

NAVAL POSTGRADUATE SCHOOL

Monterey, California



THESIS

58642

THERMODYNAMIC IMPROVEMENTS FOR THE
SPACE THERMOACOUSTIC REFRIGERATOR (STAR)

by

Michael Paul Susalla

• • •

June 1988

Thesis Co-advisor:	T. Hofler
Thesis Co-advisor:	S. L. Garrett

Approved for public release; distribution is unlimited.

T239281

REPORT DOCUMENTATION PAGE

a. REPORT SECURITY CLASSIFICATION UNCLASSIFIED		1b. RESTRICTIVE MARKINGS	
a. SECURITY CLASSIFICATION AUTHORITY		3. DISTRIBUTION/AVAILABILITY OF REPORT Approved for public release; distribution is unlimited	
b. DECLASSIFICATION/DOWNGRADING SCHEDULE			
4. PERFORMING ORGANIZATION REPORT NUMBER(S)		5. MONITORING ORGANIZATION REPORT NUMBER(S)	
5a. NAME OF PERFORMING ORGANIZATION Naval Postgraduate School	6b. OFFICE SYMBOL (If applicable) 61 Gx	7a. NAME OF MONITORING ORGANIZATION Naval Postgraduate School	
5c. ADDRESS (City, State, and ZIP Code) Monterey, CA 93943-5000		7b. ADDRESS (City, State, and ZIP Code) Monterey, CA 93943-5000	
8a. NAME OF FUNDING/SPONSORING ORGANIZATION Office of Naval Research	8b. OFFICE SYMBOL (If applicable) code 1112	9. PROCUREMENT INSTRUMENT IDENTIFICATION NUMBER	
8c. ADDRESS (City, State, and ZIP Code) 800 N. Quincy Street Arlington, VA 22217		10. SOURCE OF FUNDING NUMBERS	
		PROGRAM ELEMENT NO	PROJECT NO
		TASK NO	WORK UNIT ACCESSION NO
11. TITLE (Include Security Classification) THERMODYNAMIC IMPROVEMENTS FOR THE SPACE THERMOACOUSTIC REFRIGERATOR (STAR)			
12. PERSONAL AUTHOR(S) Susalla, Michael, Paul			
13a. TYPE OF REPORT Master's Thesis	13b. TIME COVERED FROM _____ TO _____	14. DATE OF REPORT (Year, Month, Day) 1988 JUNE	15. PAGE COUNT 172
16. SUPPLEMENTARY NOTATION "The views expressed in this thesis are those of the author and do not reflect the official policy or position of the Department of Defense or the U.S. Government."			
17. COSATI CODES		18. SUBJECT TERMS (Continue on reverse if necessary and identify by block number)	
FIELD	GROUP	SUB-GROUP	
		Thermoacoustic Refrigerator	
19. ABSTRACT (Continue on reverse if necessary and identify by block number) The objective of the STAR project is to test and space qualify a new continuous cycle cryogenic refrigeration system for cooling of sensors and electronics which is based upon the newly discovered thermoacoustic heat pumping effect. The new refrigerator has no sliding seals, a cycle frequency of about 300 Hz, and uses acoustic resonance to enhance the overall power density and efficiency. This thesis is concerned specifically with the design and testing of the thermodynamic element (or stack), which is responsible for the thermo-acoustic power conversion, and the testing of binary inert gas mixtures as working fluids. Using the refrigerator's coefficient of performance relative to the ideal Carnot coefficient of performance as a measure of efficiency, we have achieved a 93% improvement over previous designs.			
20. DISTRIBUTION/AVAILABILITY OF ABSTRACT <input checked="" type="checkbox"/> UNCLASSIFIED/UNLIMITED <input type="checkbox"/> SAME AS RPT <input type="checkbox"/> DTIC USERS		21. ABSTRACT SECURITY CLASSIFICATION UNCLASSIFIED	
22a. NAME OF RESPONSIBLE INDIVIDUAL S. L. GARRETT		22b. TELEPHONE (Include Area Code) (408)-646-2540	22c. OFFICE SYMBOL 61 Gx

Approved for public release; distribution is unlimited.

Thermodynamic Improvements for the
Space Thermoacoustic Refrigerator (STAR)

by

Michael Paul Susalla
Lieutenant, United States Navy
B.S., United States Naval Academy, 1979

Submitted in partial fulfillment of the
requirements for the degree of

MASTER OF SCIENCE IN PHYSICS

from the

NAVAL POSTGRADUATE SCHOOL
June 1988

ABSTRACT

The objective of the STAR project is to test and space qualify a new continuous cycle cryogenic refrigeration system for cooling of sensors and electronics which is based upon the newly discovered thermoacoustic heat pumping effect. The new refrigerator has no sliding seals, a cycle frequency of about 300 Hz, and uses acoustic resonance to enhance the overall power density and efficiency. This thesis is concerned specifically with the design and testing of the thermodynamic element (or stack), which is responsible for the thermo-acoustic power conversion, and the testing of binary inert gas mixtures as working fluids. Using the refrigerator's coefficient of performance relative to the ideal Carnot coefficient of performance as a measure of efficiency, we have achieved a 93% improvement over previous designs.

51672
c-1

TABLE OF CONTENTS

I.	INTRODUCTION -----	1
A.	BACKGROUND -----	1
1.	History -----	1
2.	Thermodynamics -----	4
3.	Overall Efficiency -----	7
B.	SPACE THERMOACOUSTIC REFRIGERATOR (STAR) -----	11
1.	Motivation -----	11
2.	Get Away Special (GAS) Program -----	13
3.	Shared Subsystems from NASA G-313 -----	13
C.	SCOPE -----	17
II.	THEORY -----	20
A.	THERMOACOUSTIC THEORY -----	20
1.	Qualitative Picture -----	21
2.	Single Plate -----	24
a.	Heat Flow -----	28
b.	Work Flow -----	30
c.	Efficiency -----	32
3.	Short Engine -----	32
4.	Design Considerations -----	40
B.	BINARY GAS MIXTURE THEORY -----	44
1.	Sound Speed Theory -----	44
2.	Prandtl Number Theory -----	45
a.	General Discussion -----	45

b. Kinetic Theory and Quantitative	
Analysis -----	48
3. Selection of a Gas Mixture -----	57
C. STACK DESIGN THEORY -----	59
III. STACK CONSTRUCTION -----	69
IV. EXPERIMENTAL APPARATUS AND PROCEDURE -----	80
A. DESCRIPTION OF APPARATUS -----	80
1. The Driver and its Instrumentation -----	80
2. Refrigeration Components -----	84
B. DESCRIPTION OF ELECTRONICS -----	88
C. EXPERIMENTAL PROCEDURE -----	91
1. Setup of Apparatus -----	92
2. System Startup and Operation -----	93
3. Data Recording -----	96
V. DATA ANALYSIS AND RESULTS -----	99
A. DATA ANALYSIS -----	99
B. RESULTS OF EXPERIMENT -----	105
1. Stack Modification Results -----	106
2. Results for Gas Mixtures -----	111
3. Overall Improvement -----	117
4. Other Effects of Interest -----	118
VI. CONCLUSIONS AND RECOMMENDATIONS -----	125
APPENDIX A - PRANDTL NUMBER PROGRAM -----	127
APPENDIX B - PLOTTING PROGRAM -----	141
APPENDIX C - RAW DATA -----	145
REFERENCES -----	157
INITIAL DISTRIBUTION LIST -----	160

LIST OF FIGURES

I-1	The Thermodynamics of (a) Prime Movers and (b) Refrigerators -----	5
I-2	Basic Thermoacoustic Refrigerator -----	8
I-3	Chain of Energy Transformations in a Thermoacoustic Refrigerator -----	10
I-4	Schematic of the Space Thermoacoustic Refrigerator in its Get Away Special Cannister -----	15
I-5	Block Diagram of the Electronics for the Space Thermoacoustic Refrigerator -----	16
I-6	Photograph of Hofler's (1986) Prototype Refrigerator -----	18
II-1	Gas Parcel Diagram -----	22
II-2	Theoretical Prandtl Number Dependence of Refrigerator Performance with Short Stack and Boundary Layer Approximations -----	43
II-3	Prandtl Number vs. Helium Fraction -----	58
II-4	New Stack String Arrangement -----	61
II-5	Dual Stack String Arrangement -----	62
III-1	Stack Construction Illustration -----	73
III-2	Dual Stack Construction Arrangement -----	74
III-3	Looking Down on to the Hot End of the Dual Stack -----	77
III-4	Looking Down on to the Cold End of the Dual Stack -----	77
III-5	Photograph of Dual Stack, Cold End, at 6.4x Magnification -----	78
III-6	Photograph of Dual Stack, Hot End, at 6.4x Magnification -----	79

IV-1	Schematic of Driver Apparatus Showing Acoustic Motor, Transducers, and a Portion of a Resonator. Numbered Parts are Identified in the Text.-----	81
IV-2	The Primary Refrigerator Components, Shown Attached to the Driver Assembly. The Numbered Components are Discussed in the Text.-----	85
IV-3	A Composite Copper and Aluminum Heat Exchanger Part, Prior to the Chemical Removal of Aluminum -----	87
IV-4	Block Diagram of the Electronics Used to Feedback Control the Frequency and Pressure Amplitude to Predetermined Values During Driver Operation -----	89
V-1	Temperature vs. Resistance -----	102
V-2	Temperature Ratio vs. Q_{total} for Helium, Short Resonator -----	107
V-3	COPR vs. Q_{total} for Helium, Short Resonator ---	109
V-4	Temperature Ratio vs. Q_{total} , New Stack, Short Resonator, All Gases -----	112
V-5	Temperature Ratio vs. Q_{total} , New Stack, Long Resonator, All Gases -----	113
V-6	COPR vs. Q_{total} , New Stack, Short Resonator, All Gases -----	115
V-7	COPR vs. Q_{total} , New Stack, Long Resonator, All Gases -----	116
V-8	COPR vs. Q_{total} , Showing Overall Performance Improvement -----	119
V-9	COPR vs. Q_{total} , Showing Resonator Effects ----	120
V-10	COPR vs. Q_{total} for HeXe, Short Resonator, All Stacks and Amplitudes -----	122
V-11	COPR vs. Q_{total} for He, Short Resonator, All Stacks and Amplitudes -----	123

I. INTRODUCTION

A. BACKGROUND

This being the second in a series of theses, covering different aspects of the Space Thermoacoustic Refrigerator (STAR) project, a great deal of the introductory material has already been written. In order for this thesis to be complete, the introductory material that is felt to be necessary will be repeated here. With the exception of minor corrections, Chapter I and sections A.1 and A.2 of Chapter II have been reproduced from the work of Fitzpatrick (1988).

1. History

Thermoacoustics can generally be described as the study of the interaction between heat and sound. Scientific interest in this interaction is not new. Lord Rayleigh (1878 and 1945) discussed various qualitative examples of the production of sound by heat. In one of these examples he describes investigations by Sondhauss (1850) of an effect observed by glassblowers: heating a bulb of glass at the end of a hollow rod occasionally led to the generation of sound. Faraday (1818) demonstrated that this effect occurred with gases other than air. Sondhauss proved that the vibration of the glass itself did not generate the sound, but he offered no explanation as to what did. In his

description of Sondhauss' work, Rayleigh stressed the importance of the phase difference between temperature and particle motion. Rijke (1859) built an open tube with a wire mesh inside. When the mesh was heated, the tube produced a sound of impressive intensity. The functioning of this oscillator is slightly different since it requires steady gas flow for its operation. A similar sound production effect was observed by Taconis, et al. (1949) in hollow tubes immersed in liquid helium (4.2°K). The Taconis oscillations were addressed quantitatively by Yazaki, et al. (1980). The work described above deals primarily with prime movers. These are devices that convert a temperature gradient into sound energy. We call this the classical era of thermoacoustics.

Interest in thermoacoustics was renewed when the idea of the use of acoustical devices as refrigerators appeared. Gifford and Longworth (1966) described the pumping of heat along a surface caused by a periodic change in the pressure of the adjoining gas. Such a change can be produced by the oscillations of a sound wave. In their experiments Merkli and Thomann (1974) explored the heating and cooling effects on the wall of a gas-filled resonant tube. They found that heat was transported from a region near the velocity antinode (or maximum value) of the sound's standing wave to regions near the adjacent pressure antinodes. Thermoacoustic prime movers have also received

recent attention. Kempton (1976) investigated the excess noise of aeroengines above that predicted by theory. He determined that the sound was produced by unsteady heat transfer. Each of these latter three groups of experimenters used some theory for comparison, but it was mostly qualitative. None provided the complete quantitative theory that would explain their experimental observations.

The theoretical breakthrough in the thermoacoustics field was made by Nicklaus Rott (1969, 1974, 1975 and 1980). His theory combined the basic principles from physics, thermodynamics and acoustics to quantitatively describe the effects found in both types of thermoacoustic devices: prime movers and heat pumps. Prime movers use a temperature gradient to create sound, as in the effects discussed by Sondhauss, Rayleigh, Taconis and Kempton. Heat pumps, or refrigerators, use the oscillating pressure of a sound wave to produce a temperature difference, as described by Gifford and Longworth and Merkli and Thomann. Rott described the effect found by Merkli and Thomann as thermoacoustic streaming. It is this effect that makes thermoacoustic refrigeration possible.

Inspired by Ceperley's (1979) traveling wave Sterling Cycle heat engine and Rott's quantitative theory, the team of Wheatley, Hofler, Swift, Migliori and Garrett (1982, 1983a, 1983b, 1985 and 1986) developed a series of thermoacoustic experiments at Los Alamos National

Laboratory in New Mexico. They investigated the basic thermoacoustic effects in both prime movers and refrigerators and compared their experimental results to Rott's theory.

2. Thermodynamics

We'll digress from history here to explain the thermodynamic distinction between prime movers and refrigerators. This discussion follows Sears and Salinger (1975). A prime mover receives heat at a high temperature, T_H (the hot reservoir), does work on its surroundings, and rejects heat at a lower temperature, T_C (the cold reservoir), as shown in Figure I-1.a. The first law of thermodynamics tells us that the heat flow (Q_H) from the hot reservoir must equal the work done on the surroundings (W) plus the heat flow (Q_C) to the cold reservoir:

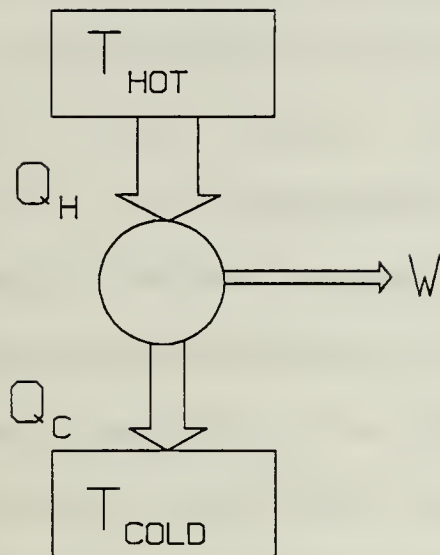
$$Q_H = W + Q_C. \quad (I-1)$$

The second law of thermodynamics states that in every process the entropy of the universe must either remain constant or increase. The entropy change for the isothermal heat transport to/from the reservoirs is defined as the heat flow divided by the reservoir temperature. For a prime mover the second law can be written:

$$\Delta S_H \leq \Delta S_C \quad \text{or} \quad Q_H/T_H \leq Q_C/T_C. \quad (I-2)$$

The thermal efficiency of the prime mover is defined as the ratio of the work output to the heat input:

$$\eta = W/Q_H = (Q_H - Q_C)/Q_H = 1 - (Q_C/Q_H). \quad (I-3)$$



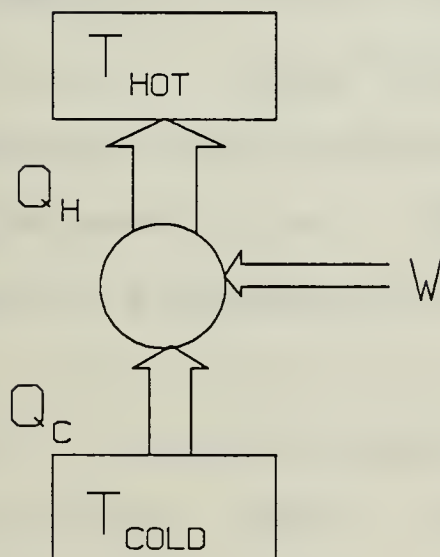
(a)

FIRST LAW: $Q_H = W + Q_C$

SECOND LAW: $\frac{Q_H}{T_H} \leq \frac{Q_C}{T_C}$

EFFICIENCY:

$$\eta = \frac{W}{Q_H} \leq 1 - \frac{T_C}{T_H}$$



(b)

FIRST LAW: $Q_H = W + Q_C$

SECOND LAW: $\frac{Q_H}{T_H} \geq \frac{Q_C}{T_C}$

COEFFICIENT OF PERFORMANCE:

$$\text{COP} = \frac{Q_C}{W} \leq \frac{T_C}{T_H - T_C}$$

Figure I-1. The Thermodynamics of (a) Prime Movers and (b) Refrigerators

Comparing equations I-2 and I-3 gives us a limit on the efficiency based on the temperatures of the reservoirs:

$$\eta \leq 1 - (T_C/T_H). \quad (I-4)$$

This limit is known as the Carnot efficiency.

In a refrigerator the process is basically reversed (see figure I-1.b.). Heat (Q_C) is removed from the low temperature reservoir, work (W) is received from the surroundings, and heat (Q_H) is delivered to the higher temperature reservoir. The expression for the first law is the same as for the prime mover, Equation I-1. For the refrigerator it means the heat flow into the hot reservoir must equal the heat flow from the cold reservoir plus the work done on the system. The second law for this case is:

$$\Delta S_H \geq \Delta S_C \quad \text{or} \quad Q_H/T_H \geq Q_C/T_C. \quad (I-5)$$

The efficiency parameter for the refrigerator is called the coefficient of performance (COP). It is defined as the ratio of the heat flow from the cold reservoir to the work input to the refrigerator, or:

$$COP = Q_C/W = Q_C/(Q_H - Q_C) \leq T_C/(T_H - T_C). \quad (I-6)$$

The limit is known as the Carnot coefficient of performance.

The work in this thesis deals solely with refrigerators. Even though prime movers are mentioned from time to time, the primary focus of the rest of our discussion will be refrigerators.

3. Overall Efficiency

According to Hofler (1986), the early thermoacoustic work at Los Alamos focused on experimental refrigerating engines. The performance of these engines fell short of expectations, leading to simple experiments on basic thermoacoustic effects and a proof-of-principle experiment on thermoacoustic refrigeration. Hofler then applied the Rott theory to the experimental systems and solved the resulting equations numerically. For his doctoral dissertation from the University of California, San Diego, Hofler designed and constructed a completely functional thermoacoustic refrigerator. He also made accurate measurements of its thermodynamic efficiency, and used this efficiency to make comparisons to the Rott theory. After receiving his doctorate, Hofler came to the Naval Postgraduate School (NPS) as a post-doctoral fellow, and brought his prototype refrigerator with him.

The purpose of this thesis, in conjunction with the work of several other students, is to modify Hofler's refrigerator design in order to improve its overall efficiency and make it suitable for space cryocooler applications. The basic design of the thermoacoustic refrigerator is shown schematically in Figure I-2. The driver (A), which produces the sound waves, is coupled to the resonator (D) using bolts, via a reducer cone (B) and bellows (C). Inside the resonator is a stack of plastic

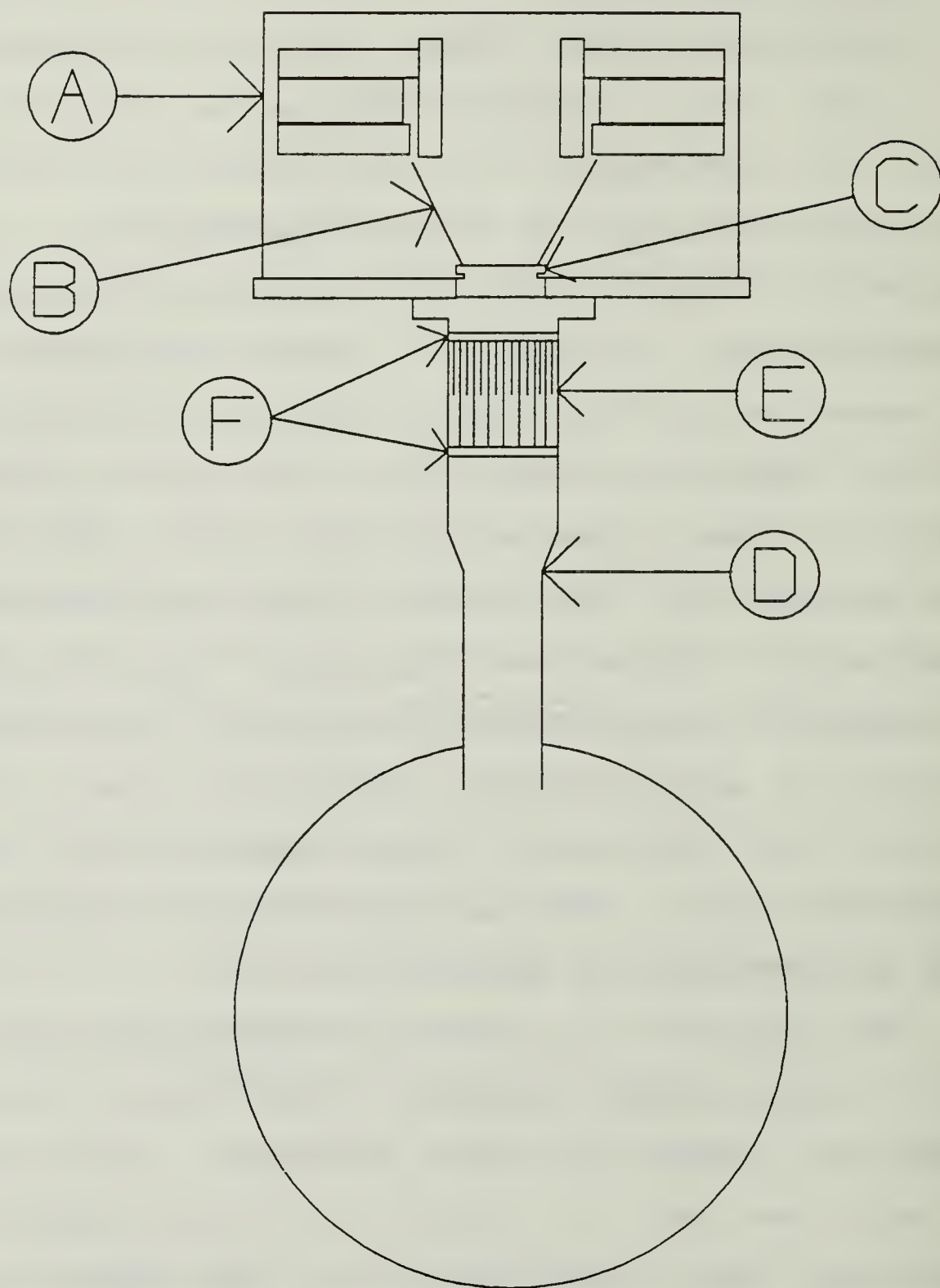


Figure I-2. Basic Thermoacoustic Refrigerator

plates (E) and their heat exchangers (F). The heat exchangers allow heat to be removed from the hot end of the stack and applied to the cold end. It is the interaction between the sound waves and the plastic plates that produces a temperature difference across the plates and allows heat to be pumped from the cold heat exchanger to the hot heat exchanger. A brief description of efficiency would be useful here. Figure I-3 shows a diagram of the chain of energy transformations which occur in a thermoacoustic refrigerator. There are three conjugate variable pairs (V and I , P and U , and ΔT and Q_C), and two transformations (electrical-to-acoustical and acoustical-to-thermal).

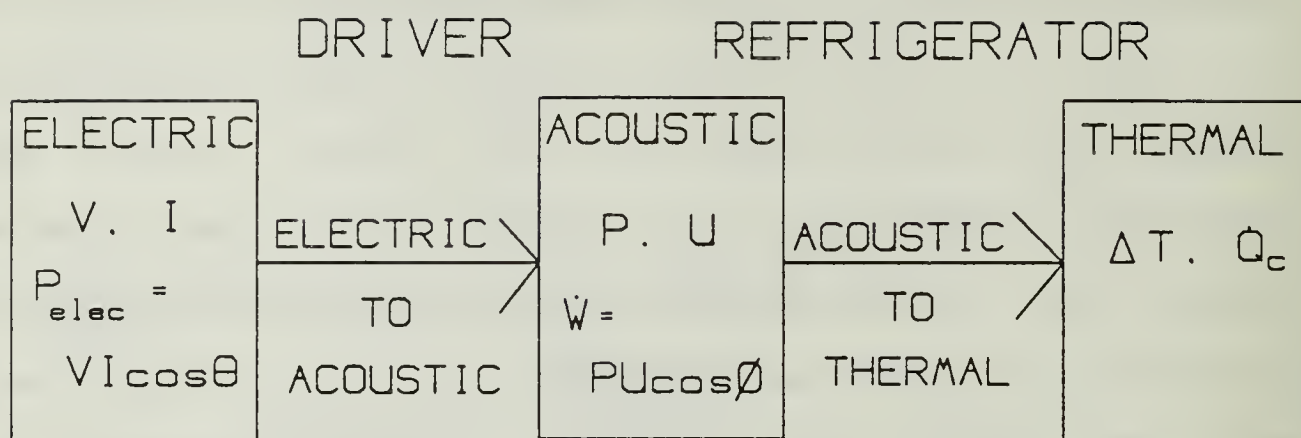
We start with electrical input power to the driver, which can be calculated (using r.m.s. values) with:

$$P_{\text{elec}} = IV \cos \theta, \quad (\text{I-7})$$

where I is the current into the electroacoustic driver, V is the voltage across the driver terminals, θ is the phase angle between I and V , and $\cos \theta$ is known as the "power factor." An electrodynamic driver converts the electrical power to acoustic power (the first transformation). Analogous to the previous definition of the electrical input power, the acoustic power is given by:

$$\dot{W} = PU \cos \phi, \quad (\text{I-8})$$

where P is the acoustic pressure, U is the volumetric velocity, which equals the product of particle velocity and



ELECTROACOUSTIC
EFFICIENCY

$$n_{EA} = \frac{\dot{W}}{P_{elec}}$$

REFRIGERATOR
COEFFICIENT OF
PERFORMANCE

$$COP = \frac{\dot{Q}_c}{\dot{W}}$$

OVERALL THERMOACOUSTIC EFFICIENCY

$$n_{TA} = \frac{\dot{Q}_c}{P_{elec}} = n_{EA} \cdot COP$$

Figure I-3. Chain of Energy Transformations
in a Thermoacoustic Refrigerator

resonator cross-sectional area, and ϕ is the phase angle between them. The efficiency of this electroacoustic transformation is given by:

$$\eta_{EA} = \dot{W} / P_{elec} \quad (I-9)$$

In the second transformation, the refrigerator converts the acoustic power to a temperature gradient (T) and heat flow (Q). As discussed previously, the efficiency for this transition is given by the coefficient of performance:

$$COP = \dot{Q}_C / \dot{W} \quad (I-10)$$

The overall thermoacoustic efficiency is therefore the product of the efficiencies for the two transformations:

$$\eta_{TA} = (\eta_{EA})(COP) = \dot{Q}_C / P_{elec} \quad (I-11)$$

Improvements in the overall refrigerator efficiency can thus be divided into two distinct, though interrelated, efforts. The first is the subject of this thesis: modifications to improve the coefficient of performance. The second effort involves modifications to the driver to optimize the electroacoustic efficiency and is addressed by LT Michele Fitzpatrick, U.S. Coast Guard, in her master's thesis.

B. SPACE THERMOACOUSTIC REFRIGERATOR (STAR)

1. Motivation

In addition to improving overall efficiency, our experimental refrigerator will be designed and built with the intention of flying it on the space shuttle as part of

the National Aeronautics and Space Administration's (NASA) Get Away Special (GAS) program. As of 3 February 1988, there is a Memorandum of Agreement between the Naval Postgraduate School (NPS) and the Air Force which provides funding for the space flight and which assigns the NASA payload number G-337 to this project. The reason for testing the thermoacoustic refrigerator in space is that the immediate applications of the STAR are expected to be the cooling of electronics, high T_C superconductors and infrared detectors in space.

There are currently two primary methods for cooling satellite systems in space: (1) evaporation of expendable cryogens (liquid helium, nitrogen, ammonia-methane and solid hydrogen, etc.), and (2) closed cycle refrigerators (Stirling cycle, Vuilleumier cycle, etc.), which involve large reciprocating piston masses operating at low frequency. [Walker (1983) and Smith, et al. (1984)] The disadvantages of these current cooling methods are their short lifetimes (expendable cryogens) and high vibration levels and low reliability (closed cycle refrigerators). The advantages of the thermoacoustic refrigerator over these and other systems lie in its simplicity and reliability. The STAR has no sliding seals, relatively efficient performance, low vibration levels and (hopefully) a longer life span.

The thermoacoustic refrigerator needs to be surrounded by a vacuum and insulating material to minimize heat loss due to thermal conduction and radiation. The vacuum of space will provide the best insulation to determine the refrigerator's ultimate efficiency. The absence of gravity removes the possibility of thermal convection as an additional nuisance heat transport effect.

2. Get Away Special (GAS) Program

NASA's GAS program allows small, self-contained payloads to fly on the Space Shuttle in GAS canisters for relatively low cost (\$10,000) (Get Away Special Team, 1984). The GAS can is five cubic feet in volume and can house a payload of up to 200 pounds. Each payload must contain its own electrical power, control, data acquisition and storage facilities, etc. The Shuttle's astronauts will turn a switch on or off at designated times during the flight, but are otherwise not involved with the experiment.

3. Shared Subsystems from NASA G-313

Another group of NPS students and faculty (Boyd, et al., 1987) have taken advantage of the GAS program to measure the resonant acoustic modes of the shuttle payload bay and the ambient acoustic environment produced as a result of main engine and booster operation during launch. Their experiment is titled "The Space Shuttle Cargo Bay Vibroacoustics Experiment" and is designated by NASA as payload G-313. Several subsystems that were developed for

NASA G-313 will be used by NASA G-337 (STAR). A schematic of the STAR in its GAS can is shown in Figure I-4. One of the systems borrowed from NASA G-313 is the controller system used to run the experiment and record the data. The recorder system consists of the INTEL model BPK 5V75 magnetic bubble memory module and an NSC 800 micro-processor-based controller. Two other NPS students, LT Charles B. Cameron, USN and CPT Ronald Byrnes, USA, will be designing the analog electronics and software to integrate these systems into the STAR experiment for their master's theses. A block diagram of the electronics is shown in Figure I-5.

Another borrowed system is the power supply, which consists of Gates brand lead acid battery cells (five ampere-hour, two volts each). These gelled electrolyte batteries are ideal for the STAR due to their high power density, low cost and the low level of outgassing during discharge cycles. NASA G-313 used a one layer battery of 68 cells providing 680 watt-hours of energy and weighing about 80 pounds (including the cells' support structure). We will be using two battery layers with as many cells as we can, up to 136. This will give us a minimum of 680 watt-hours and a maximum of 1,360 watt-hours of available electrical energy, and a total battery weight between 80 and 160 pounds. The number of cells we can use will depend on the total weight of the driver-resonator assembly and

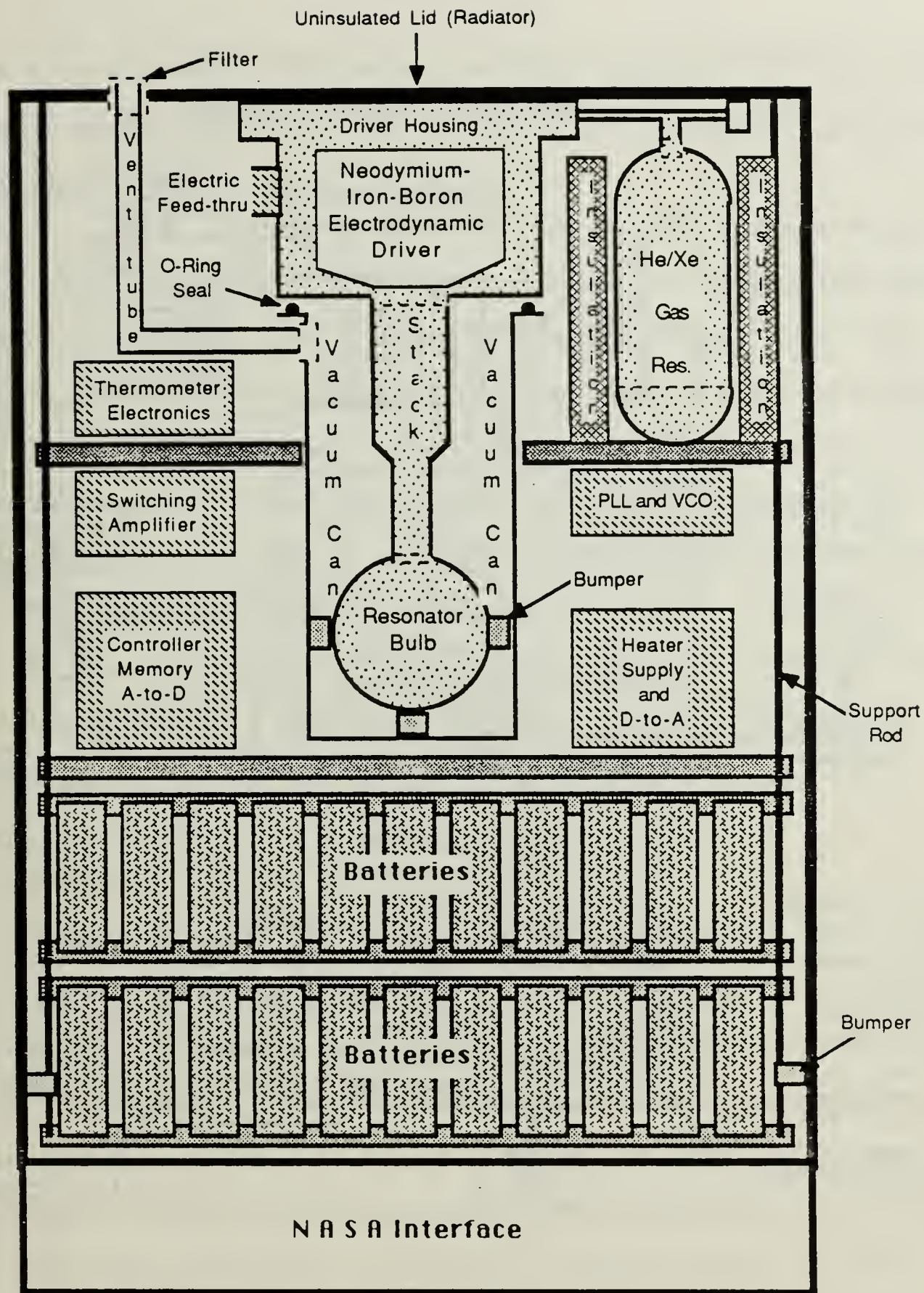
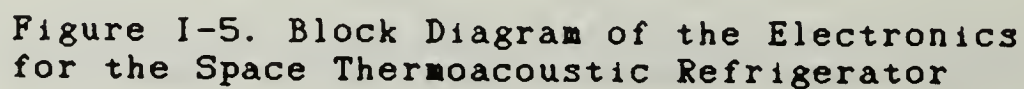


Figure I-4. Schematic of the Space Thermoacoustic Refrigerator in its Get Away Special Cannister

The diagram illustrates the control system for a high-power ultrasonic transducer. The system is enclosed in a dashed rectangular boundary. At the top, a 'Radiator Plate' is connected to a 'Driver' block, which contains a transformer with primary terminals 'Pg' and 'Pm' and a secondary terminal 'A'. The 'Driver' is connected to a 'Hot Ex' (External) block, which is part of a 'Stack' of transducer elements. The 'Stack' is also connected to a 'Cold Ex' (External) block, which is connected to a 'Heater'. The 'Heater' is powered by a 'Heater Power Supply' connected to 'From Control'. The 'Stack' is monitored by three thermocouples: 'TC1' (connected to the 'Radiator Plate'), 'TC2' (connected to the 'Hot Ex'), and 'TC3' (connected to the 'Cold Ex'). 'TC1' and 'TC2' are connected to 'Thermocouple Electronics', which outputs to 'To Control'. 'TC3' is connected to the 'Heater Power Supply'. The control system includes an 'Automatic Gain Control' (AGC) block, which receives 'DC' from 'From Control' and 'AC' from a 'VCO' (Variable Frequency Oscillator). The AGC outputs 'AC' to a 'Switching Power Amp', which drives the 'Driver'. The 'Driver' outputs 'AC' to a 'Pressure Gage' and 'AC' to a 'Mike Amp' (Microphone Amplifier). The 'Pressure Gage' outputs 'DC' to 'To Control'. The 'Mike Amp' outputs 'AC' to an 'Accel. Amp' (Accelerometer Amplifier). The 'Accel. Amp' outputs 'AC' to a 'Phase Detector'. The 'Phase Detector' outputs 'DC' to an 'Integrator (Feedback Control)' block. The 'Integrator' outputs 'DC' to the 'VCO' and 'To Control'. The 'VCO' outputs 'AC' to the 'Automatic Gain Control' and 'To Control'. The 'Automatic Gain Control' also outputs 'DC' to 'To Control'. The 'Heater Power Supply' outputs 'DC' to the 'Heater'. The 'Heater' is connected to the 'Cold Ex' block. The 'Stack' is connected to the 'Hot Ex' block. The 'Radiator Plate' is connected to the 'Driver'.



its auxilliary equipment (vacuum can, gas reservoir, etc.) and electronics, as we have to stay within the 200 pound limit.

The use of the GAS can imposes certain restrictions. Since we are using batteries to supply the power, the refrigerator has to be energy efficient. Also, the GAS can setup requires the STAR to be compact and lightweight. Figure 1-6 shows a photograph of Hofler's prototype refrigerator. This setup, which includes parts that will be unnecessary in space, is approximately six feet in height. In comparison, the maximum payload height for the GAS can is 28.25 inches, or less than 2.5 feet. These considerations played a major role on the choice of equipment for and the design of the STAR.

C. SCOPE

This thesis is primarily experimental in nature. The purpose being to improve the thermodynamic efficiency of Hofler's prototype refrigerator. Theory is presented only as necessary to provide the reader with an understanding of the thermoacoustic refrigeration process and to explain why certain modifications were made. For this reason, no direct comparison of overall refrigerator performance to theory is presented. Hofler (1986) presents a quantitative comparison of the refrigerator's performance to the detailed Rott theory.

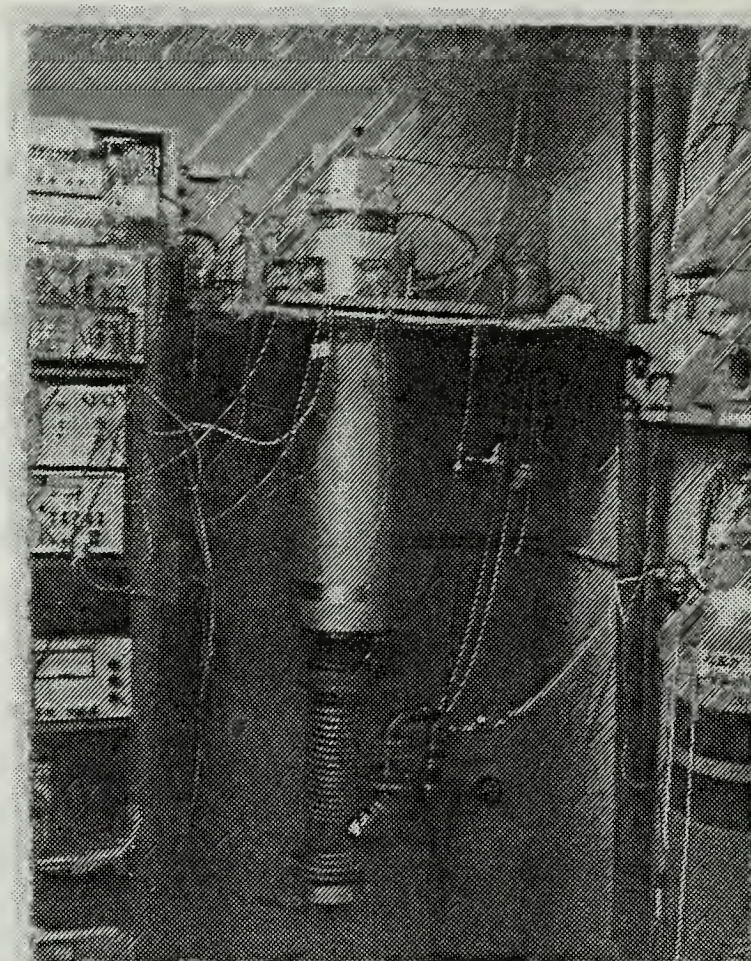


Figure I-6. Photograph of Hofler's (1986)
Prototype Refrigerator

Chapter II. begins with a fairly in depth discussion of thermoacoustic theory, to provide the above mentioned understanding and to illustrate possible areas for the improvement of efficiency. This is followed by the details of how and why specific modifications, such as gas mixtures and stack designs, were made.

Chapter III. provides all of the information necessary for the construction of a thermoacoustic stack.

Chapter IV. provides a discussion of the overall experimental apparatus and procedures. We have basically used the prototype system of Hofler (1986) for our experiments. The material in sections A and B of this chapter are derived primarily from Hofler's doctoral dissertation (1986), with emphasis on the few areas that we have changed.

Chapter V. presents the methods used for analysis of our data and the overall results of our experiments.

Chapter VI. provides conclusions and recommendations for further development.

II. THEORY

A. THERMOACOUSTIC THEORY

As stated in Chapter I., the first two sections (A.1. and A.2) of this Chapter are essentially reproduced from the master's thesis of LT Michele Fitzpatrick (1988).

Thermoacoustic theory has been developed in detail by Rott (1969, 1974, 1975 and 1980) and adapted to the thermoacoustic refrigerator by Wheatley et al. (1982, 1983a, 1983b, 1985 and 1986), Wheatley and Cox (1985), Hofler (1986) and Swift (1989).

The space thermoacoustic refrigerator (STAR) basically consists of an acoustic driver producing sound waves in a resonant tube (see Figure I-2). This resonator is filled with a mixture of helium-xenon gas (≈ 12.5 atomic % xenon) pressurized to ten atmospheres, and contains a stack of plastic plates. This section of the Chapter will present a qualitative model for the thermoacoustic heat pumping process followed by a quantitative development for heat and work flow at a single plate. This is followed by a more rigorous development for the heat flow, work flow and coefficient of performance for a stack of plates that are much shorter than one quarter wavelength. Section A. concludes with a discussion of some of the changes that

could improve the coefficient of performance of the refrigerator.

1. Qualitative Picture

Consider a parcel of gas that moves back and forth along one of the plates at the acoustic frequency (see Figure II-1). As it moves, the gas parcel will experience changes in temperature and volume. Part of the temperature changes come from the adiabatic compression and expansion of the gas by the sound pressure, and part as a consequence of the local temperature of the plate itself. A temperature gradient may develop along the plate as a result of the operation of the refrigerator. The temperature and volume changes can be described by six separate steps (the changes in volume are indicated by changes in the size of the square parcel in the figure).

Assume the plate is at a uniform temperature, T . The parcel starts at position 1 ($X=0$) with a temperature of T . The sound wave moves the parcel to the right to position 2. The parcel has undergone adiabatic compression and its temperature is now T^{++} . Since the temperature of the gas is higher than that of the plate, heat (Q) will flow from the gas parcel to the plate. The parcel's volume is decreased and its temperature lowered to T^+ . This heat flow also causes the plate's temperature to increase at the position X^+ . Parcel position 3 is actually in the same location as position 2, but is displaced vertically in the figure for

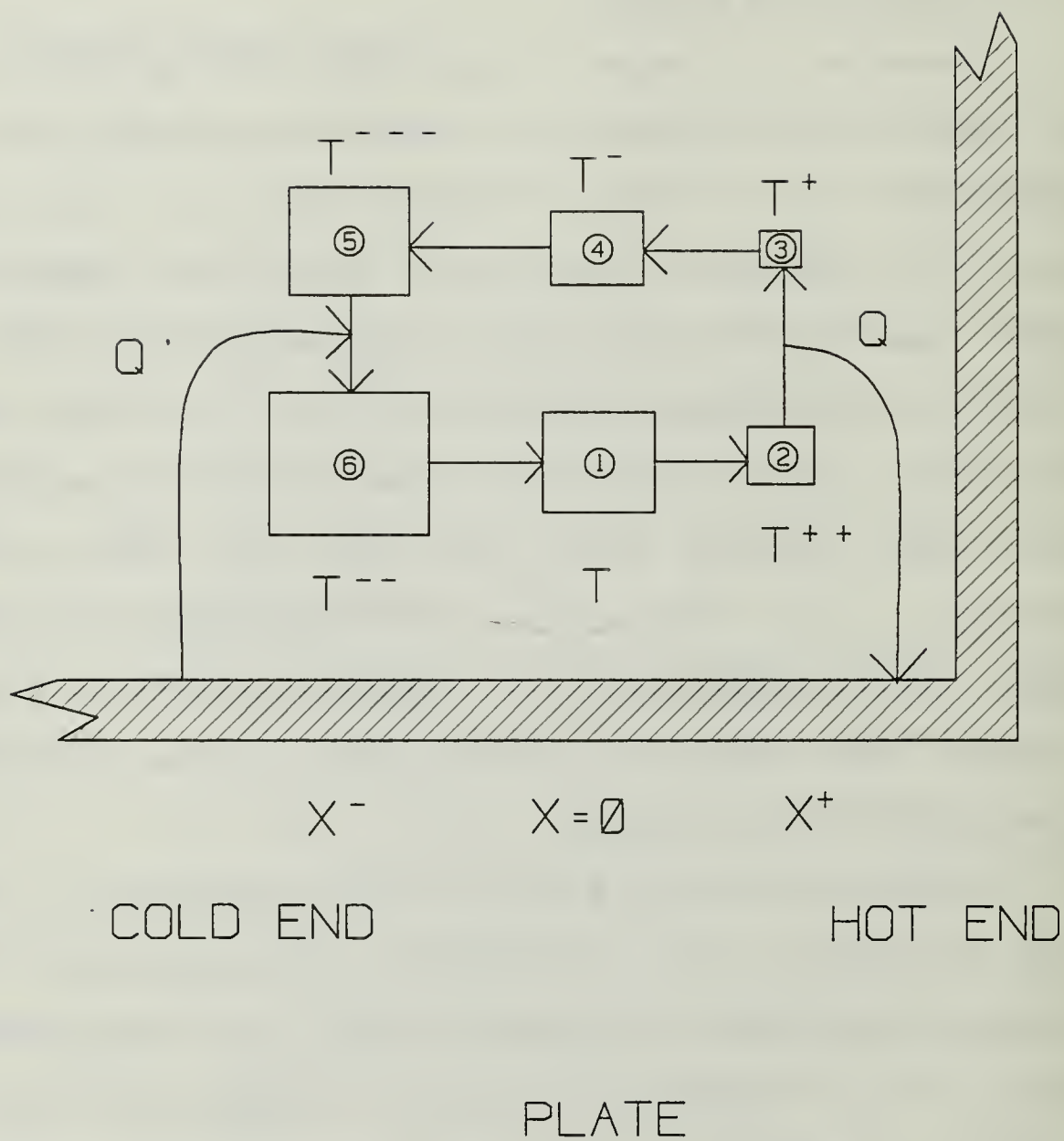


Figure II-1. Gas Parcel Diagram (Note: Displacement in the Vertical Direction is Shown for Clarity--Parcel Moves in Horizontal Direction Only.)

clarity. The parcel now moves to position 4 and expands adiabatically to a new temperature of T^- . A repeat of this process puts the parcel in position 5 with a temperature of T^{--} . Now the temperature of the gas is lower than that of the plate and heat (Q') flows from the plate to the gas parcel, expanding the parcel and raising its temperature to T^{--} . This heat flow causes the plate's temperature to decrease at position X^- . The parcel moves to the right, again under adiabatic compression, and we are back where we started, in position 1 with temperature T (adapted from Wheatley, et al., 1985).

This gas parcel cycle is repeated at the resonator's operating frequency. For the STAR this frequency is between approximately 250 and 600 cycles per second, depending on the gas types and mixture (specifically the speed of sound in the gas) and the length of the resonator.

Notice that the temperature of the gas parcel at position $X=0$ is different depending on which direction the gas parcel is moving. It is this phase shift in temperature relative to motion that produces the thermoacoustic effect, as we will show in the calculations that follow.

It is also important to note that in order for heat to flow between the gas parcel and the plate, the parcel must be vertically located within about one thermal penetration depth of the plate. The thermal penetration depth (δ_K) is the distance that heat can diffuse through

the fluid during a time $1/\omega$, where ω is the acoustic angular frequency.

Wheatley, et al. (1986) describe thermoacoustic engines as consisting of long trains of these gas parcels, all about a thermal penetration depth from the plate. The parcels draw heat from the plate at one extreme of their oscillatory motion and deposit heat at the other extreme. Adjacent heat flows cancel, except at the ends of the plate. The net result is that an amount of heat, Q , is passed from one end of the plate to the other. It should be noted that the above discussion assumes zero viscosity.

2. Single Plate

Swift (1989) illustrated the basic principles of the thermoacoustic engine by examining a simple example of a single plate in a gas-filled tube such as we described above. In this example the acoustic and thermodynamic effects are nearly distinct. In the absence of the plastic plate, the plane standing wave sustained in the tube has well known acoustic properties. Its pressure and x-direction velocity (along the length of the tube) are given as (using peak values):

$$p_1 = P_A \sin(x/\lambda) \quad (\text{II-1})$$

$$\text{and } u_1 = i(P_A/\rho_m a) \cos(x/\lambda) \quad (\text{II-2})$$

where P_A is the pressure amplitude at the pressure antinode, $\lambda = \lambda/2\pi = a/\omega$ is the reduced wavelength, λ is the wavelength, a is the speed of sound in the gas, ω is the

angular frequency and ρ_m is the mean density of the gas. The subscript 1 indicates the first order time oscillation, and the subscript m indicates the mean value. The total pressure can be given as:

$$p = p_m + p_1 e^{i\omega t}. \quad (\text{II-3})$$

A similar expression may be used to represent the total velocity. Following Swift, we will assume that the first order in the acoustic amplitude is sufficient for all acoustic and thermodynamic variables (pressure, velocity, temperature, density and entropy).

The sound wave is adiabatic and has an oscillatory temperature given by:

$$T_1 = (T_m \beta / \rho_m c_p) p_1, \quad (\text{II-4})$$

where $\beta = -(d\rho/dT)_p / \rho_m$ is the isobaric thermal expansion coefficient and c_p is the isobaric (constant pressure) heat capacity per unit mass. Note that T_1 and p_1 are in phase. For ideal gases, thermodynamics tells us that:

$$T_m \beta / \rho_m c_p = (\gamma - 1) T_m / \gamma p_m, \quad (\text{II-5})$$

where $\gamma = c_p / c_v$ is the ratio of isobaric to isochoric specific heats. γ equals 5/3 for monatomic gases and is smaller but still greater than one for other gases. Combining Equations II-4 and II-5 gives us:

$$T_1 / T_m = [(\gamma - 1) / \gamma] p_1 / p_m. \quad (\text{II-6})$$

The introduction of the plastic plate into the standing wave modifies the original, unperturbed temperature oscillations. This modification is due to the heat

flow between the gas and the plate, as described previously. The temperature is modified in both magnitude and phase for gas about a thermal penetration depth away from the plate. According to Swift, this results in two important effects: 1) a time averaged heat flow near the surface of the plate, along the direction of acoustic vibration, and 2) the generation or absorption of real acoustic power near the surface of the plate. In refrigerators the effect is an absorption of acoustic power. In prime movers the acoustic power is generated by the temperature gradient present in the plate.

There are several assumptions we will make to simplify calculations, again following Swift. We assume that the plate is short enough compared to a reduced wavelength ($\Delta x \ll \lambda$) and far enough from both velocity and pressure nodes that p_1 and u_1 can be considered uniform over the entire plate. We assume the gas has zero viscosity, so that u_1 does not depend on y (we had already made this assumption by looking at u_1 in the x -direction only). We assume that the plate has a large enough heat capacity per unit area that its temperature does not change appreciably at the acoustic frequency. We assume that the plate has a mean temperature gradient in the x -direction ∇T_m . Finally we neglect the plate's and gas' thermal conductivity in the x -direction.

Applying these assumptions, we see that the mean fluid temperature ($T_m(x)$) is the same as that of the plate. Swift calculated the oscillating fluid temperature using the general equation of heat transfer. He kept only first-order terms, neglected thermal conduction along x and applied the boundary condition, $T_1(0)=0$, imposed by the plate. The resulting equation is:

$$T_1(y)=[(T_m \beta / \rho_m c_p) p_1 - (\nabla T_m / \omega) u_1][1 - \exp[-(1+i)y/\delta_K]]. \quad (II-7)$$

To interpret this equation, we look at it in the limit that the gas is far enough from the plate ($y \gg \delta_K$) to make negligible thermal contact with the plate. This gives:

$$T_1(y) \approx [(T_m \beta / \rho_m c_p) p_1 - (\nabla T_m / \omega) u_1]. \quad (II-8)$$

The first term in Equation II-8 is the temperature oscillation due to the adiabatic expansions and compressions of the gas (see Equation II-4). The second term comes from the mean temperature gradient in the gas. As the gas oscillates along x with displacement amplitude u_1/ω , the temperature at a given point in space oscillates by an amount $\nabla T_m u_1/\omega$ even if the temperature of a given piece of fluid remains constant. The actual temperature oscillations are a linear superposition of these two effects.

The y dependent part of Equation II-7 is complex. It approaches 1 for $y \gg \delta_K$, as given previously. It approaches zero for $y \ll \delta_K$, where the plate imposes the condition $T_1=0$. Most importantly, for $y \approx \delta_K$, its magnitude is still on the

order of 1, but it has a substantial imaginary part. This phase shift in the oscillating temperature of the standing wave at $y \approx \delta_k$, due to the thermal presence of the plate, is an important result because it leads directly to the time averaged heat flow in the x-direction. This is the same phase shift that was emphasized in the description of the gas parcel motion.

a. Heat Flow

Swift argues that since we are neglecting ordinary thermal conductivity in the x direction, the only way heat can be transported along x is by the hydrodynamic transport of entropy, carried by the oscillatory velocity u_1 :

$$\dot{q}_2 = T_m \rho_m \overline{s_1 u_1} = (1/2) \rho_m c_p \text{Im}[T_1] u_1. \quad (\text{II-9})$$

The line above the quantity $s_1 u_1$ indicates the time-average of the first order entropy and velocity product. The heat flow is a second order quantity, signified by the subscript 2.

The total heat flow \dot{Q}_2 along the plate, in the x direction, is found by integrating \dot{q}_2 over the y-z plane:

$$\dot{Q}_2 = \pi \int_0^\infty \dot{q}_2 dy \quad (\text{II-10})$$

where π is the perimeter of the plate in the y-z plane.

Substituting for T_1 and performing the integration gives:

$$\dot{Q}_2 = -(1/4) \pi \delta_k (T_m \beta) p_1 u_1 (\Gamma - 1) \quad (\text{II-11})$$

where $\pi \delta_k$ is the thermodynamically active area in a plane perpendicular to the longitudinal acoustic motion, $T_m \beta$ is

the heat parameter of the gas, and r is defined as the ratio of actual temperature gradient to the critical temperature gradient ($\nabla T / \nabla T_{\text{crit}}$). The critical temperature gradient occurs when the temperature change along the plate just matches the temperature change due to the adiabatic compression of the gas, and no heat flows between the gas and the plate. This is the boundary between the refrigerator and prime mover functions of thermoacoustic engines.

Equation II-11 shows that when $r < 1$, heat flows up the temperature gradient from cold to hot and work (acoustic power) is absorbed, as for a refrigerator. When $r = 1$ there is no heat flow. When $r > 1$, heat flows down the temperature gradient from hot to cold and acoustic power is produced, as for a prime mover.

Note that the total heat flow is proportional to the area $\pi \delta_x$, and to $T_m \beta$ (which equals 1 for ideal gases). It is also proportional to the product $p_1 u_1$, and so equals zero if the plate is at either a pressure or velocity node of the standing wave. The maximum value of the product occurs halfway between the nodes. Finally, the heat flow is proportional to the temperature gradient factor $r - 1$. For $\nabla T_m > \nabla T_{\text{crit}}$, $r - 1$ is greater than zero and the heat flow is toward the pressure node, while for $\nabla T_m < \nabla T_{\text{crit}}$, $r - 1$ is less than zero and the heat flow is away from the pressure node. If suitable heat exchangers, at T_H and T_C , are installed at

the ends of the plate (with $T_H - T_C = T_m \Delta x$), this heat flow carries heat from one exchanger to the other.

The heat flow is small under ordinary circumstances. However, in closed resonators it is possible to achieve sound amplitudes many orders of magnitude higher than those of ordinary conversation. Since \dot{Q}_2 is proportional to P_A^2 , and since in practical acoustic engines the entire cross section of the standing wave is filled with plates (spaced roughly $4\delta_K$ apart), very high heat flows and/or a large $T_H - T_C$ may be achieved.

b. Work Flow

The work flow (i.e. acoustic power) is given by the work per cycle times the rate at which that work occurs (the acoustic frequency f). From thermodynamics, the average acoustic power produced per unit volume is:

$$\dot{w}_2 = -(\omega / \rho_m) \overline{i p_1 \dot{\rho}_1} = -(1/2) \omega \rho p_1 \text{Im}[T_1]. \quad (\text{II-12})$$

The gas about a thermal penetration depth away from the plate "breathes", because of thermal expansion and contraction, with the right time phase with respect to oscillating pressure to do (or absorb) net work. This is exactly the same gas that we have seen is responsible for the heat flow. Gas elsewhere is ineffective in doing (or absorbing) work. The density oscillations for $y \ll \delta_K$ and for $y \gg \delta_K$ are in phase with the pressure oscillations, and hence do (or absorb) no net work.

The total acoustic power produced, \dot{W}_2 , is found by integrating \dot{w}_2 over all space, as with the heat flow:

$$\dot{W}_2 = (1/4) \pi \delta_x (\gamma - 1) (p_1^2 / \rho_m a) (r - 1) \Delta x / \lambda, \quad (\text{II-13})$$

where all the terms have been defined previously.

The acoustic power is proportional to the volume $\pi \delta_x \Delta x$ of a fluid that is about a thermal penetration depth from the plate. It is proportional to p_1^2 , and so is quadratic in the acoustic amplitude (as was the heat flow) and vanishes at pressure nodes. Finally \dot{W}_2 is proportional to $r - 1$, the same temperature gradient factor as appeared in \dot{Q}_2 (Equation II-11). When $\nabla T_m = \nabla T_{\text{crit}}$, $r - 1 = 0$, and there are no temperature oscillations in the fluid, other than those due to adiabatic processes, and no acoustic power is absorbed or generated. For $\nabla T_m > \nabla T_{\text{crit}}$, $r - 1 > 0$ and acoustic power is produced near the plate. Whether this power increases the amplitude of the standing wave, is radiated away to infinity, is simply absorbed, or flows through an acoustic-to-electric transducer to generate electric power depends on details of the resonator, not on the plate itself or the standing wave near the plate. For $\nabla T_m < \nabla T_{\text{crit}}$, $r - 1 < 0$ and acoustic power is absorbed near the plate. For a tube without plates, which has a diameter less than the wavelength, at constant temperature ($\nabla T = 0$), this work flow is responsible for the ordinary thermal attenuation of a sound wave (Kinsler, et al., 1982).

c. Efficiency

We combine Equations II-11 and II-13 to get the efficiency of the plate with no viscous losses or longitudinal conduction losses:

$$\eta = \dot{W}_2 / \dot{Q}_2 = [(\gamma - 1) / (T_m \beta)] (\omega \Delta x p_1) / (\rho_m a^2 u_1). \quad (\text{II-14})$$

Since $u_1 = u_0 \sin(x/\lambda)$, and $p_1 = \rho_m a u_0 \cos(x/\lambda)$, we get:

$$\eta = [(\gamma - 1) / (T_m \beta)] (\Delta x / (\lambda \tan(x/\lambda))). \quad (\text{II-15})$$

For $x \ll \lambda$, this reduces to:

$$\eta = [(\gamma - 1) / (T_m \beta)] (\Delta x / x), \quad (\text{II-16})$$

$$\text{and} \quad \eta = \eta_{\text{carnot}}^{\gamma}. \quad (\text{II-17})$$

This efficiency approaches the Carnot efficiency as the power output and heat transfer rates approach zero.

We can make a similar calculation for the refrigerator mode of operation, where the relevant efficiency is the coefficient of performance (COP). Given that $\text{COP} = \dot{Q}_2 / \dot{W}_2$, we find that:

$$\text{COP} = \gamma (\text{COP}_{\text{carnot}}). \quad (\text{II-18})$$

3. Short Engine

Having developed the simplified case of a single plate we now turn our attention to a more realistic model, with an entire stack of plates. Since Swift (1989) has incorporated the thermoacoustic theory of Rott (1969, 1973, 1974, 1975 and 1980), we will once again follow his development closely. The assumptions that the length of the stack is much shorter than a wavelength and that the temperature spanned is much less than the absolute

temperature will be retained. However, this more realistic model includes viscosity, longitudinal thermal conduction, finite (instead of infinite) plate heat capacity and a stack of plates (instead of just one). The goal in our development is to include these effects, which produce many complications, in such a manner as to maintain a connection to the more simplified, but more easily understood, development of the previous section.

Swift defines a co-ordinate system where the x-axis is along the direction of acoustic vibration (longitudinal in the stack) and the y-axis is perpendicular to the planes of the plates (using a parallel plate geometry) with the y-origin centered between two plates. This gives a plate spacing of $2y_0$ and a plate thickness of $2l$. He begins with an equation of motion and a continuity equation for the fluid:

$$\rho[(\partial \vec{v}/\partial t) + (\vec{v} \cdot \nabla) \vec{v}] = -\nabla p + \nu \nabla^2 \vec{v} + (\xi + \nu/3) \nabla(\nabla \cdot \vec{v}), \quad (\text{II-19})$$

$$\text{and} \quad (\partial \rho/\partial t) + \nabla \cdot (\rho \vec{v}) = 0, \quad (\text{II-20})$$

where ρ is density, \vec{v} is velocity, p is pressure, ν is kinematic viscosity (Swift uses μ for this parameter) and ξ is second viscosity. He imposes the boundary condition that $\vec{v}=0$ at the fluid-plate interface. He then uses the equation for heat flow in a fluid and solid:

$$\rho T[\partial s/\partial t + \vec{v} \cdot \nabla s] = \nabla \cdot (\lambda \nabla T) + (\text{quadratic velocity terms}), \quad (\text{II-21})$$

$$\text{and} \quad \rho_s c_s (\partial T_s/\partial t) = \lambda_s \nabla^2 T_s, \quad (\text{II-22})$$

where λ is thermal conductivity, s is entropy per unit

mass, T is absolute temperature and the subscript s refers to the solid. The applicable boundary conditions are that $T=T_s$ and $\lambda \partial T / \partial y = \lambda_s \partial T_s / \partial y$ at the fluid-plate interface. Equations for each of the needed parameters are then linearized, assuming that they all oscillate at the angular frequency ω :

$$p = P_m + p_1(x) e^{i\omega t}, \quad (\text{II-23})$$

$$\rho = \rho_m + \rho_1(x, y) e^{i\omega t}, \quad (\text{II-24})$$

$$\vec{v} = \hat{x} u_1(x, y) e^{i\omega t} + \hat{y} v_1(x, y) e^{i\omega t}, \quad (\text{II-25})$$

$$T = T_m(x) + T_1(x, y) e^{i\omega t}, \quad (\text{II-26})$$

$$T_s = T_m(x) + T_{1,s}(x, y) e^{i\omega t}, \quad (\text{II-27})$$

$$\text{and } s = s_m(x) + s_1(x, y) e^{i\omega t}, \quad (\text{II-28})$$

where the subscript m denotes a mean value and the subscript 1 refers to a first-order quantity. Swift then manipulates these equations, by integrating with respect to y , into the form of a wave equation for $p_1(x)$ and an equation for energy flux \dot{H}_2 (which includes both heat and work since $\dot{H} = \dot{Q} + \dot{W}$) along x . The wave equation is: (II-29)

$$\left[1 + \frac{(\sigma - 1)f_k}{1 + \epsilon_s} \right] p_1 + \frac{\rho_m a^2}{\omega^2} \frac{d}{dx} \left[\frac{1 - f_v}{\rho_m} \frac{dp_1}{dx} \right] - \frac{a^2}{\omega^2} \frac{f_k - f_v}{(1 - \sigma)(1 + \epsilon_s)} \frac{dT_m}{dx} \frac{dp_1}{dx} = 0$$

and the equation for energy flux is:

$$\begin{aligned} \dot{H}_2 = & \frac{\pi y_0}{2\omega \rho_m} \text{Im} \left[\frac{d\tilde{p}_1}{dx} p_1 \left[1 - \tilde{f}_v - \frac{T_m \beta (f_k - \tilde{f}_v)}{(1 + \epsilon_s)(1 + \sigma)} \right] \right] \\ & + \frac{\pi y_0 c_p}{2\omega^3 \rho_m (1 - \sigma)} \frac{dT_m}{dx} \frac{dp_1}{dx} \frac{dp_1}{dx} \text{Im} \left[\tilde{f}_v + \frac{(f_k - \tilde{f}_v)(1 + \epsilon_s)(f_v / f_k)}{(1 + \epsilon_s)(1 + \sigma)} \right] \end{aligned}$$

$$-\pi(y_0\lambda + l\lambda_s) \frac{dT_m}{dx} \quad (II-30)$$

We have used $\sigma = \eta c_p / \lambda$ as Prandtl number,

$$f_k = \tanh[(1+i)y_0/\delta_k] / [(1+i)y_0/\delta_k], \quad (II-31)$$

$$f_v = \tanh[(1+i)y_0/\delta_v] / [(1+i)y_0/\delta_v], \quad (II-32)$$

$$\text{and } \delta_s = \frac{\eta c_p}{\rho_s c_s} \tanh[(1+i)y_0/\delta_k] / \rho_s c_s \delta_s \tanh[(1+i)l/\delta_s], \quad (II-33)$$

where δ is a specific penetration depth denoted by the appropriate subscript, k for thermal penetration depth in the fluid, s for thermal penetration depth in the solid and v for viscous penetration depth in the fluid (which is roughly the distance that shear momentum diffuses in time $1/\omega$). Swift then applies some simplifying assumptions to produce equations that can be related to the results of section 2. A "boundary layer" approximation (i.e., $y_0 \gg \delta_k$ and $l \gg \delta_s$) sets the hyperbolic tangents to unity. Since in practical engines the plate spacing is 2 to 4 thermal penetration depths (or greater) and the hyperbolic tangent function is within a few percent of unity at $y_0 = 2\delta_k$, this is a reasonable approximation. A "short stack" approximation (i.e., $\Delta x \ll \lambda$) yields relations for p_1 and u_1 that are identical to those of section 2, with the exception of a $(1+l/y_0)$ term in u_1 that accounts for the velocity being higher inside the stack. This approximation also gives us the fact that p_1 , u_1 and all thermophysical properties are independent of x within the stack. Finally, the zero viscosity assumption is made (although viscosity

will be added back in later) thereby setting v and f_v equal to zero. Using these approximations Equations II-29, II-30 and II-33 can be reduced to:

$$p_1 + \frac{\rho_m a^2}{\omega^2} \frac{d}{dx} \left[\frac{1}{\rho_m} \frac{dp_1}{dx} \right] = \frac{(\gamma-1) \delta_K}{(1+i)(1+\epsilon_s) y_0} (\gamma-1) p_1, \quad (\text{II-34})$$

$$\dot{H}_2 = -\frac{1}{4} \pi \delta_K \frac{T_m}{1+\epsilon_s} p_1^s u_1^s (\gamma-1) - \pi (y_0 \lambda + l \lambda_s) \frac{dT_m}{dx}, \quad (\text{II-35})$$

$$\text{and} \quad \epsilon_s = \frac{\rho_m C_p \delta}{\rho_s C_s \delta_s}, \quad (\text{II-36})$$

where all terms have previously been defined. It can be seen that the first term in Equation II-35 is identical to the hydrodynamic heat flux \dot{Q}_2 derived for the single plate, except for the $1/(1+\epsilon_s)$ term. This term accounts for the finite heat capacity of the plate and modifies the boundary condition for T_1 at the fluid-plate interface to a non-zero value, thereby reducing the heat flux. For the short stack \dot{W}_2 is small ($\dot{W}_2/\dot{Q}_2 = \text{carnot}/\gamma = \Delta T/T_m \ll 1$) so heat flux and energy flux are approximately equal. The second term in Equation II-35 accounts for ordinary conduction of heat down the temperature gradient by the fluid and solid.

The next step is to derive an equation for the acoustic power. Since net acoustic power cannot enter or leave the engine in the y -direction the acoustic power generated or absorbed must involve the difference in average acoustic intensity $\overline{p_1 u_1}$ between the two ends of the stack. Using this and the fact that $dp_1/dx = -i\omega \rho_m u_1$, Swift

manipulates Equation II-34 to arrive at a relation for acoustic power:

$$\dot{W}_2 = -\frac{1}{4} \pi \delta_K \Delta x \frac{(\gamma-1)\omega}{\rho_m a^2 (1+\epsilon_s)} |p_1|^2 (\gamma-1), \quad (\text{II-37})$$

which is the same as Equation II-13, with the exception of the $1/(1+\epsilon_s)$ term which was discussed above. From these results it is clear that, under these simplifying assumptions, the short engine performs in a manner similar to that predicted by the single plate results.

We now follow Swift in repeating this derivation, but include non-zero viscosity. The inclusion of viscosity adds some complexity to the situation. Under these circumstances u_1 becomes a function of y and the concept of critical temperature gradient becomes less well defined. Since T_1 now depends on y , in an irregular fashion, there is no natural definition of ∇T_{crit} . However, we will use (as did Swift) $r = \nabla T_m / \nabla T_{\text{crit}}$ and $\nabla T_{\text{crit}} = T_m \rho_1^s / \rho_m c_p \langle u_1^s \rangle$, where the superscript s defines the value for the standing wave. The addition of viscosity modifies the relation for dp_1/dx to:

$$\frac{dp_1}{dx} = - \frac{i\omega \rho_m \langle u_1 \rangle}{1-f_v} = - \frac{\omega \rho_m \langle u_1^s \rangle}{1-f_v}, \quad (\text{II-38})$$

which is complex even though $\langle u_1^s \rangle$ is real.

Substituting into Equations II-29 and II-30 and applying the boundary layer approximation yields the following relations:

$$\dot{H}_2 = -\frac{1}{4} \pi \delta_K \frac{T_m \bar{p}_1^S \langle u_1^S \rangle}{(1+\epsilon_S)(1+\sigma)(1-\delta_v/y_0 + \frac{1}{2}(\delta_v/y_0)^2)} \left[\frac{\Gamma}{1+\sigma^{\frac{1}{2}}} - \left[1+\sigma^{\frac{1}{2}} - \frac{\delta_v}{y_0} \right] \right],$$

$$- (y_0^{\lambda+1} \lambda_S) \frac{dT_m}{dx} \quad (II-39)$$

and

$$p_1 + \frac{\rho_m a^2}{\omega^2} \frac{d}{dx} \left[\frac{1-f_v}{\rho_m} \frac{dp_1}{dx} \right] = \frac{(\gamma-1) \delta_K p_1}{(1+i)(1+\epsilon_S) y_0} \left[\frac{\Gamma}{(1+\sigma^{\frac{1}{2}})(1-f_v)} - 1 \right]. \quad (II-40)$$

For the zero viscosity case, $\sigma=0$, these relations reduce to Equations II-34 and II-35.

Work flow is calculated, using the short stack approximation, from the wave equation. This gives:

$$\dot{W}_2 = -\frac{1}{4} \pi \delta_K \Delta x \frac{(\gamma-1) \omega (p_1^S)^2}{\rho_m a^2 (1+\epsilon_S)} \left[\frac{\Gamma}{(1+\sigma^{\frac{1}{2}})(1-\delta_v/y_0 + \delta_v^2/2y_0^2)} - 1 \right]$$

$$- \frac{1}{4} \pi \delta_v \Delta x \frac{\omega \rho_m \langle u_1^S \rangle^2}{1-\delta_v/y_0 + \delta_v^2/2y_0^2}, \quad (II-41)$$

which reduces to Equation II-37 when $\sigma=0$.

From these relations it is clear that viscosity makes the situation much more complex. Since the goal is an expression for the coefficient of performance, it is necessary to determine \dot{Q}_2/\dot{W}_2 . We know that $\dot{H}_2 = \dot{Q}_2 + \dot{W}_2$, such that $COP = \dot{Q}_2/\dot{W}_2 = (\dot{H}_2 - \dot{W}_2)/\dot{W}_2 = (\dot{H}_2/\dot{W}_2) - 1$. In order to maintain the essential effects of viscosity, while reducing the complexity of the resulting equations, we will include viscosity only to the lowest order present, that is $\sigma^{\frac{1}{2}}$. Additionally we will assume that $y_0 \approx \delta_K$, which is the case for most practical engines as previously discussed. This

gives us that $\delta_v/y_0 \approx \delta_v/\delta_k = \sigma^{1/2}$. Applying these approximations to Equations II-40 and II-41 yields:

$$\dot{H}_2 = -\frac{1}{4}\pi\delta_k \frac{T_m p_1^S \langle u_1^S \rangle}{(1+\epsilon_s)(1-\sigma^{1/2})} (r-1) - \pi(y_0^{\lambda+1} \lambda_s) \frac{dT_m}{dx}, \quad (\text{II-42})$$

and

$$\dot{W}_2 = \frac{1}{4}\pi\delta_k \Delta x \frac{(\gamma-1)\omega(p_1^S)^2}{\rho_m a^2 (1+\epsilon_s)} (r-1) - \frac{1}{4}\pi\delta_v \Delta x \omega \rho_m \langle u_1^S \rangle^2, \quad (\text{II-43})$$

Now we can take the ratio of these two relations and get a useable, understandable relation for the coefficient of performance, which is what we are trying to improve experimentally. The result is:

$$\text{COP} = \frac{\left[\frac{-(1/4)\pi\delta_k T_m p_1^S \langle u_1^S \rangle (r-1)}{(1+\epsilon_s)(1-\sigma^{1/2})} - \pi(y_0^{\lambda+1} \lambda_s) \frac{dT_m}{dx} \right]}{\left[\frac{(1/4)\pi\delta_k \Delta x (\gamma-1)\omega(p_1^S)^2 (r-1)}{\rho_m a^2 (1+\epsilon_s)} - \frac{1}{4}\pi\delta_v \Delta x \omega \rho_m \langle u_1^S \rangle^2 \right]} - 1 \quad (\text{II-44})$$

The above relations are approximate expressions, which should apply to realistic situations, with the only remaining assumptions being 1) the short stack approximation, 2) the boundary layer approximation, and 3) a small Prandtl number approximation. We have previously explained that the boundary layer approximation is reasonable for the plate separations of our stacks. The short stack approximation is also not particularly restrictive for realistic engines. With a Prandtl number of approximately 0.027 for helium-xenon we have a relatively small Prandtl number, so this approximation is also very

reasonable. In his comparison to theory, Hofler (1986) shows that in relatively "long" acoustic engines Equations II-29 and II-30 predict the performance within 20 to 30 percent.

4. Design Considerations

The purpose of this section is to discuss the primary modification that we have made based on theory, that is, the reduction of the Prandtl number of the system. To evaluate how this affects performance we will first look at Equation II-44. We know, from experience, that the second term in the numerator is small compared to the first term. We also know that ϵ_s is, in general, small compared to unity, so we will set $\epsilon_s = 0$ for evaluation purposes. The product $T_m \beta$ is known to equal unity for ideal gases. Applying these conditions, with Swift's $\delta_v = \delta_k \sigma^{1/2}$ and $y_0 = \delta_k$ we can reduce Equation II-44 to:

$$COP = \left[\frac{\{[-4\pi y_0 p_1^S \langle u_1^S \rangle (r-1)] / (1-\sigma^{1/2})\} - [\pi(y_0 \lambda + 1 \lambda_s) dT_m / dx]}{\{[4\pi y_0 \Delta x (\gamma-1) p_1^{S^2} (r-1)] / (\rho_m a^2)\} - [4\pi y_0 \sigma^{1/2} \Delta x \omega \rho_m \langle u_1^S \rangle^2]} \right]^{-1} \quad (II-45)$$

It is clear from this that as σ is reduced, $1-\sigma^{1/2}$ is increased resulting in an overall decrease in the numerator of our relation, and $\sigma^{1/2}$ is reduced resulting in a decrease in the denominator of our relation. These two effects, when evaluated fully, show that COP will decrease with reduced Prandtl number. However, we know based on our experiments that this cannot be true for our system. This effect that is apparently the opposite of what we expect, and know to

be true, is therefore due to some (or one) of the approximations that we have made being invalid for our system. As we are about to show, the relations given in Equations II-39 and II-41 yield the proper result, indicating that the inclusion of viscosity only to the lowest order does not provide adequately for the effects of viscosity in our system.

Looking at Equations II-39 and II-41 we see that they are fairly complex. We will use the simplifications that $\epsilon_s = 0$, $T_m \beta = 1$ and $\rho_m a^2 = \gamma p_m$; and we will consider the thermal conduction term in the heat flow to be negligible. We also know that $\delta_x = \delta_v / \sigma^{1/2}$, and we will use $p_1^s = p_0 \cos kx$ and $\langle u_1^s \rangle = a(1/\gamma)(p_0/p_m) \sin kx$ to further simplify our relations. This allows us to re-write Equations II-39 and II-41 as:

$$\frac{4\dot{H}_2 \gamma p_m}{\pi \delta_k p_0^2} = \frac{a \cos kx \sin kx}{(1+\sigma)[1-\delta_v/y_0 + \frac{1}{2}(\delta_v/y_0)^2]} \left[\gamma \frac{1+\sigma^{1/2}+\sigma}{1+\sigma^{1/2}} - (1+\sigma^{1/2}-\delta_v/y_0) \right],$$

(II-46) and

$$\frac{4\dot{W}_2 \gamma p_m}{p_0^2 \pi \delta_k} = (\gamma-1) \omega \Delta x \cos^2 kx \left[\frac{\gamma}{(1+\sigma^{1/2})(1-\delta_v/y_0 + \frac{1}{2}(\delta_v/y_0)^2)} - 1 \right] - \frac{\omega \Delta x \sigma^{1/2} \sin^2 kx}{[1-\delta_v/y_0 + \frac{1}{2}(\delta_v/y_0)^2]}. \quad (II-47)$$

Now we can combine Equations II-46 and II-47 to get a relation for COP as follows:

$$COP = \frac{\cos kx \sin kx}{kx(1+\sigma)(1-\delta_v/y_0 + \frac{1}{2}(\delta_v/y_0)^2)} \left\{ - - - \right\} - 1, \quad (II-48)$$

where the brackets {---} represent the following relation:

$$\frac{r[(1+\sigma^{\frac{1}{2}}+\sigma)/(1+\sigma^{\frac{1}{2}})]-(1+\sigma^{\frac{1}{2}}-\delta_v/Y_0)}{(Y-1)\cos^2 kx \left[\frac{r}{(1+\sigma^{\frac{1}{2}})(1-\delta_v/y_0+\frac{1}{2}(\delta_v/y_0)^2)} - 1 \right] - \left[\frac{\sigma^{\frac{1}{2}}\sin^2 kx}{1-\delta_v/y_0+\frac{1}{2}(\delta_v/y_0)^2} \right]}$$

and we have used $a/\omega \Delta x \approx a/\omega x = 1/kx$. It is not clear from this relation how COP will vary with Prandtl number. However, if we define a set of variables and perform a numerical analysis we can see the desired effect. We will define a quantity, $\delta_M = (\delta_v \delta_k)^{\frac{1}{2}} = \text{constant}$, as the geometric mean of the penetration depths, such that $\delta_v = \delta_M \sigma^{\frac{1}{4}}$ and $\delta_v/y_0 = (\delta_M/y_0) \sigma^{\frac{1}{4}}$. This roughly corresponds to our experiment. Setting reasonable values for the four parameters in our relation: $kx=0.2$, $r=0.7$, $\delta_M/y_0=0.5$ and $Y=1.667$, we can see how COP varies with Prandtl number. Figure II-2 is a plot showing how heat (\dot{H}_2), work (\dot{W}_2) and COP vary with Prandtl number, using Equations II-46, II-47 and II-48. It is clear that as Prandtl number is reduced COP increases. It should be noted that as Prandtl number becomes very small we actually see COP decrease with reduced Prandtl number, as we estimated using the approximation with only the lowest order viscosity terms. Since Swift's engine (1989) with liquid sodium has a Prandtl number of approximately 0.004, his approximation is in fact valid for his system, although it is not for ours, as we discussed above.

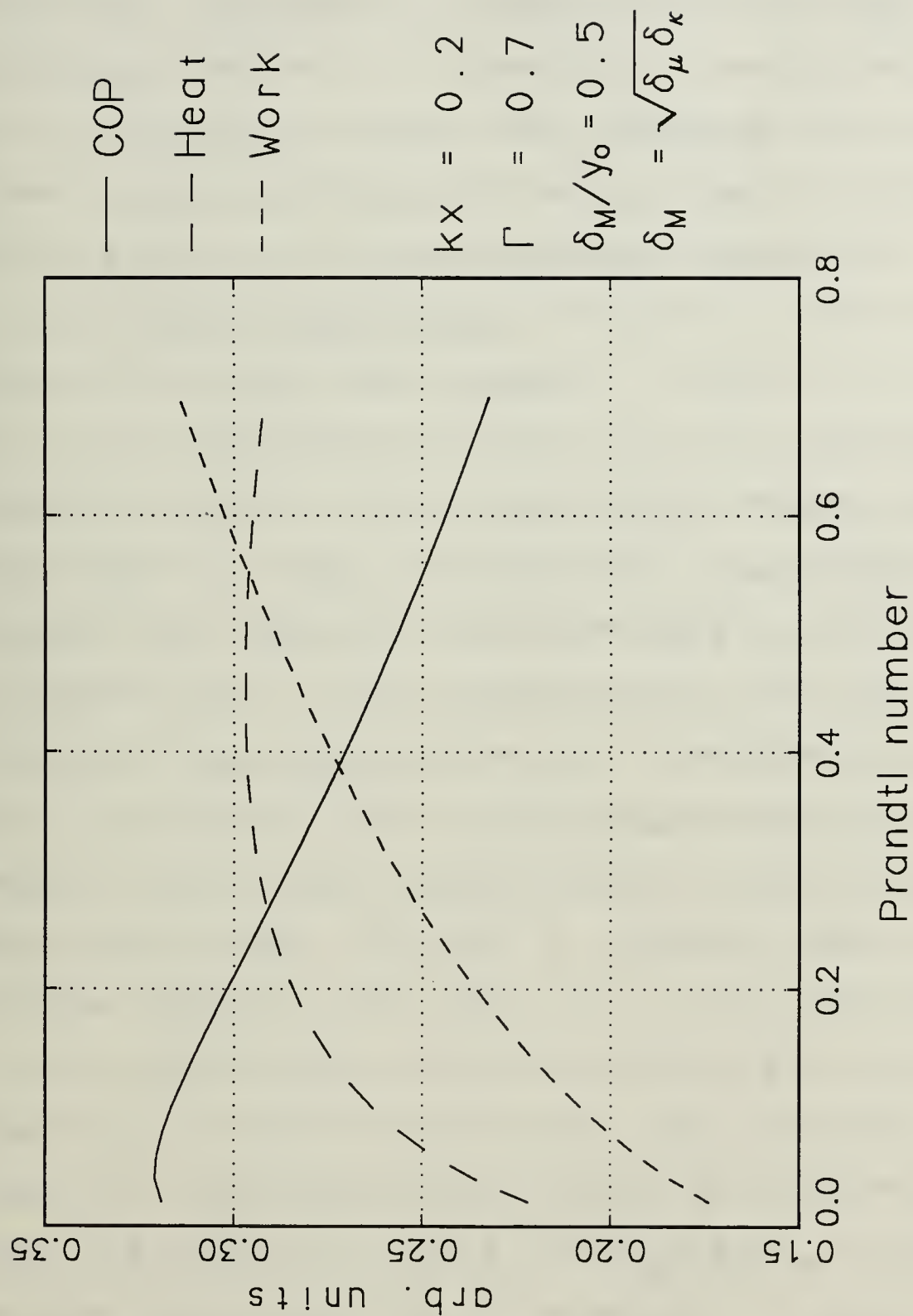


Figure 11-2. Theoretical Prandtl Number Dependence of Refrigerator Performance with Short Stack and Boundary Layer Approximations.

B. BINARY GAS MIXTURE THEORY

1. Sound Speed Theory

One of the parameters of importance, when considering refrigerator performance, is the velocity of sound in the fluid being used. The purpose of this section is to show how this value is calculated for binary gas mixtures.

In general, the sound speed "a" in a gas is given by the relation: $a = (\gamma R_0 T / m)^{1/2}$, where $\gamma = c_p / c_v$ is the ratio of isobaric to isochoric specific heats, R_0 is the universal gas constant, T is the absolute temperature and m is the molecular weight of the gas. This relation holds for a binary mixture of gases as well. However, γ and m may be different for a mixture and must be calculated. From Huang (1976) we get a relation for the specific heat capacity of a binary mixture: $(c_p)_{ij} = [x_i M_i c_{pi} + x_j M_j c_{pj}] / [x_i M_i + x_j M_j]$, where x_i is the mole fraction of the i^{th} species, M_i is the molecular weight of the i^{th} species and c_{pi} is the isobaric specific heat capacity of the i^{th} species. A similar relation holds for c_v as well. The equivalent molecular weight m , of the mixture is given by: $m = x_i M_i + x_j M_j$.

Combining the above relations we get a final equation for the speed of sound of a binary mixture, as follows:
$$a = \{ [R_0 T (x_i M_i c_{pi} + x_j M_j c_{pj})] / [(x_i M_i + x_j M_j) (x_i M_i c_{vi} + x_j M_j c_{vj})] \}^{1/2}.$$

Since γ is approximately 5/3 for any ideal monatomic gas it is clear that any variation due to c_p and c_v will be small. Therefore, the primary effect on sound speed, of

mixing two gases is that it is inversely proportional to the square root of the total mass. At 300 degrees Kelvin the sound speeds of the mixtures used in our experiment are as follows:

pure helium	$a \approx 1008$ m/s
helium-argon (19% Ar)	$a \approx 614$ m/s
helium-xenon (12% Xe)	$a \approx 460$ m/s

2. Prandtl Number Theory

a. General Discussion

Before going into the details of how Prandtl number varies for binary gas mixtures, it is important to understand the general concept of Prandtl number, and to discuss the expected variation based on this concept. Prandtl number is a dimensionless ratio that relates transport properties of fluids. In Fluid Mechanics it is given the symbol "Pr" and in Thermodynamics we use " σ ". Prandtl number can be represented in many different ways. For calculational purposes we define Prandtl number as $\sigma = \eta c_p / \lambda$, where η is dynamic viscosity, c_p is the isobaric specific heat capacity and λ is the thermal conductivity of the fluid. This relation is used because these parameters are well tabulated and more readily calculated than others that are available. For an understanding of the physics of Prandtl number and how it relates to the refrigeration process we define Prandtl number as $\sigma = \nu / \kappa$, where $\nu = \eta / \rho$ is the kinematic viscosity and $\kappa = \lambda / \rho c_p$ is the thermal

diffusivity. This definition is used because kinematic viscosity represents momentum diffusion through the fluid due to a gradient in the velocity, and thermal diffusivity represents the diffusion of thermal energy due to temperature gradients in the fluid. This says that Prandtl number is a ratio of momentum diffusion to thermal diffusion. A third way of describing Prandtl number is $\sigma = (\delta_v / \delta_k)^2$, where δ_v is the viscous penetration depth and δ_k is the thermal penetration depth. The capacity for diffusion of a given quantity is directly related to the magnitude of the associated penetration depth. Since $\delta_v = (2\nu/\omega)^{1/2}$ is a function of kinematic viscosity, and $\delta_k = (2k/\omega)^{1/2}$ is a function of thermal diffusivity, we will restrict the discussion to ν and k effects.

Hirschfelder et al., (1954, p.14) derive a relation, using simple kinetic theory, for the thermal conductivity of a monatomic gas, $\lambda = 15R_0\eta/4M$, where R_0 is the universal gas constant and M is the molecular weight of the gas. From this relation and the knowledge that $c_p - c_v = R$ and $\gamma = c_p/c_v$, where $R = R_0/M$, it is easily shown that $\sigma = \eta c_p / \lambda = 4\gamma / (15(\gamma - 1))$ for a monatomic gas. It is also known that $\gamma = 5/3$ for any monatomic gas, which results in $\sigma = 2/3$ for all monatomic gases. Calculations using rigorous kinetic theory also show that Prandtl number is approximately $2/3$ for monatomic gases. This theory will be discussed in the next section.

When two monatomic gases are combined the molecular interactions produce changes in the physical properties, resulting in Prandtl number deviating from the $2/3$ value. For a mix of a heavy gas and a light gas, as we have used, the Prandtl number drops rapidly as the percentage of heavy gas increases from zero. This is due primarily to a very rapid rise in the molecular density ($=\text{grams/mole}$) of the gas as the concentration of the heavier gas increases from zero to some small percentage. As an example, a mix of two percent xenon with 98% helium produces a .64% increase in this molecular density. Since the kinematic viscosity, $\nu = \eta/\rho$, is inversely proportional to this molecular density, while dynamic viscosity is relatively invariant, there is a rapid drop in kinematic viscosity and therefore momentum diffusion. Thus, we see that the momentum diffusion process is dominated by the presence of the heavier gas molecules. The thermal diffusivity, $K = \lambda/\rho c_p$, on the other hand is inversely proportional to the product ρc_p , which is essentially constant with changes in concentration, and directly proportional to the thermal conductivity, thereby changing strictly due to variations in thermal conductivity. Reif (1965) represents thermal conductivity by $\lambda = c(kT/m)^{3/2}$, where c is a heat capacity per molecule (which is essentially a constant), k is the Boltzmann constant, T is the absolute temperature and m is the molecular weight. It is clear from

this relation that the thermal conductivity, and therefore thermal diffusivity and thermal energy diffusion, will be much greater for a lighter gas, and their values will be dominated by the concentration of the lighter gas in the mixture. Combining these two effects it is clear that both momentum and thermal energy diffusion rates decrease with increasing concentration of the heavier gas. However, the rate of change in momentum diffusion is much more dramatic at the lower concentrations and drops off rapidly as the concentration of the heavier gas increases, while the rate of change of thermal energy diffusion is much more gradual and continuous over the concentration range. This results in the ratio of the two, which is effectively the Prandtl number, dropping rapidly from the $2/3$ value for the pure light gas as the heavier gas is initially introduced, reaching a minimum as the momentum diffusion steadies out and rising back to the $2/3$ value as energy diffusion continues to decrease while the heavier gas concentration approaches 100%.

b. Kinetic Theory and Quantitative Analysis

The purpose of this section is to discuss the theory, with its assumptions and limitations, and the equations used to calculate the Prandtl number of a binary gas mixture. Much of the information presented here is reproduced in Appendix A in order to allow the removal and use of Appendix A without reference back to the main body

of the text. Hirschfelder, et al. (1954) introduce a basic kinetic theory in Chapter one, develop a rigorous kinetic theory in Chapter seven and present equations for the calculation of thermal conductivity and dynamic viscosity for binary gas mixtures in Chapter eight of their text. Using these relations with another for the isobaric specific heat capacity of the mixture we can determine Prandtl number, $\sigma = \eta c_p / \lambda$. Rather than reproduce the work of Hirschfelder, et al. (1954) we will present a discussion of the methods they used in deriving their equations, including the assumptions and limitations that apply. Then we will present all of the equations necessary for the calculation of Prandtl number for a binary gas mixture, and a sample curve of Prandtl number as a function of concentration that was created using the output data of the program presented in Appendix A, which uses these equations.

The development of the kinetic theory of gases is based on knowledge of the distribution function that represents the number of molecules of a specific species, in a unit volume element, about a point in space, with velocities in a unit range about a specified velocity, at a given instant in time. This distribution function is represented by $f_i(r, v_i, t)$. Hirschfelder, et al. derive the Boltzmann equation, in terms of this distribution function, which is the basis for discussion of transport properties

of gases. The Boltzmann equation is given as:

$$\frac{\partial f_i}{\partial t} + \left(V_i \frac{\partial f_i}{\partial r} \right) + \frac{1}{m_i} \left(X_i \frac{\partial f_i}{\partial V_i} \right) = \sum_j \int \int \int \left(f_i' f_j' - f_i f_j \right) g_{ij} b db d\epsilon dV_j \quad (II-49)$$

where the superscript "1" denotes a post-collision value, g_{ij} is the pre-collision initial relative velocity, b is the impact parameter, m_i is the mass of the i^{th} species, X is an external force on the molecule, V is the velocity of the molecule and ϵ is a rotational impact parameter. The hydrodynamic equations of change (conservation of energy, conservation of momentum, etc.) are derived from the Boltzmann equation.

Hirschfelder, et al., use a perturbation method of successive approximations, which they attribute to Enskog, to obtain solutions to the Boltzmann equation. Using this method they derive a form for the perturbation function ϕ , that depends on space and time through the quantities, number density, mass average velocity and temperature, and their spatial derivatives:

$$\phi_i = -(A_i \partial \ln T / \partial r) - (B_i \partial V_0 / \partial r) + n \sum_j (C_i^{(j)} d_j). \quad (II-50)$$

The coefficients A_i , B_i and $C_i^{(j)}$ each represent rather involved integral equations which must be solved. They are solved by a series approximation method, using the infinite Sonine polynomial series. The Sonine polynomials are defined as:

$$S_n^{(m)}(x) = \sum_j [(-1)^j (m+n)! x^j] / [(n+j)! (m-j)! j!]. \quad (II-51)$$

Linear combinations of a finite number of these polynomials

are shown to be the solutions to the integral equations for A_i , B_i and $C_i^{(j)}$. However, the transport coefficients (which is what we are after) are expressed in terms of the Sonine polynomial expansion coefficients. These Sonine polynomial expansion coefficients involve complicated combinations of integrals, called "bracket" integrals. Chapman and Cowling (1939) express these bracket integrals as linear combinations of a set of integrals:

$\Omega_{ij}^{(1,s)} = (2\pi kT/\mu_{ij})^{1/2} \int_0^\infty \int_0^\infty (e^{-\gamma_{ij}^2}) \gamma_{ij}^{(2s+3)} (1-\cos^1(\chi)) b db d\gamma_{ij}$,
 (II-52), where μ_{ij} is the reduced mass of the colliding molecules i and j , γ_{ij} is the reduced initial relative speed of the colliding molecules, b is the impact parameter and χ is the angle of deflection of the molecules. Hirschfelder, et al., have tabulated values of these $\Omega^{(1,s)}$ integrals for frequently encountered bracket integrals in Table I-M of their text. Hirschfelder, et al., go on to define the transport coefficients in terms of these $\Omega^{(1,s)}$ integrals. It is these relations that we have used in our determination of Prandtl numbers for binary gas mixtures.

Before presenting these relations it is important to understand the assumptions used in this derivation and the limitations they impose, if any. Since the usual definitions of transport coefficients only apply under conditions only slightly displaced from equilibrium, our results are limited by this restriction.

Only binary collisions are considered, which limits us to densities low enough that three-body collisions are unimportant. The theory predicts that viscosity is independent of pressure at constant temperature. Hirschfelder, et al., state that experiments on nitrogen have shown that only a 4% deviation in viscosity occurs as pressure is varied from 1 to 60 atmospheres. Our operating condition of 10 atmospheres is well within this range and should therefore closely conform to the theory in this respect.

The theory limits itself to Classical Mechanics and thereby precludes low temperature situations where quantum effects become significant. These quantum effects are less than 1% for helium above 200 Kelvin (and even smaller for heavier isotopes). The coldest temperature we have achieved to date has been 193 Kelvin, under a no load condition, so our normal operations are all above 200 Kelvin and we are not concerned with quantum effects.

The Chapman-Enskog (1939) theory uses a first-order approximation in their perturbation method solution to the Boltzmann equation. This is only valid when the gradients of the physical quantities (density, velocity, temperature, etc.) are small. This means the changes in these properties over one mean free path must be small with respect to unity. Based on the mean free paths for gases at pressures above one atmosphere, this condition is satisfied

except under conditions of extreme gradients, such as those present in shock waves. Since the observed pressure waveforms in our resonators are sinusoidal, we do not have any shock waves and we are not restricted by this assumption.

The theory further assumes that the dimensions of the containing vessel and any obstacles within it are large compared to the mean free path, which provides no limitations for our gases and pressures. Although the Chapman-Enskog theory applies strictly to monatomic gases the results have been shown to be good even for polyatomic gases, provided that the molecules are not too non-spherical. Finally, the development of the theory results in a set of equations for transport coefficients which rely upon the previously discussed $\Omega^{(1,s)}$ integrals. These integrals are dependent upon the potential function that represents the molecular interactions. Throughout the derivation by Hirschfelder, et al., and in all of the equations used for our calculations, the Lennard-Jones (6-12) potential is assumed.

Now that we have presented the theory and its limitations we will present the equations necessary for the calculation of dynamic viscosity, thermal conductivity and isobaric specific heat capacity of a binary mixture of monatomic gases. From these, as we have already discussed, we get Prandtl number, where $\sigma = \eta c_p / \lambda$.

The dynamic viscosity for a binary gas mixture is given by:

$$[\eta_{mix}]_1 = \frac{1+Z_\eta}{X_\eta + Y_\eta},$$

where

$$X_\eta = \frac{x_1^2}{[\eta_1]_1} + \frac{2x_1x_2}{[\eta_{12}]_1} + \frac{x_2^2}{[\eta_2]_1},$$

$$Y_\eta = \frac{3}{5} A_{12}^\diamond \left\{ \frac{x_1^2}{[\eta_1]_1} \left(\frac{M_1}{M_2} \right) + \frac{2x_1x_2}{[\eta_{12}]_1} \left(\frac{(M_1+M_2)^2}{4M_1M_2} \right) \left(\frac{[\eta_{12}]_1^2}{[\eta_1]_1[\eta_2]_1} \right) + \frac{x_2^2}{[\eta_2]_1} \left(\frac{M_2}{M_1} \right) \right\},$$

and

$$Z_\eta = \frac{3}{5} A_{12}^\diamond \left\{ x_1^2 \left(\frac{M_1}{M_2} \right) + 2x_1x_2 \left[\left(\frac{(M_1+M_2)^2}{4M_1M_2} \right) \left(\frac{[\eta_{12}]_1}{[\eta_1]_1} + \frac{[\eta_{12}]_1}{[\eta_2]_1} \right) - 1 \right] + x_2^2 \left(\frac{M_2}{M_1} \right) \right\}$$

In these equations x_1 and x_2 represent the mole fractions of species 1 and 2, M_1 and M_2 represent the molecular weights of species 1 and 2 and $A_{12}^\diamond = \eta^{(2,2)\diamond} / \eta^{(1,1)\diamond}$, where the superscript \diamond refers to a value that takes into account the deviation of a particular molecular model (in our case the Lennard-Jones (6-12) potential) from the idealized rigid sphere model of molecular interactions. The values for $[\eta_1]_1$ and $[\eta_2]_1$ are given by the equation for a pure substance:

$$[\eta]_1 \times 10^7 = 266.93 (MT)^{1/2} / [\sigma^2 \eta^{(2,2)\diamond}(T^*)],$$

where η is dynamic viscosity in gm/cm-sec, T is temperature in $^\circ K$, $T^* = kT/\epsilon$ is reduced temperature, M is molecular weight, σ is collision diameter in angstroms and ϵ/k is the potential parameter in $^\circ K$. The remaining term $[\eta_{12}]_1$ represents an artificial quantity for a hypothetical pure

substance with molecules of molecular weight $2M_1M_2/(M_1+M_2)$, that interact according to a potential curve specified by interaction parameters σ_{12} and ϵ_{12} . These terms are described in terms of the Lennard-Jones (6-12) potential, where σ is the distance of closest approach (in angstroms) of two molecules which collide with zero initial relative kinetic energy, and ϵ is the maximum energy of attraction of the two molecules. $[\eta_{12}]_1$ is given by:

$$[\eta_{12}]_1 \times 10^7 = 266.93 [2M_1M_2T/(M_1+M_2)]^{1/2} / [\sigma_{12}]^{(2,2)} (T_{12}^*),$$

where the subscript 12 on individual terms refers to a combined value for species 1 and 2. The values for σ_{12} and ϵ_{12} are given by the empirical combining laws $\sigma_{12} = \frac{1}{2}(\sigma_1 + \sigma_2)$ and $\epsilon_{12} = (\epsilon_1 \epsilon_2)^{1/2}$, respectively, and T_{12}^* is given by $T_{12}^* = kT / \epsilon_{12}$.

The thermal conductivity for a binary mixture is given by:

$$[\lambda_{\text{mix}}]_1 = \frac{1 + Z_\lambda}{X_\lambda + Y_\lambda} \text{ in cal/cm-sec-}^\circ\text{K},$$

$$\text{where } X_\lambda = \frac{x_1^2}{[\lambda_1]_1} + \frac{2x_1x_2}{[\lambda_{12}]_1} + \frac{x_2^2}{[\lambda_2]_1},$$

$$Y_\lambda = \frac{x_1^2}{[\lambda_1]_1} U^{(1)} + \frac{2x_1x_2}{[\lambda_{12}]_1} U^{(y)} + \frac{x_2^2}{[\lambda_2]_1} U^{(2)},$$

$$Z_\lambda = x_1^2 U^{(1)} + 2x_1x_2 U^{(z)} + x_2^2 U^{(2)},$$

$$U^{(1)} = \frac{4}{15} A_{12} - \frac{1}{12} \left(\frac{12}{5} B_{12} + 1 \right) \frac{M_1}{M_2} + \frac{(M_1 - M_2)^2}{2M_1M_2},$$

$$\begin{aligned}
U^{(2)} &= \frac{4}{15} A_{12} \diamond - \frac{1}{12} \left(\frac{12}{5} B_{12} \diamond + 1 \right) \frac{M_2 (M_2 - M_1)^2}{M_1 2M_1 M_2}, \\
U^{(y)} &= \frac{4}{15} A_{12} \diamond \left(\frac{(M_1 + M_2)^2}{4M_1 M_2} \right) \frac{[\lambda_2]_1^2}{[\lambda_1]_1 [\lambda_2]_1} - \frac{1}{12} \left(\frac{12}{5} B_{12} \diamond + 1 \right) \\
&\quad - \frac{5}{32 A_{12} \diamond} \left(\frac{12}{5} B_{12} \diamond - 5 \right) \frac{(M_1 - M_2)^2}{M_1 M_2}, \\
U^{(z)} &= \frac{4}{15} A_{12} \diamond \left[\left(\frac{(M_1 + M_2)^2}{4M_1 M_2} \right) \left(\frac{[\lambda_{12}]_1}{[\lambda_1]_1} + \frac{[\lambda_{12}]_1}{[\lambda_2]_1} \right) - 1 \right] - \frac{1}{12} \left(\frac{12}{5} B_{12} \diamond + 1 \right), \\
[\lambda]_1 \times 10^7 &= 1989.1 \frac{(T/M)^{\frac{1}{2}}}{\sigma^2 \Omega^{(2,2)} \diamond (T_{12}^*)}, \\
[\lambda_{12}]_1 \times 10^7 &= 1989.1 \frac{(T(M_1 + M_2)/2M_1 M_2)^{\frac{1}{2}}}{\sigma_{12}^2 \Omega_{12}^{(2,2)} \diamond (T_{12}^*)}, \\
\text{and } B_{12} \diamond &= [5 \Omega^{(1,2)} \diamond - 4 \Omega^{(1,3)} \diamond] / \Omega^{(1,1)} \diamond.
\end{aligned}$$

The definitions for all terms are similar to those given for the dynamic viscosity relations.

The remaining quantity necessary for the calculation of Prandtl number is the isobaric specific heat capacity of the binary mixture. Huang (1976) gives a relation for this quantity: $c_{pmix} = \sum m_i c_{pi} / m = \sum x_i M_i c_{pi} / \sum x_i M_i$, where x_i is the mole fraction of species i , M_i is the molecular weight of species i and c_{pi} is the isobaric specific heat capacity of species i . The required units of this quantity, for compatibility with the previous equations are cal/gm-°K.

All of these equations were formed into the Fortran computer program presented in Appendix A. Outputs

have been created (from this program) for temperatures of 200°K and 300°K, and for mixtures of helium-xenon and helium-argon, for all concentrations from 100% helium to 0% helium. A composite plot showing all of these cases is provided as Figure II-3. It is clear from these curves that the Prandtl number variation with concentration is just as predicted by the qualitative analysis, given in the first part of this section.

3. Selection of a Gas Mixture

Now that we have shown how the sound speeds and Prandtl numbers of binary gas mixtures vary with concentration, it is necessary to consider how each of these parameters affect performance. We know from the thermoacoustic theory, presented in section A of this Chapter, that power density will decrease with reduced sound speed (due to the increased mass), and that COP will increase with reduced Prandtl number. However, as Prandtl number decreases, due to the addition of a heavy gas, the overall mass of the gas increases, and sound speed is reduced. It is therefore necessary that the mixture have as low a Prandtl number as possible while the mass increase is kept to a minimum (and therefore the reduction in sound speed is minimized). Looking at Figure II-3 it is clear that we need a mixture that is at a point on the very steeply sloped section of the curve, as the concentration begins to deviate from pure helium. Our selection of 12.5%

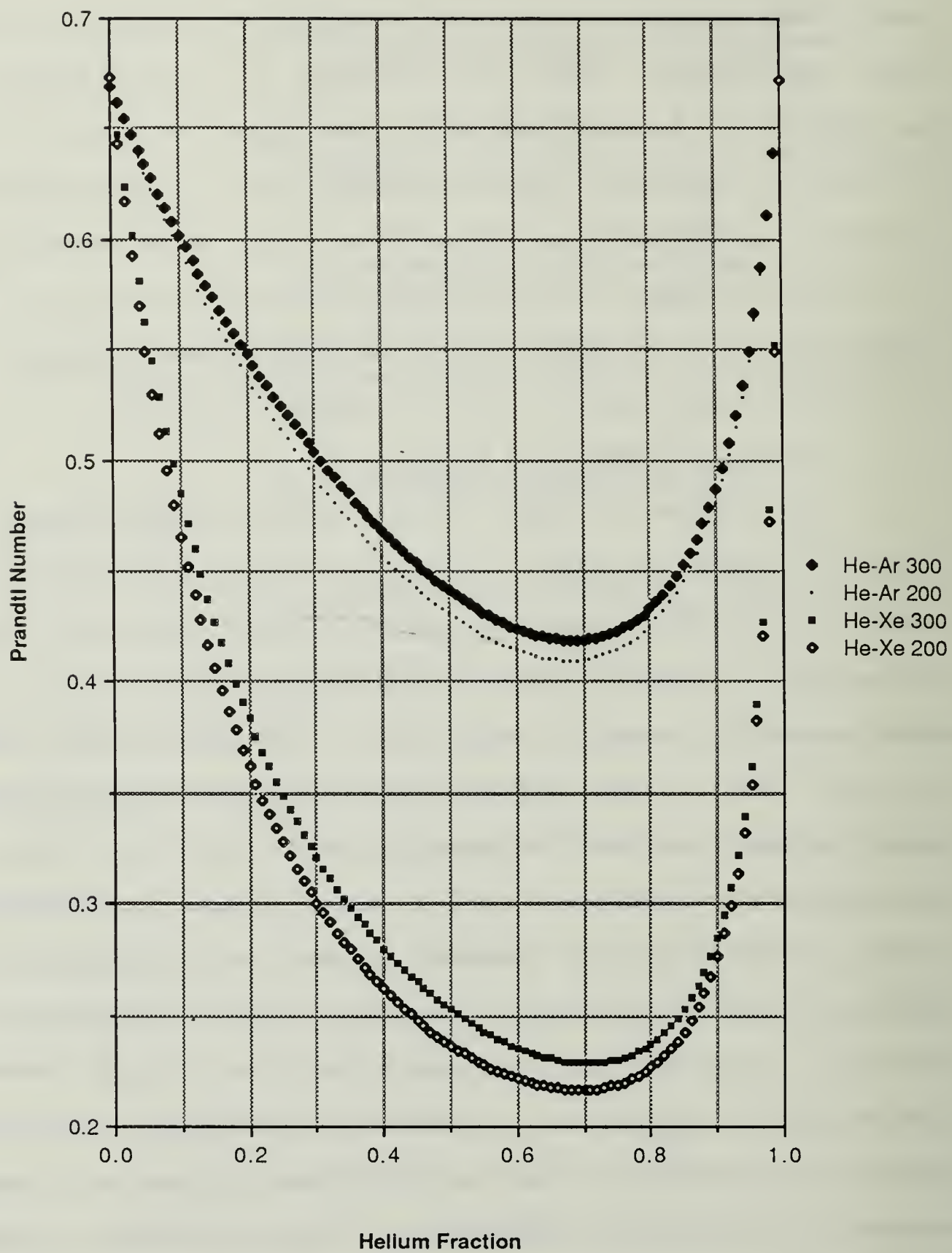


Figure II-3. Prandtl Number vs. Helium Fraction

xenon and 18.5% argon in our helium-xenon and helium-argon mixes, respectively, was made based on this requirement. With the xenon we achieved approximately 90% of the maximum possible Prandtl number reduction, while getting only 40% of the possible Mass increase. With argon we once again achieved about 90% of the maximum possible Prandtl number reduction but got approximately 60% of the possible mass increase. The results of these selections will be discussed in Chapter V.

C. STACK DESIGN THEORY

The purpose of this section is to explain the differences between the two stacks built for this project and that used in previous experiments, including the basis for any and all modifications. To provide an orderly flow of information, the differences between the stacks will be fully described and then an explanation of each of the new features will be given. Details of stack construction are provided in Chapter III.

We will discuss three stacks in this section: the original stack, built by Dr. Tom Hofler, will be referred to as the "old" stack, the first stack built for this experiment will be referred to as the "new" stack, and the second stack built for this experiment will be referred to as the "dual" stack. The actual designs for all of the stacks are based on the work and ideas of Dr. Hofler. All

of the stacks have the same outer diameter of 1.506 inches and the same size center post with a 0.25 inch diameter. Additionally all three have the same plate thickness of 0.003 inches, and were built using a loom, discussed in Chapter III, with a line spacing of 0.2 inches. The primary differences between the stacks are in the areas of average plate spacing, overall stack length, and final arrangement of the fishing line used to provide the plate spacing.

The old stack has an overall length of 3.089 inches with an average plate spacing of 0.0140 inches, with no modifications to the fishing line arrangement. The new stack has an overall length of 3.066 inches with an average plate spacing of 0.0133 inches. Additionally, it has a special pattern cut into the fishing line, as shown in Figure II-4. The dual stack has an overall length of 3.068 inches with an average plate spacing of 0.016 inches at the hot end and 0.035 inches at the cold end. There is no pattern cut into the fishing line of the dual stack, however, there is a gap of approximately 0.75 inches between the rows of thin lines and thick lines, as shown in Figure II-5. Additionally, on the layer of plastic with both sizes of fishing line, every other piece of the thick fishing line has been removed, starting at a point 18 inches from the end of the plastic sheet that is at the center of the roll. The only remaining difference between the stacks is that the old and new stacks have center posts

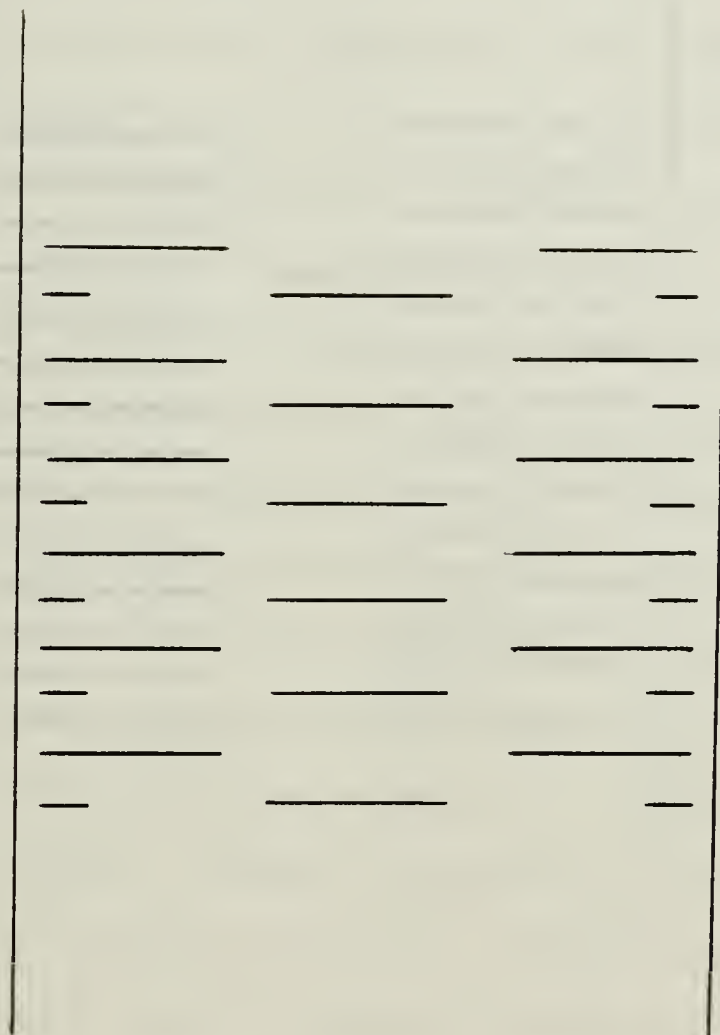


Figure 11-4. New Stack String Arrangement

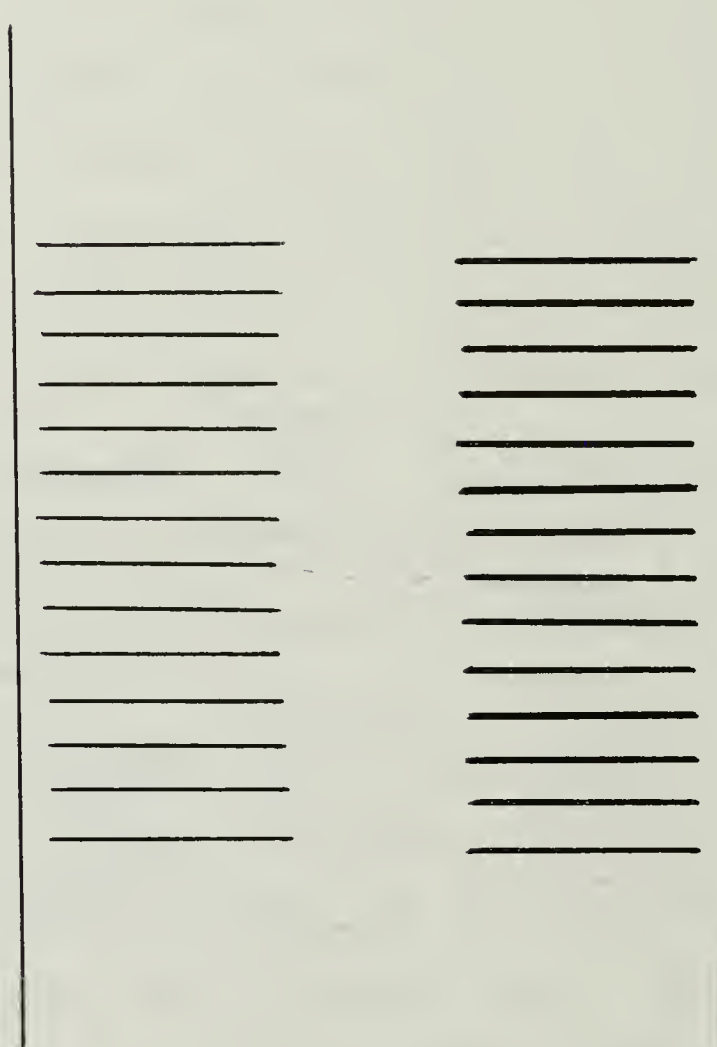


Figure 11-3. Dual Stack String Arrangement

of a cloth phenolic type rod and the dual stack has a nylon plastic type rod. This last difference is strictly due to availability of material at the time of construction and is not considered to be of any significance in relation to refrigerator or stack performance.

Each of the modifications, relative to the old stack, will now be explained, beginning with those for the new stack. The changes in this stack are primarily intuitive in nature, based on experiments by Hofler and Wheatley, and therefore do not lend themselves to quantitative analysis. The change in overall length was selected to provide a space between the end of the stack and primarily the cold heat exchanger. This space is desired to preclude any flow restrictions that could occur with the stack plates resting against the plates of the heat exchanger surface. A piece of fishing line (approximately 0.020 inches in diameter) was glued to the end of the stack, to fill the void left by the reduced length, thereby preventing the stack from moving around in the resonator relative to the heat exchangers. The pattern of Figure II-4 was selected for two reasons. Since the amount of heat transport is related to the total surface area of the plates, the removal of some of the fishing line would increase this surface area and thereby increase the heat transport. Also, since it is virtually impossible to have precisely uniform spacing of the fishing line and plates, there are slight differences

in the longitudinal flow channels in the stack. This in turn can produce flow variations and pressure differences from one channel to the next. Due to there being no continuous pieces of fishing line along the full length of the stack, with this pattern, the channels are all interconnected and the pressure and flow differences, if any, will be minimized. The overall result of this pattern was a reduction of approximately 50% in the amount of fishing line present in the stack. This reduction should also have the effect of reducing the overall obstruction to flow in the resonator. It should also be noted that this pattern may have had a significant effect on the degree of crush experienced during the rolling process, resulting in the smallest average plate spacing of any of the stacks. This plate spacing is very important in the thermoacoustic performance of the refrigerator.

The changes in the dual stack are somewhat more complex and theoretical in nature. Within the accuracy of construction methods, the overall length of the dual stack is the same as that of the new stack, for reasons explained above. The removal of every other piece of the thick fishing line, after the first 18 inches, is based on reducing the overall amount of fishing line in the stack, as discussed for the new stack. All lines were left intact for the first 18 inches to provide a more uniform plate spacing toward the center of the roll, where the diameter

of the roll is not very large with respect to the fishing line spacing. The 0.75 inch gap between the rows of thin and thick strings was used for two reasons. A certain minimal gap is necessary to prevent the inner plastic layer, on the hot end, from butting up against the thick strings when the ends of the stack are pushed together. The extra distance, out to 0.75 inches, was used to give approximately the same total length of string as we had in the new stack.

Understanding the reasons for the dual nature of the stack requires some knowledge of the basic characteristics of large temperature span refrigerators, as well as the basic heat transfer process that occurs in the stack. The heat flow at the two ends of the stack is not the same, generally being significantly higher at the hot end, where heat is rejected. This difference is functionally dependent on efficiency and increases with reduced efficiency. To properly explain this effect some terms must be introduced. Although the following relations are simplified they are adequate for the explanation of this effect. The heat transfer capacity q is given by:

$$q(x) = Q(x) / (r(x) - 1) = -\pi \delta_k p(x) u(x), \quad (\text{II-52})$$

and the local heat flow Q is given by:

$$Q(x) = -\pi \delta_k p(x) u(x) (r(x) - 1), \quad (\text{II-53})$$

where $r(x) = \nabla T / \nabla T_{\text{crit}}$, ∇T_{crit} is the maximum temperature gradient in the x direction, π is the surface area per unit

length of the stack, $p(x)$ is the acoustic pressure distribution, $u(x)$ is the acoustic velocity distribution, δ_K is the thermal penetration depth (which according to Swift (1989), is the distance that heat can diffuse through the fluid during the time $1/\omega$), and x is the longitudinal distance along the stack. In a standard stack $u(x)$ and $r(x)-1$ are the only parameters that vary significantly in the longitudinal direction. The quantity $r(x)-1$ represents the temperature gradient perpendicular to the x direction (i.e. the transverse direction). This quantity will vary greatly, depending on heat load, and must be large in order to transfer large amounts of heat. In a large temperature span refrigerator $|r(x)-1|$ is very small at the cold end and large at the hot end. The $Q(x)$ distribution is dominated by $|r(x)-1|$. Conversely, $u(x)$ is generally small at the hot end of the stack and large at the cold end. It is $u(x)$ that dominates the $q(x)$ distribution. These effects give a low heat flow at the cold end, where the heat transfer capacity is highest, and a high heat flow at the hot end, where the heat transfer capacity is lowest.

The object of the dual stack design is to reduce this conflict by changing the distribution of $q(x)$, making it more uniform and similar to that of $Q(x)$. Since $r(x)-1$ must be greater than zero to transfer heat, and is very dependent on heat load, it was determined that $q(x)$ was the quantity that should be modified. To accomplish this, the acoustic

velocity distribution had to be countered by some other effect. The only parameter affected enough by stack design to accomplish this is Π . By varying the amount of surface area along the stack length the $q(x)$ distribution can be altered. By having half the number of plates at the cold end, we cut the surface area by a factor of two, essentially countering the $u(x)$ distribution, and making the capacity for heat transfer correspond more closely to the actual heat flow conditions. Ideally, the surface area should vary continuously in the longitudinal direction to precisely counter the velocity distribution and produce an exactly uniform $q(x)$ distribution, thereby giving optimum results. This situation would be much more difficult to construct and methods that have been discussed to date have other drawbacks that make them less acceptable than the current design. Although this is the major reason for an expected increase in the COP with the dual stack design there are two other minor effects which should also help. An area not covered by the simplified equations above is that of viscous friction as the gas moves along the plates. The energy loss due to this friction is proportional to both the square of the acoustic velocity and the total surface area exposed to the gas. Since the surface area has been cut in half at the cold end, where the velocity is highest, this source of energy loss should be significantly reduced, thereby increasing the COP. The second area of

interest relates to the uniformity of the $q(x)$ distribution. Since $q(x)$ depends on $u(x)$, anything that makes $u(x)$ more uniform will also make $q(x)$ more uniform, which in turn tends to improve the COP. The velocity distribution will depend somewhat on the degree of blockage in the flow path. The plates have an "effective" size that is larger than their thickness, due to viscous effects. By reducing the number of plates the degree of blockage is reduced and the velocity distribution is more uniform, thereby tending to increase the COP.

III. STACK CONSTRUCTION

The thermoacoustic stack, necessary for the transport of heat as discussed in chapter II, consists of a continuous roll of very thin plastic, the layers of which are separated by spacers attached to the plastic surface. This geometry was selected instead of a parallel plate arrangement based on both ease of construction and structural rigidity of the finished product. When the dimensions of a stack are considered, plate spacing of 0.015 inches (or 0.033 inches depending on which stack), plate thickness of 0.003 inches, overall diameter of 1.506 inches, and overall length of about 3.066 inches, it is easily seen that the parallel plate geometry would be much more difficult to construct and extremely fragile. The plastic used in this experiment was a polyester Mylar TM type. There was no particular reason for this selection other than ease of handling. The plate spacers consist of strips of high grade monofilament nylon fishing line which are affixed to the plastic surface using a spray adhesive.

Prior to construction, decisions must be made concerning overall length of the stack, which determines the width of the plastic sheet, required diameter, which determines the overall length of the plastic sheet and, approximate plate spacing, which determines the size of spacers to be

attached to the plastic surface. For this project two stacks were built. The first had an overall length of 3.066 inches, with a diameter of 1.506 inches and 0.015 inch spacers. The second was a dual stack with the same diameter, an overall length of 3.068 inches and spacers of 0.015 inches, with two layers of plastic along half of its length, and spacers of 0.033 inches along the other half. This provided a variable plate spacing for reasons discussed in chapter II. The overall length of plastic sheet needed to make a stack can be determined by mathematical analysis of the spiral wound roll once the dimensions are specified. The resulting equation for length is $L = (\pi/d)(r_1^2 - r_0^2)$, where d is the sum of the spacer size and plate thickness, r_1 is the radius of the stack (and also the radius of the resonator bore), and r_0 is the radius of the center post, on which the plastic is rolled. The center posts that have been used are 0.25 inch diameter and are either cloth phenolic or a nylon type plastic rods. Usually a safety margin of twelve to eighteen inches is added to the length calculated by the above equation. This is due to the fact that a precise fit is desired in the resonator bore and it is easier to trim small pieces from an oversized roll than to add pieces to one that is undersized. The width of the plastic sheet is cut very precisely using a sharp paper cutter, with a guide that has been carefully positioned to the desired width. This method

has provided results with an accuracy of 0.002 inches. The overall length of plastic sheet used for the two stacks in this experiment was 120 inches for the first stack and two pieces of 60 inches each for the dual stack.

Once the plastic sheet has been cut to size and fishing line of the required size has been acquired, construction can begin. The spray adhesive used in this experiment was 3M brand Super 77 spray adhesive. Since attaching individual pieces of fishing line would be very time consuming and result in a less than uniform spacing an alignment device is used to assist in this process. An aluminum loom has been constructed to provide uniform parallel spacer positioning on the plastic surface. A long piece of fishing line is wound around the hooks of the loom, positioned in grooves to provide parallellism, and fixed at both ends with screws to hold it in place. The loom has an open front and back to provide access to both sides of the fishing line. Using a spray shield to protect the loom, spray adhesive is applied to the front side of the fishing line. The loom is then turned over and aligned over the plastic to provide parallel, uniform positioning of the strips of fishing line. Once positioned the loom is set down and a smooth aluminum block is used to press the fishing line onto the surface. The working surface and press used in this experiment were smoothly polished aluminum blocks, which were necessary to provide a

relatively uniform compression of the fishing line when pressing. A teflon sheet was placed under the plastic and over the working surface to prevent the strings, which extend beyond the plastic, from sticking to the working surface. A sketch of the loom, with fishing line attached is shown positioned over the plastic sheet in Figure III-1. The distance between strips of fishing line on the loom used in this experiment was 0.20 inches. This spacing was selected based on experiments conducted by Dr. Tom Hofler at the Naval Postgraduate School. The loom covers a length of six inches and therefore requires twenty repetitions of this procedure to complete a stack. The dual stack required more repetitions due to there being two different string sizes on one plastic sheet and a second layer of plastic of half the width, as shown in Figure III-2. Once the fishing line is pressed down and allowed a minimal drying time of one to two minutes a scalpel or razor blade is used to cut the fishing line off at the edge of the plastic. It should be noted that if the line is wound on the loom with too much tension the plastic will tend to curl when the line is cut. This is obviously an undesirable situation so care must be taken when winding the line on the loom to provide just enough tension to maintain the strips in the grooves. After all of the fishing line is attached to the plastic some trimming must be done prior to rolling. The fishing line is carefully cut back approximately one

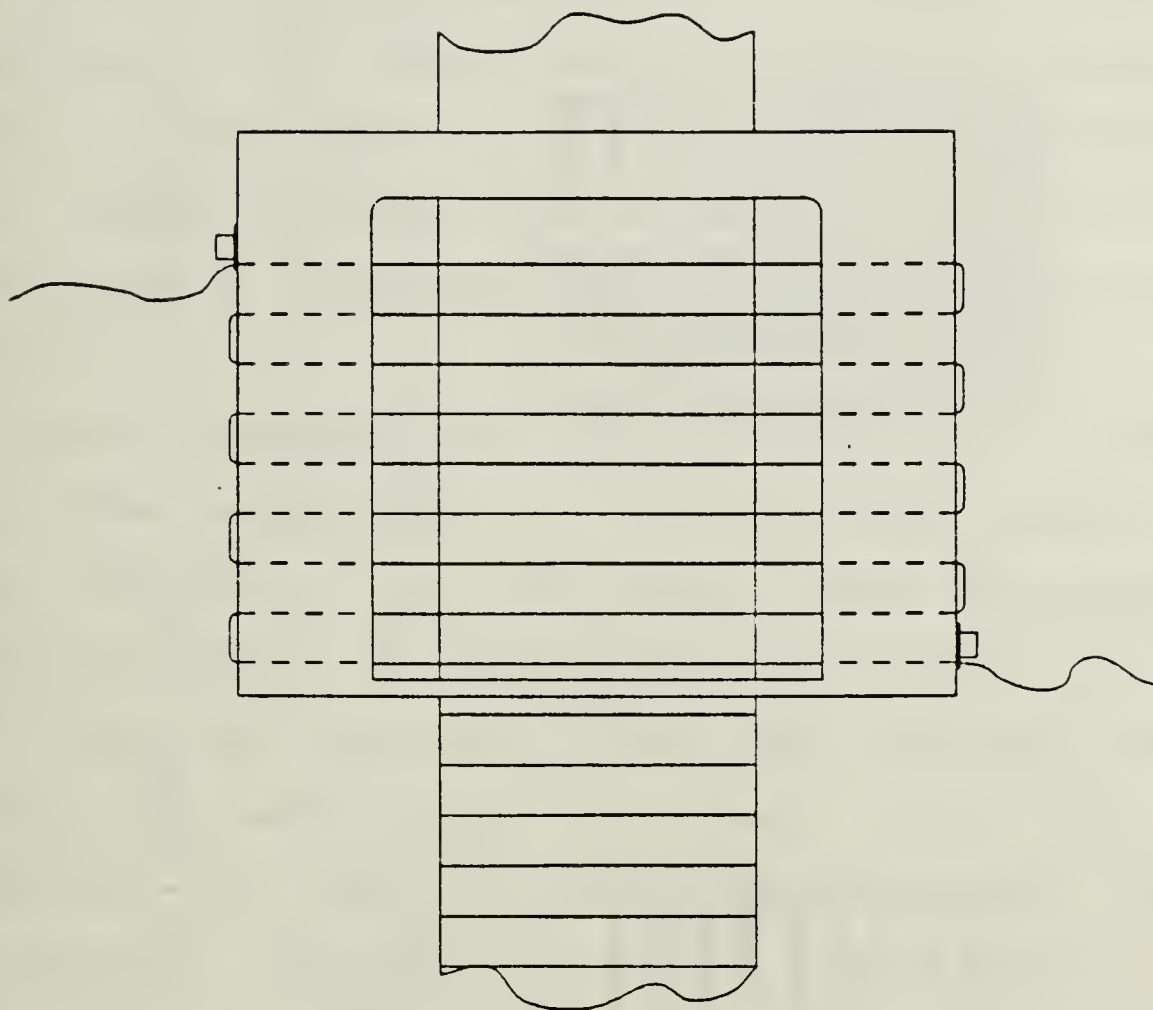
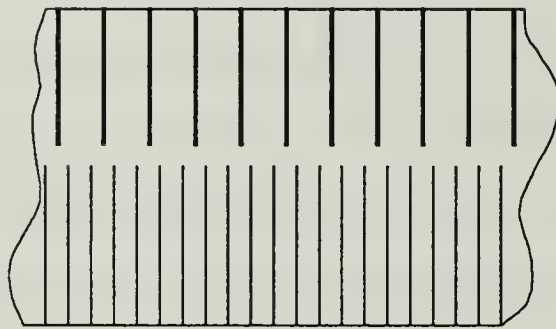


Figure III-1. Stack Construction Illustration



(a) Two strips of plastic film with line spacers adhered. The right strip has both thin & thick lines adhered.



(b) The narrow strip has been placed on top of the wide strip & is ready to be rolled up lengthwise (from bottom to top).

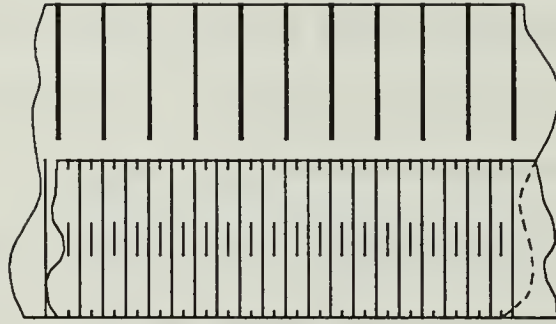


Figure III-2. Dual Stack Construction Arrangement

sixteenth of an inch from each edge, to prevent potential flow problems at the heat exchanger interfaces. Additionally, depending on the stack design, a pattern is cut in the strings or some strings are removed, for reasons explained in the stack theory of chapter II. Great care should be exercised in the trimming of any patterns to avoid making any large cuts in the plastic surface as this could produce significant flow variations during operation of the unit.

After completing this process the stack is ready to roll. The center post is carefully taped, using scotch tape, to the end of the plastic sheet. The plastic is carefully rolled up, using just enough tension to maintain the shape and provide uniform layer spacing, without getting too much crush, which would result in a layer separation much smaller than the string diameter. This is in general the most difficult part of the stack construction process. The uniform layer spacing is checked visually by holding the stack up to a light or using some sort of magnifying device. The spacing can also be checked quantitatively based on the known inner post diameter, the measured outer diameter and a count of the number of layers along several radii. This will provide an average layer spacing which will in general be somewhat smaller than the sum of the fishing line diameter and the plastic thickness. This is due to a certain degree of crush or

compression during the pressing and rolling processes. After rolling, even with a great deal of care, there will be some degree of spreading, or misalignment, at the ends of the cylinder. Using two smooth surfaces the ends of the stack can be pressed and the layers will slide into position to give flat ends and an overall length as precise as the width of the plastic sheet.

Drawings of the two ends of the dual stack are shown in Figures III-3 and III-4. The other stack has the same appearance as the dense or hot end of Figure III-3. Polaroid photographs of the actual dual stack, showing a radius from the center post out, at a 6.4x magnification, are provided as Figures III-5 and III-6. The finished roll is then trimmed down in diameter, by cutting small pieces off the length of the plastic strip, to fit snugly in the resonator bore. The final product is taped along the seam, with scotch tape, to hold the roll in the cylindrical shape.

Although some of the differences between the two stacks that were built for this experiment are mentioned in here, the details of and reasons for the differences are presented in the stack theory of chapter II.

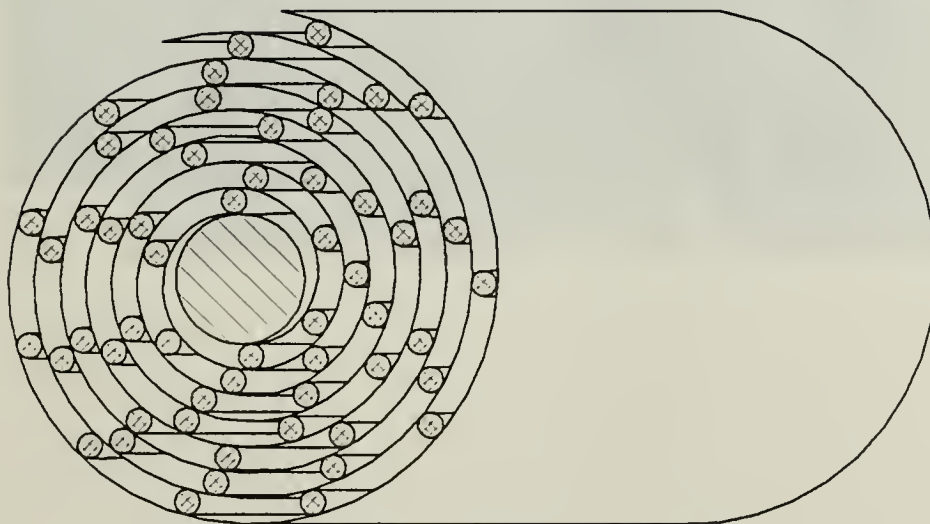


Figure III-3 Looking down on to the Hot End of the Dual Stack

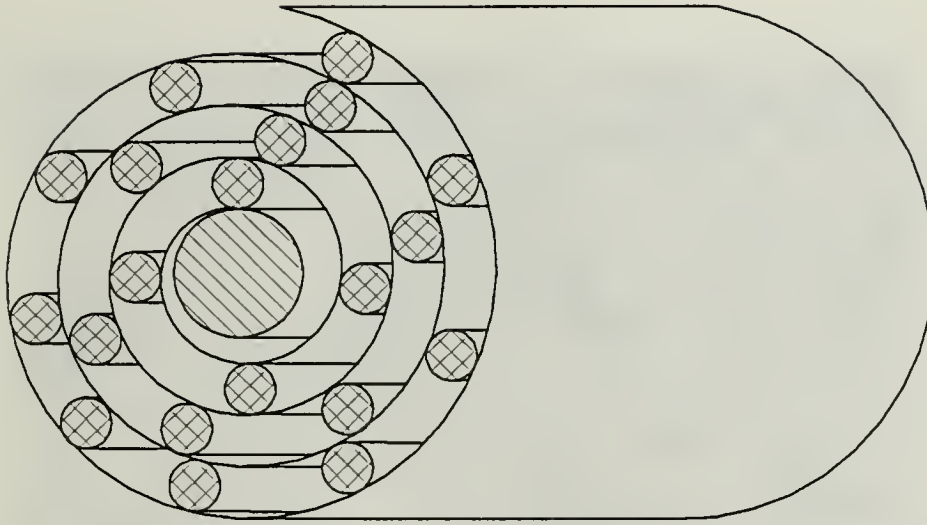


Figure III-4. Looking Down on to the Cold End of the Dual Stack

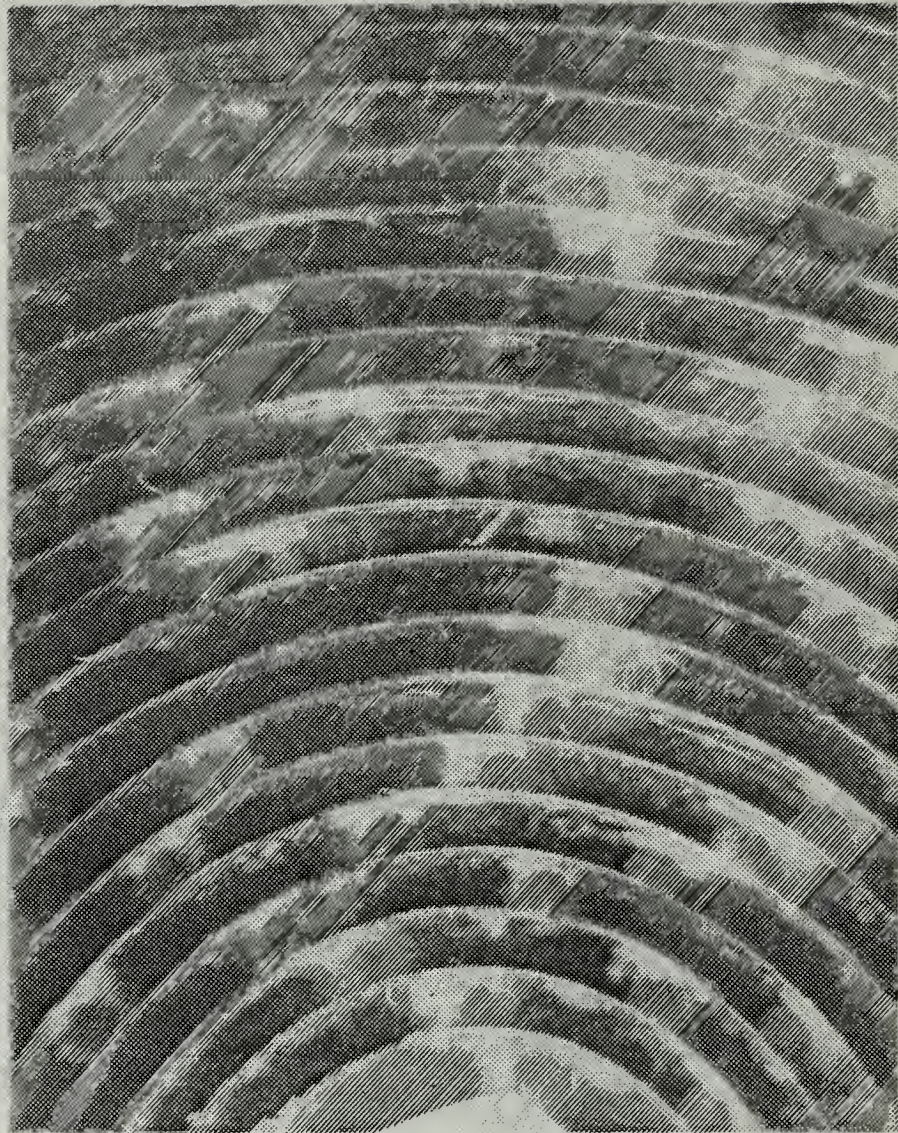


Figure III-5. Photograph of Dual Stack, Cold End, at 6.4x Magnification



Figure III-6. Photograph of Dual Stack, Hot End, at 6.4x Magnification

IV. EXPERIMENTAL APPARATUS AND PROCEDURES

In this Chapter we will present a description of our experimental apparatus, including the electronics used, and a discussion of our experimental procedure. We have used the prototype thermoacoustic refrigerator, and associated electronics package, that was built by Hofler (1986,1988). We have paraphrased sections of his discussion of the system as necessary to provide a basic understanding of the apparatus and its operation.

A. DESCRIPTION OF APPARATUS

In order to properly describe the apparatus it is necessary to break it down into two major areas; that of the high intensity driver, with its instrumentation for acoustic power measurements and that of the refrigeration components (resonator, stack, heat exchanger, etc.).

1. The Driver and its Instrumentation

The driver consists of a modified commercial loudspeaker, shown in Figure IV-1. The modifications consist of removal of the original plastic housing and fabric dome and attachment of a thin-wall aluminum cone-shaped piston and a surround. Figure IV-1 shows the unit with a voice coil and former 1, iron pole pieces 2, magnet 3, aluminum piston 4, surround 5, aluminum pressure vessel

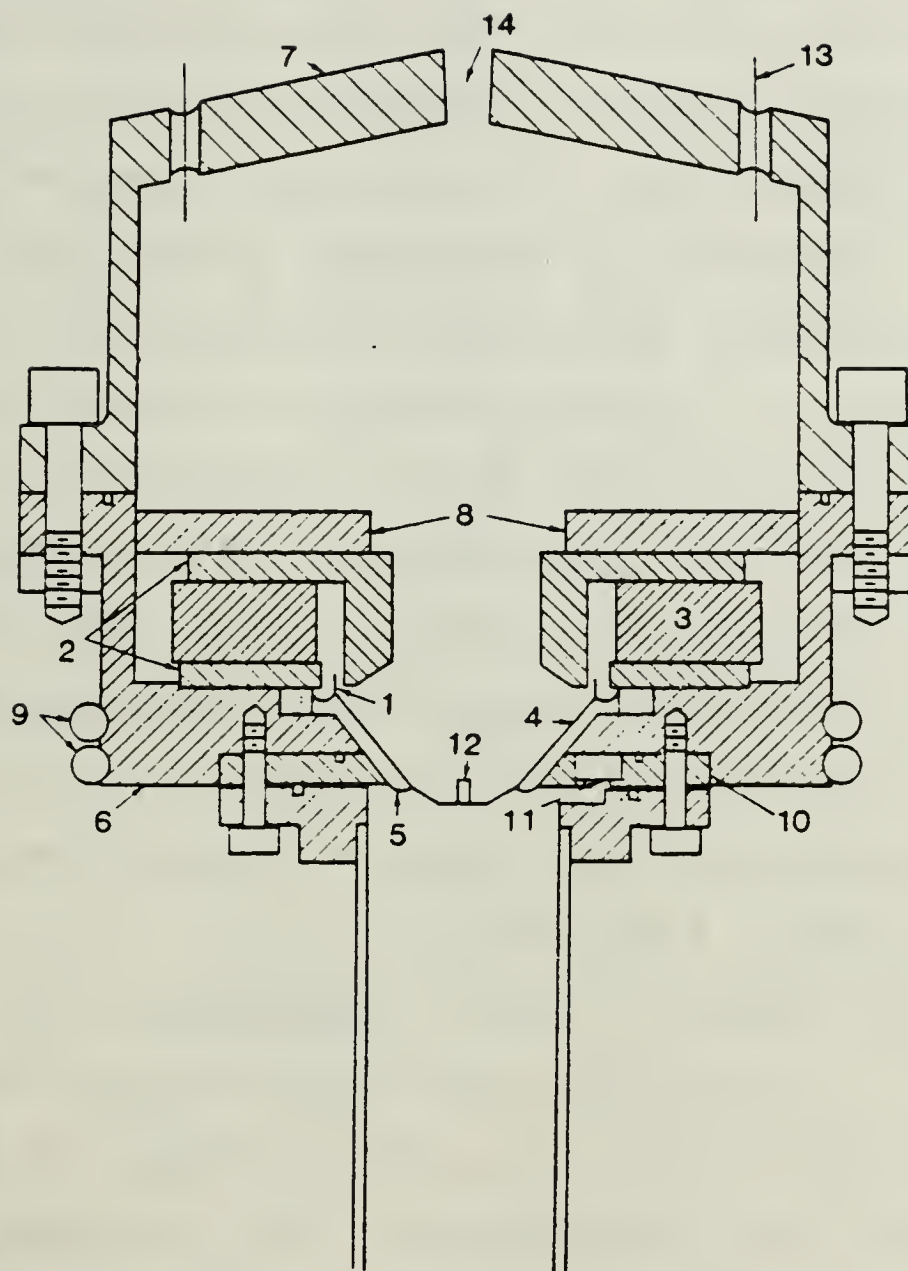


Figure IV-1. Schematic of Driver Apparatus Showing Acoustic Motor, Transducers, and a Portion of a Resonator. Numbered Parts are Identified in the Text.

6 and 7, aluminum plate 8, cooling water tubes 9, annular plate (where pressure transducer is mounted) 10, dynamic pressure transducer 11 and a post for the mounting of an accelerometer 12. The unit has a two inch diameter voice coil and an effective piston driving area of 0.93 square inches. Additionally, it has a high power capability that is made possible by suspending ferrofluid in the magnet gap, to conduct heat from the voice coil. A capillary filled hole is located adjacent to the surround to break the gas seal provided by the surround. The flow impedance of the capillary was chosen to be as low as possible without affecting the acoustic power measurements. The assembly is housed in the aluminum pressure vessel 6 and 7, and the resonator section is bolted to 6. The heat removed by the water cooling tubes 9, is conducted through the aluminum housing 6 and plate 8.

The dynamic pressure transducer 11, is physically attached to the structure of the driver and can therefore be calibrated along with other aspects of the driver, independent of the resonator. The transducer itself was designed and built by Dr. Hofler. It consists of a thin y-cut quartz crystal disk with evaporated electrodes and a miniature FET impedance converter circuit that buffers the output signal. The dynamic pressure transducer provides a low noise, low distortion, phase accurate signal which is calibrated to determine the volume velocity in a small

calibration cavity that can be attached to the driver. This, in conjunction with the integrated accelerometer signal (which is then a velocity signal) and the phase difference between the two, provides for an accurate measurement of the acoustic power provided to the resonator. Hofler's calibration of the pressure transducer was accomplished by comparison to a "standard" transducer that had previously been calibrated to an accuracy of $\pm 1\%$, by Swift, et. al. (1982), resulting in a sensitivity of 1.292 ($\pm 1\%$) volts/bar. The accuracy of the acoustic power measurement is $\pm 3\%$, as shown by Hofler (1988).

As previously noted in the discussion of Figure IV-1, the accelerometer is mounted on the post 12, which is attached to the back side of the piston 4. The post is necessary to thermally isolate the accelerometer from the piston (which becomes warm during operation) and to position the accelerometer where its cable has clearance from the piston wall. The accelerometer is a shear piezoceramic type. The piston's velocity signal (which is the integrated output of the accelerometer) is calibrated with the dynamic pressure transducer signal using a small volume of known acoustic impedance, to get an accurate value for volume velocity. This calibration may change as the properties of the surround change with use and must therefore be repeated at periodic intervals, to maintain the accuracy of results. Repeated calibrations, over a two

year period, have shown that the sensitivity of the pressure transducer has been stable within about 0.1%, while the volume velocity calibration value has shown an overall decrease of about 7%. It should be noted that the volume velocity value dropped just over 4% during the first four months of driver use, and dropped only 3% more over the next 18 months.

2. Refrigeration Components

The main components of the refrigeration section are shown in Figure IV-2. The resonator (18, 20 and 21 in the figure) is constructed of several parts. Where temperature uniformity is desired heavy-gauge copper is used. In section 18, containing the stack 17, there is a large temperature gradient and an epoxy-fiberglass substance is used to provide high strength with very low thermal conductance. This epoxy-fiberglass section, by itself would be very permeable to gas diffusion if left alone. To correct this situation, Dr. Hofler evaporated a thin film of indium over the outside of the fiberglass section, and then wrapped more fiberglass over the metal film.

The primary refrigeration component is the stack (17 in the Figure IV-2) which is constructed of a long sheet of plastic that is spiral wound on a 0.25 inch diameter plastic or cloth phenolic rod 16. The layers of plastic are separated by monofilament fishing line spacers. The details of stack construction were presented in Chapter III.

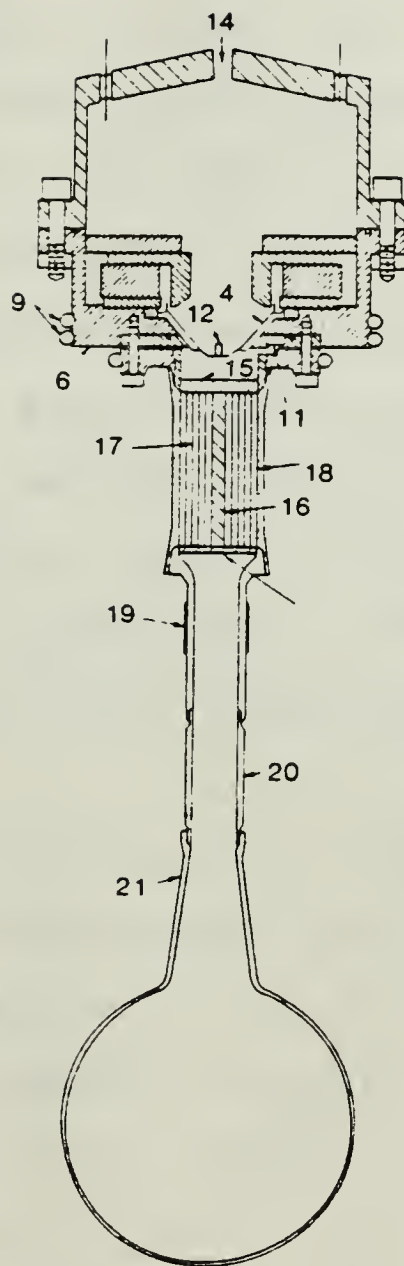


Figure IV-2. The Primary Refrigerator Components, Shown Attached to the Driver Assembly. The Numbered Components are Discussed in the Text.

The other components of importance in the refrigeration section are the hot and cold heat exchangers 15 and 22 in Figure IV-2, respectively. The hot heat exchanger provides for removal of heat from the unit, to prevent overall heating of the stack during operation. The cold heat exchanger provides good thermal contact with the applied heat load, from the heater coil 19. Dr. Hofler constructed the heat exchangers using electroplating and a chemically removable aluminum form, shown in Figure IV-3 prior to removal of the aluminum. The resulting heat exchangers had parallel copper strips with the planes of the strips parallel to the tube axis. The details of this construction are provided in the doctoral dissertation of Hofler (1986).

The remainder of the physical apparatus consists of a vacuum system, that attaches below the driver housing, thereby enclosing the entire refrigeration section, and a section of super-insulation wrapped around the resonator. All of this is to provide thermal insulation, thereby reducing nuisance heat loads. A layer of super-insulation consists of a layer of glass micro-fiber web followed by a layer of aluminized polyester film. The entire resonator section is wrapped with 10 to 12 of these layers. The vacuum system uses an ion gauge to monitor the vacuum, which varies between 3×10^{-4} and 5×10^{-6} torr during operation, depending on operating conditions and gas types.

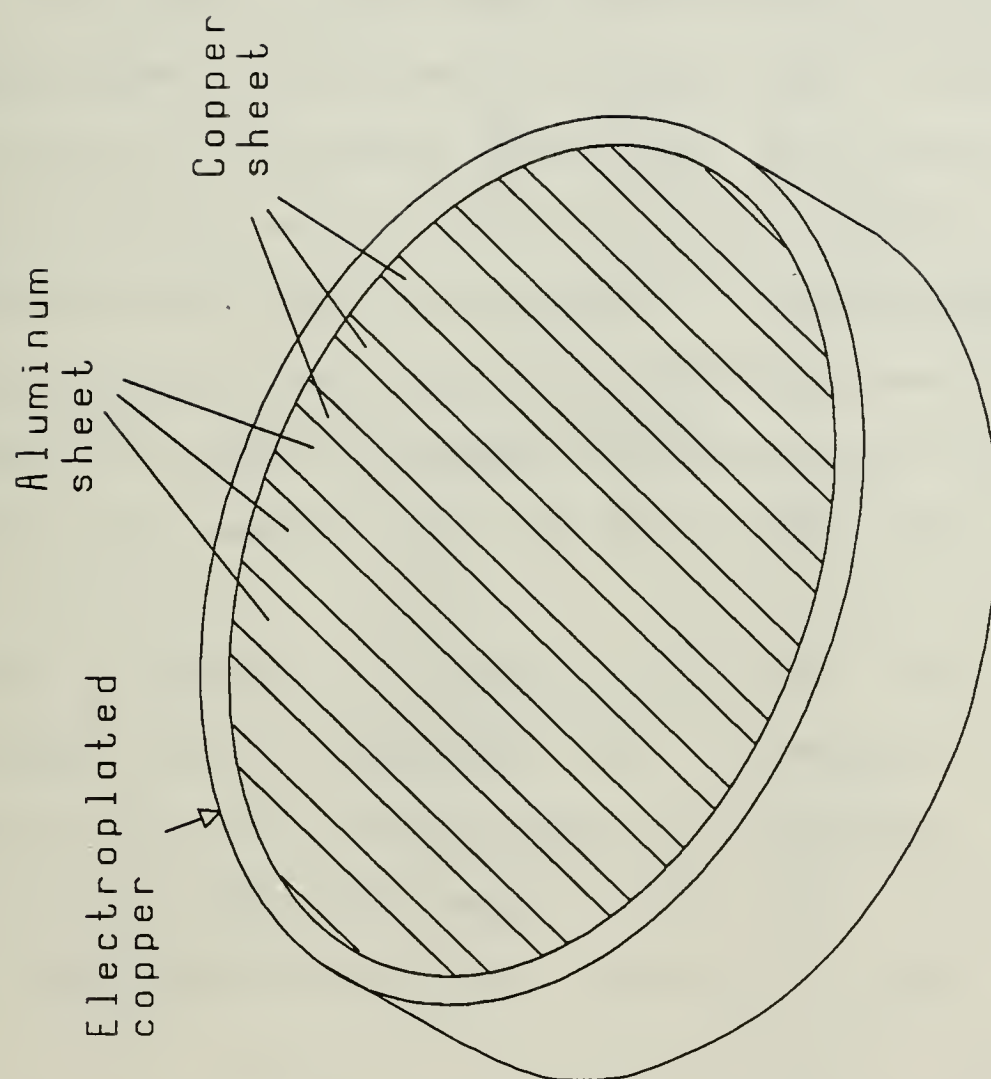


Figure IV-3. A Composite Copper and Aluminum Heat Exchanger Part. Prior to the Chemical Removal of the Aluminum

B. DESCRIPTION OF ELECTRONICS

The electronics portion of our experimental apparatus consists of two primary sections. These are the control and protective section and the data monitoring section. The control and protective systems will be discussed here and the data monitoring aspects will be covered in the next section, where we discuss the experimental procedure.

The control and protective electronics system provides feedback control of the drive frequency and amplitude, protection against burn-up of the driver voice coil, and signal conditioning to increase the precision of acoustic power measurements. The protective circuit is particularly important in our situation because the required operating conditions are very close to the maximum limits of the driver.

Figure IV-4 is a block diagram of the control circuits for drive frequency and amplitude. This figure is reproduced, with minor equipment updates, from the doctoral dissertation of Tom Hofler (1986). The explanation of its operation, for the most part, is quoted here for completeness:

"The frequency control is based on a lock-in amplifier that is used as a phase null detector with an analog output. The velocity signal is fed into the lock-in preamp, and the pressure signal is used as a reference channel input. The level of this reference signal is adjusted to be 1 V rms, in order to minimize lock-in phase errors. The Y-channel output voltage of the lock-in is proportional to the measured phase deviation and is fed into a simple integrating controller. The controller

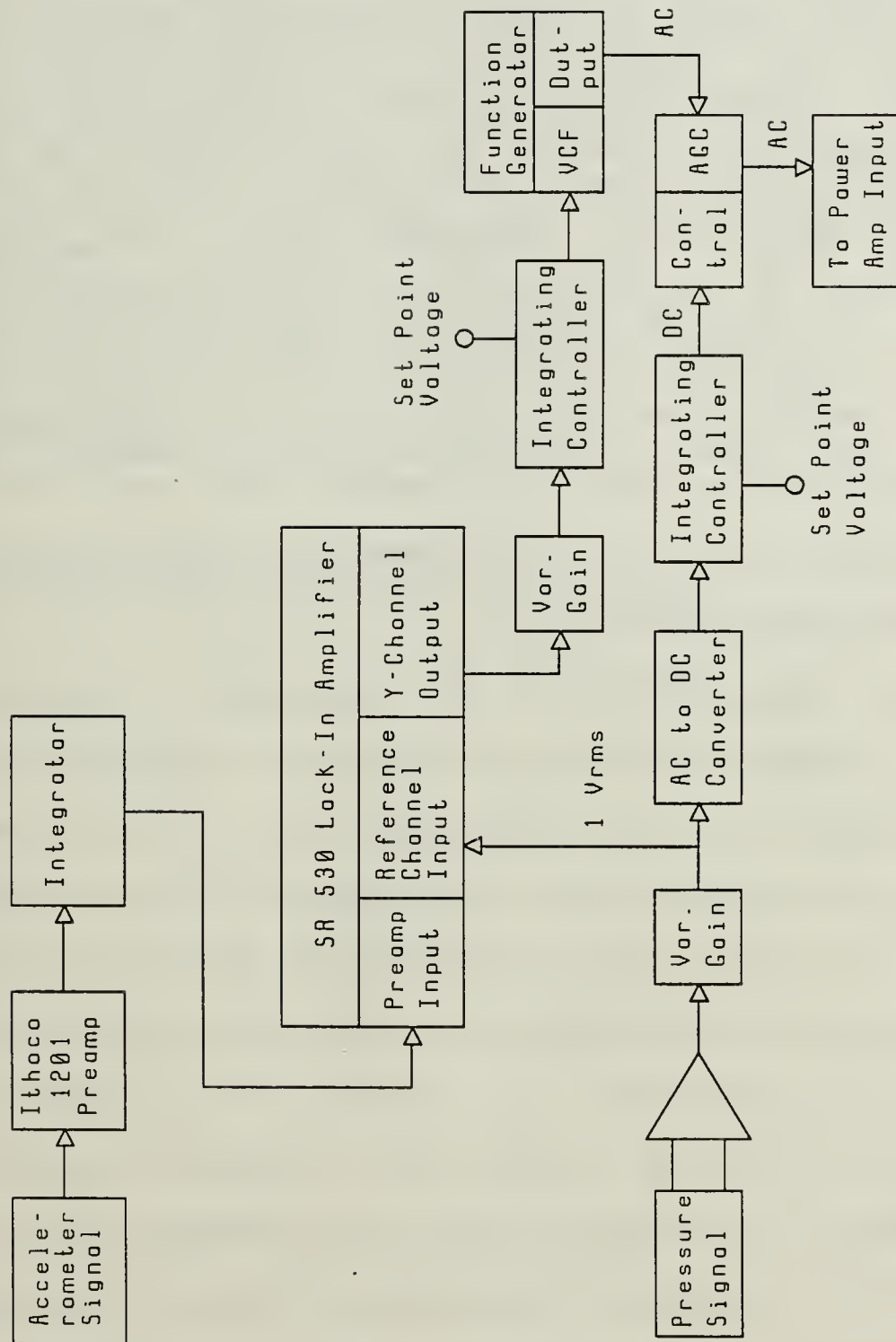


Figure IV-4. Block Diagram of the Electronics Used to Feedback Control the Frequency and Pressure Amplitude to Predetermined Values During Driver Operation

output is connected to the voltage-controlled-frequency (VCF) input of the signal generator, and the loop is closed by the driver-resonator system. The phase, including calibration corrections, is set on the lock-in so that the desired Y-channel output voltage is zero when the pressure and velocity are in phase. The controller has a set point voltage fixed at zero, so the frequency is controlled to maintain the resonance condition of the pressure and velocity being in phase. The pressure amplitude control group begins by adjusting the amplitude of the pressure signal to a pre-defined level with an adjustable gain stage. This ensures that the loop gain and stability margin are constant for different drive levels. After the pressure signal is adjusted in amplitude, it is rectified and filtered, and this DC signal is used by another integrating controller to produce a control voltage for an adjustable gain control circuit (AGC). The output of the signal generator is then passed through the AGC and into the power amplifier input. The loop is again closed by the acoustic system, with its pressure amplitude thereby being regulated.

Integrating the accelerometer signal is convenient since it is the velocity that is the important quantity in a power measurement...."

To finish the explanation we will need to discuss the velocity signal measurement since the method used by Hofler was not used in our experiment. In our experiment we measured the velocity amplitude using the lock-in directly. It was determined that this would not introduce any errors into the power measurements, as previously thought. Unlike the previous apparatus, our lock-in amplifier uses true sine wave conversion, resulting in complete rejection of the harmonic distortion in the accelerometer signal. Using the measured dynamic pressure and velocity, along with the sensitivities of the transducer and accelerometer, and the volume velocity calibration factor we can calculate an accurate acoustic power, as long as the frequency control

circuit is maintaining the phase difference between the two signals at zero.

The power protection circuit monitors the power amplifier current and will trigger a crowbar circuit to blow a fuse if either of two setpoints are exceeded. If a set peak current value is exceeded the fuse is blown, to protect against large fast transients. If a set rms current value is exceeded the fuse will also be blown, to protect against currents below the peak limit but high enough to burn out the voice coil.

C. EXPERIMENTAL PROCEDURE

In this section we will discuss three basic areas of our experimental procedure. First is the setup of the apparatus for a specific data run. Then we will cover the procedure for starting up and operating the refrigerator. We will conclude with a discussion of the actual data that is recorded. In the operating section we will cover two different methods since the procedure was changed after the second data run, for reasons that will be explained later.

Before discussing the actual setup it should be noted that all temperatures that we recorded were measured using commercial type-E thermocouple wire with an accuracy of $\pm 1.7^{\circ}\text{C}$ or $\pm 1\%$ of the reading, whichever is greater. All of the thermocouple wires are fed through a Hewlett Packard HP3421A data acquisition control unit to a computer, for

continuous display on the computer monitor during operation.

1. Setup of Apparatus

The setup of the system for a particular data run consists of filling the system with the desired gas, pressurizing the system up to the desired pressure of 10 bar and starting up the external vacuum system.

The resonator is filled through a connection at the top of the driver housing, however the controlling factor is the capillary near the driver surround that was previously discussed. The pressurization rate is monitored on a differential pressure gauge since the surround is capable of sustaining no more than 0.25 bar of differential pressure without permanent damage. The system is filled using a process of evacuation and purging that is repeated twice before the system is brought up to operating pressure. This procedure is designed to remove any gas other than the desired gas (particularly air if the system has been opened) prior to system operation. After the second evacuation the system is pressurized to 10 bar. The evacuation and purging process consumes the better part of a day due to the low flow rates that are possible within the allowed differential pressure range.

To save time, the external vacuum system can be started in parallel with the above procedure. Since the diffusion pump of the vacuum system creates a great deal of

heat, an external cooling supply is used to keep it at a reasonable temperature. Therefore, to start up the vacuum system the cooling system is lit off, the main vacuum pump suction is closed, the vacuum pump is started and the pump suction is slowly opened, to prevent rapid depressurization and damage to the previously discussed super-insulation. Then the diffusion pump is turned on. Once the system is up to pressure and the vacuum is below 1×10^{-3} torr it is ready to start up.

2. System Startup and Operation

To start the refrigerator the two controllers (frequency and pressure amplitude) are turned off and the signal generator is set up for a sine wave at the approximate resonant frequency for the resonator and gas type being used. The drive amplitude is set to zero and the power is turned on. The amplitude is brought up slowly until a drive current of about 0.5 amps is achieved. At this point the frequency is manually adjusted to resonance (i.e. zero quadrature output) and the frequency control circuit is turned on. Then the amplitude is slowly increased to the desired value (if possible) and the reference channel is adjusted to precisely 1.00 volts. Then the pressure amplitude control circuit is turned on. Depending on the desired pressure amplitude and gas type it is not always possible to reach the desired operating point at initial startup. It is therefore necessary to select

some lower amplitude, until the engine cools down and the desired amplitude can be reached. The limiting factor is generally the piston's displacement amplitude. If the maximum displacement amplitude is exceeded significant damage to the surround occurs. Once the desired amplitude is achieved the refrigerator runs unattended until steady state is reached. In this case, steady state is defined as less than a one to two percent deviation in the cold end temperature over a 90 minute period. This is determined by evaluating the continuous computer monitor display of temperatures, which shows approximately 90 minutes of data history when set up for display at four minute intervals. This is the basic procedure for startup and setup for a no (applied) heat load data point. In general equilibration takes from 8 to 24 hours depending on the pressure amplitude setting.

We have used two different methods for obtaining data with heat loads applied to the cold end. The first method is that used by Hofler (1986), where a designated heat load is applied to the heater, at the cold end, and equilibration is based on temperature stabilization, as discussed above for the no load case. This heat load is set by applying a fixed DC current and voltage to the heater coil. It was determined after two data runs that a better method might be available. This better method, designed and set up by Dr. Hofler, involves a temperature feedback

control network which allows setting a desired steady state cold end temperature. The controller then establishes the current flow to the heater that is necessary to achieve and maintain that temperature. The equilibration point is no longer based on temperature but is instead based on the heater current deviation being less than approximately $\pm 0.5\text{mA}$ over a 90 minute period. This corresponds to being within better than $\pm 1\%$ over the 90 minute period, for the currents we have measured. The control network involves a rather complex Fortran computer program, written by Dr. Hofler, that reads the heater thermocouple, at an operator selected time interval, and then performs a crude time integral of the difference between the monitored temperature and the selected set point temperature. The program's integrator output variable is used to numerically control the heater current from the HP6633A system D.C. power supply. The program allows the operator to select the control time interval (usually 5 seconds), the periodicity of display (usually 4 minutes), the desired temperature, a proportional constant in volts/deg (usually 0.0), and an integration constant in volts/deg-sec (usually 0.01). The latter two of these control the stabilization time and the degree of stabilization. The usual values that were given are those that have shown the best results during our experiments.

This temperature feedback control method was determined to be better for the STAR project for two basic reasons. First, it provided a more rapid equilibration because the refrigerator was loaded more heavily at first, to drive the temperature of the cold end to the desired temperature, and then the load was let off only as necessary to maintain that temperature. This reduced the equilibration time to 6 to 8 hours in most cases. Secondly, this method conserves power due to the reduced equilibration time. This is considered to be vital to the STAR project due to its reliance on batteries for power, which gives it a limited operating lifetime.

3. Data Recording

Once steady state has been established a data set is recorded in a notebook. A data set consists of nine readings, as well as date and time. First, the temperatures of the hot and cold heat exchangers are recorded. There are two thermocouples for each heat exchanger, one being at the center and one at the wall. Due to an intermittent failure of the thermocouple at the center of the cold heat exchanger we have only recorded the other three temperatures. Then we record the drive frequency, the mean pressure, the amplitude of the dynamic pressure signal and the amplitude of the lock-in velocity signal. Then, depending on which method of operation was used, we record the DC heater voltage and current, or just the DC heater

current. For the latter case we use the known heater resistance versus temperature characteristic to calculate the heater load (instead of voltage times current). After the data are recorded we change either the dynamic pressure amplitude or the heat load, and wait for the system to equilibrate. A standard data run for a given gas type and stack involves 8 to 10 data points and takes about a week, from start to finish. The difference in the number of data points is based on the different temperatures achievable at different pressure amplitudes, while staying within the piston's displacement amplitude limit.

In addition to the above data, we also record the vacuum in the system and the temperature and resonant frequency of a gas analysis tube, similar to that described by Polturak, et. al. (1986), and Garrett, et. al. (1986), that we attached to the system. These are monitored just for completeness and are not directly involved in any performance evaluation. With the exception of one data run, all of our gases had analysis certifications for purity, and these values were used for calculations. In one case we mixed our own helium-argon gas and used the gas analyzer, built by Dr. Hofler, to determine the mixture concentration.

The final bit of data that is recorded involves the rate at which the engine warms up, after being fully cooled down and turned off. This data is analyzed and together

with the total heat capacity of the cold end of the system, is used to determine a value for the heat leak out of the refrigerator. The heat leak determined by this method is then reduced by $2.4 \text{ mw}/^{\circ}\text{C}$, which is the portion that has been determined to be due to the thermal conductance of the stack and gas, which is internal and intrinsic to the stack. This heat leak is then included in the total heat load.

V. DATA ANALYSIS AND RESULTS

In this chapter we will discuss the methods and equations that were used in analyzing our data. This will be followed by a numerical and graphical presentation of various aspects of our experiment. It should be kept in mind that the purpose of these experiments was to improve the coefficient of performance (COP) of the prototype refrigerator, built by Hofler (1986).

A. DATA ANALYSIS

All of our data analysis was done through the use of a Microsoft Multiplan spreadsheet program and graphical display of the numbers that were thereby generated. This method was used because we had voluminous amounts of data where many of the required calculations were repetitive in nature. Taking into account all of the quantities, both recorded and calculated, we ended up with a spreadsheet of 25 columns by 122 rows. It should be noted that many of these quantities were calculated for informational purposes and are not directly related to our final evaluation of the refrigerator's coefficient of performance.

Our analysis consists of comparing a normalized (normalized to the Carnot COP for the same temperature

difference) coefficient of performance, for the refrigerator with modifications (COPR), to the same quantity for the original Hofler refrigerator. Since we have modified both the thermoacoustic stack and the gas type, we have three basic areas for comparison. We will compare the results with different stacks and the same gas type, with different gases and the same stack, and then with different stacks and gases combined. In order to make these comparisons we have created plots of COPR versus total heat load (Q_{total}). In addition to these we have created plots of temperature ratio (T_c/T_h) versus Q_{total} , to validate our data. Based on the experiments of Hofler (1986), these latter plots are expected to be linear.

In order to create these plots we need to know the values for COPR, Q_{total} , T_c and T_h . The values for T_c and T_h are simply raw data taken during the experiments. We have used the temperature at the center of the hot heat exchanger as T_h , and the temperature at the wall of the cold heat exchanger as T_c (due to the intermittent failure of the cold heat exchanger's center thermocouple).

The value for Q_{total} has two components. The first is the column labelled QHEAT in Appendix C. This is the power applied to the heater, located below the cold heat exchanger, in watts. It is calculated by either multiplying the heater DC voltage times the heater DC current, or by multiplying the heater resistance by the square of the

heater DC current ($P=VI$ or $P=I^2R$ for DC). The voltage and current values are raw data. The resistance values were taken from a plot of T_c vs. R created from the two sets of data where we recorded both heater voltage and current ($R=V/I$). This plot is shown as Figure V-1. Both of these methods were used as discussed in Chapter IV. The second component of Q_{total} is the heat leak, which is labelled HEATLK in Appendix C. As discussed in Chapter IV, this value is determined by analysis of the rate at which the refrigerator warms up once the power is turned off. Based on this warmup data and using the heat capacity of the cold portion of the resonator a value for the total heat leak to the cold end of the refrigerator is determined (in $mW/^{\circ}C$). This number is then reduced by $2.4 mW/^{\circ}C$, which is the thermal conduction of the stack and the gas. The resulting quantity is the conduction external to the stack and is accurate to within 8%. The value for Q_{total} is then the sum of $Q_{HEAT} + HEATLK$. The error in Q_{HEAT} is negligible, but the error in HEATLK is not. The error in Q_{total} is about 8% when Q_{HEAT} is zero and is about 1.5% to 2% for values of Q_{total} near heat loads of optimum efficiency.

The remaining quantity necessary for the calculation of COP is the acoustic power (or work). We use a relation similar to that derived by Hofler (1986). The difference being that we no longer use the velocity signal from the bandpass filter; using the velocity signal from the lock-in

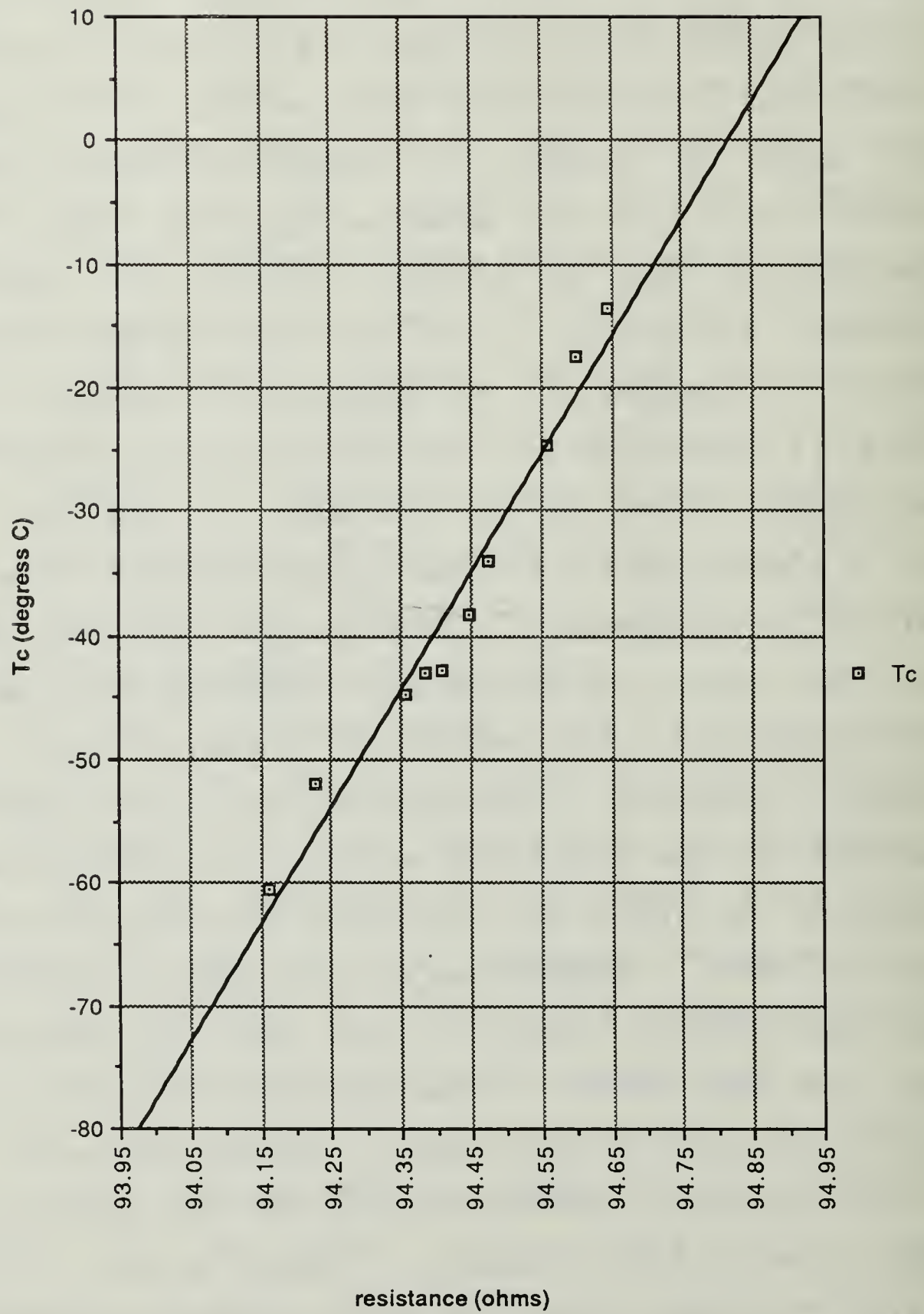


Figure V-1. Temperature vs. Resistance

instead. Also, we have added two correction terms to the equation. We are using an equation of the form:

$$W = \frac{(1/M_P)^2 V_P V_{LI} (1 - \epsilon_A)}{(M_P/M_U) - \epsilon_{VV}}$$

where M_P is the dynamic pressure transducer sensitivity, M_U is the volume velocity sensitivity, V_P is the measured pressure signal, V_{LI} is the measured velocity signal, $(1 - \epsilon_A)$ is an accelerometer non-linearity correction term, and ϵ_{VV} is a volume velocity calibration correction term. $\epsilon_A = (7.4 \times 10^{-5} \text{ sec}^2/\text{cm})a$, where a is the acceleration in cm/sec^2 ($\times 10^{-3}$), as shown in column 13 of Appendix C. $\epsilon_{VV} = 0.05(f - 550)$, where f is the frequency in hertz, as shown in column 4 of Appendix C. The ratio M_U/M_P is the result of the small cavity volume velocity calibration, discussed previously, and is therefore just a number that we put into the equation prior to calculation. Since the refrigerator was disassembled on several occasions during our experiments this calibration was performed several times. The calibration value changes over time as the driver is used and therefore this number M_U/M_P is corrected in our equations for all data taken after each calibration. The quantity M_P is also a calculated number that is input into the equations, since it is just the dynamic pressure transducer sensitivity. The actual equations that we have used are of the following form:

$$W = 59810(1 - 7.4 \times 10^{-5}a)V_P(0.003V_{LI})/(1839.8 - 0.05(f - 550)),$$

where 59810 is $(1/M_P)^2$ including unit conversions, $(1-7.4 \times 10^{-5} a)$ is a correction term for accelerometer nonlinearities, as discussed above, $(0.003 V_{LI})$ is the measured velocity signal (with unit conversions in the coefficient), 1839.8 is (M_U/M_P) the result of our volume velocity calibration, and $(0.05(f-550))$ is a correction to the volume velocity term due to the calibration being frequency dependent, as discussed above. The accelerometer correction $(1-\epsilon_A)$ is about 2% at most, and the frequency correction (ϵ_{VV}) is about 1% at most. The frequency correction was obtained for the case of pure helium. However, given the much larger frequency range of the gas mixtures, the amount of correction in some cases is too small, giving a calibration error of about 1%. The total worst case error for W is about 5% with 3.5% being a more typical value.

Using the Q_{total} and W values calculated by the above methods we get $COP = Q_{total}/W$. To get $COPR$ we need to divide this by the Carnot COP for the same temperature difference. The Carnot COP is known to be $COP_{carnot} = T_c/(T_h - T_c)$, which means $COPR$ can be derived as $COPR = COP((T_h/T_c) - 1)$. This is the equation we have used to determine $COPR$. On our spreadsheet, in Appendix C this is the $COPR2$ column. The worst case error in the absolute values for $COPR$ may be as high as 15% however, typical values are about 5%. Also, the relative error involved in comparing data taken under different conditions is probably considerably less than 5%.

We now have all of the values necessary to evaluate the effects of our modifications on the refrigerator's coefficient of performance.

B. RESULTS OF EXPERIMENT

As stated earlier, we will break this discussion into three major sections. First we will discuss the results of our stack modifications. This will be followed by a discussion of performance with different gases and the same stack. We will conclude with the overall improvements using our best stack/gas combination. Also, a brief discussion concerning the results with different pressure amplitudes and different resonator lengths will be provided.

Since we have data from two new stacks and two gas mixtures, as well as two different pressure amplitudes and two resonator lengths, available for comparisons, we must be selective in our presentation, so as not to have an excessive number of plots that show the same result. To fulfill this goal we will present one or two sample sets of curves, with analysis, for each major category of interest, and provide numerical results for the other cases within that category, where appropriate. In general a set of curves includes a plot of COPR versus Q_{total} and a plot of T_c/T_h versus Q_{total} .

Prior to presenting any of our figures we shall introduce the notation that is used in the titles and legends.

All of our plots are designed to provide data comparisons and as such each contains more than one curve. The legend lists the specific curves using the following notation:

GAS TYPE--STACK--RESONATOR LENGTH--PRESSURE AMPLITUDE, where abbreviations have been used in all cases. For gas types we have helium, helium-argon, and helium-xenon which are represented by He, HeAr, and HeXe, respectively. For the stacks we have old, new, and dual which are represented by O, N, and D, respectively. The resonator length is designated by s or l for short or long and the pressure amplitude is represented by the percent, relative to the mean pressure (P_o/P_m), by the number 2 or 3.

1. Stack modification results

To illustrate the effects of our stack modifications we have elected to compare the data for pure helium, at 2% pressure amplitude, with the short resonator installed. Figure V-2 shows the temperature ratio (T_c/T_h) versus total heat load (Q_{total}) curves for all three stacks under these conditions. It is fairly clear from the curves that the data are essentially linear for all three cases, as expected. The curves also show that for a given temperature ratio the old stack can support more heat load than the dual stack and the new stack can support more heat load than either of the others. This statement can be reversed, such that for a given heat load the temperature spanned is greatest for the new stack and lowest of the dual stack.

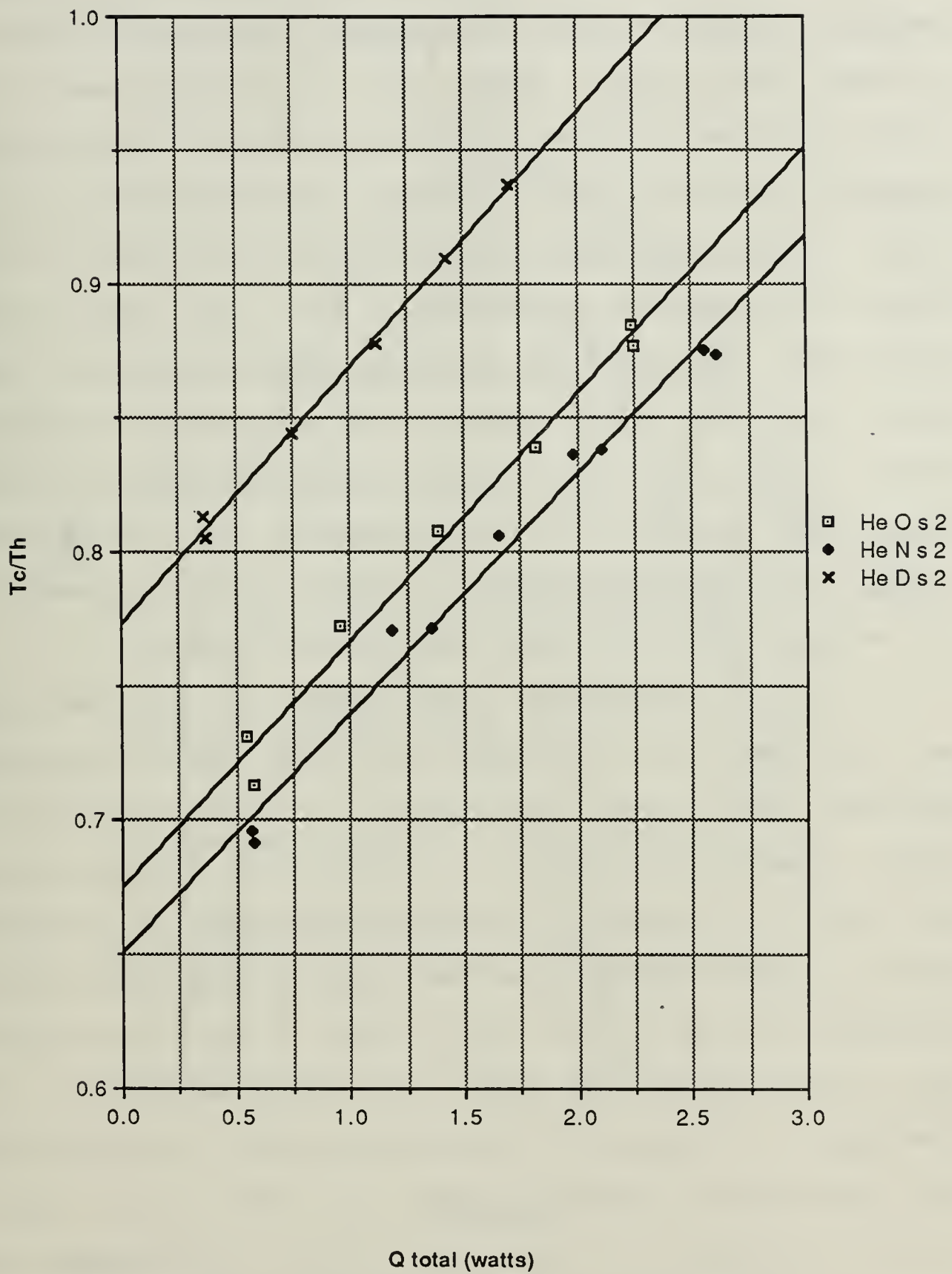


Figure V-2. Temperature Ratio vs. Q_{total} , For Helium, Short Resonator

These curves also show that our data are following the expected trends for the refrigerator, in general. Figure V-3 shows COPR versus Q_{total} for all three stacks. It is clear from this Figure that the COP is significantly improved with the new stack and vastly degraded with the dual stack. Evaluating the difference at the peaks of the curves, we see that the dual stack has a peak COPR of 0.034 while the old stack has a peak at 0.067 and the new stack peaks at 0.078. This shows a 16% improvement for the new stack and a 51% reduction for the dual stack. Conducting this same analysis for the remainder of our data sets yields an average improvement of 14% with the new stack and an average reduction of 57% with the dual stack.

It is clear from these results that the dual stack has not performed as predicted while the new stack has provided significant improvements. It is believed that the basic theory used to design the dual stack is valid, in-so-far as the concept is concerned. However, it is obvious that we have underdesigned the stack by either omitting an important factor or over simplifying. At the time of design and construction of the stack, it was our belief that plate spacing, so long as it was not too small, would not have any detrimental effects. Based on this belief, and an initial evaluation of the new stack's performance, we decided to build the dual stack with the hot end having the same fishing line size as that used in the new stack.

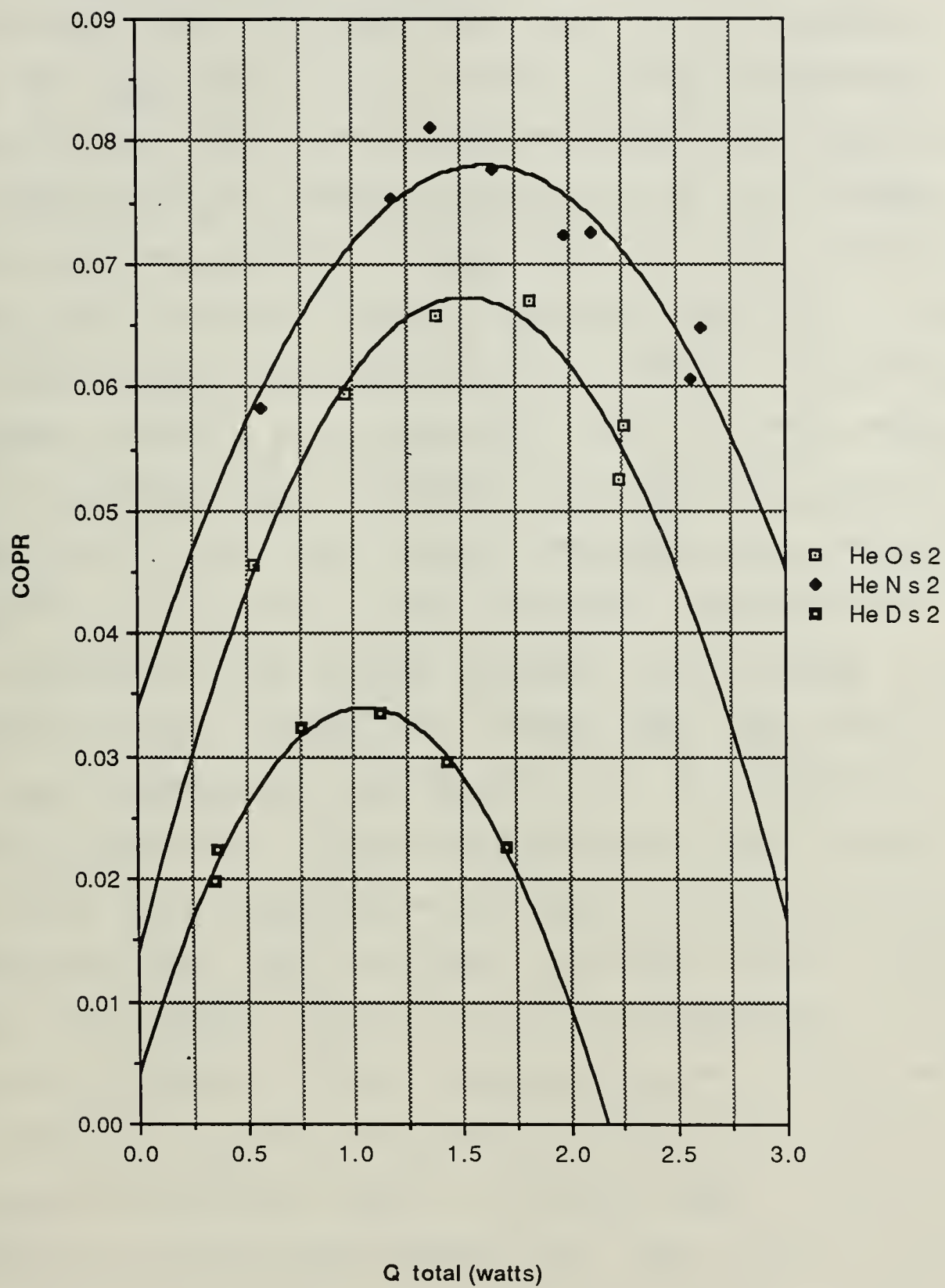


Figure V-3. COPR vs. Qtotal for Helium, Short Resonator

However, with the dual layer at the hot end and the thick fishing line at the cold end, we ended up with a 20% increase in plate spacing at the hot end and a 163% increase in plate spacing at the cold end (relative to the spacing in the new stack). Based on the extremely poor results with the dual stack it appears that the magnitude of the plate spacing is more critical than we had originally thought. The theory, presented in Chapter II, shows that a plate spacing of 2 to 4 thermal penetration depths, with the entire resonator cross-section filled with plates is desired for the best heat pumping characteristics. However, our analysis of the theory did not predict this massive drop in COP with a larger plate spacing. To some extent this plate spacing effect is illustrated by the new stack's performance, as well. Although our intuitive reasoning for the design of the new stack predicted improved performance, the results are better than expected. Combining this with the extremely poor performance of the dual stack, and the fact that the new stack has the smallest plate spacing of the three stacks, we can see that plate spacing is much more important than previously thought. Rough calculations for helium show that the average plate spacing, in number of thermal penetration depths is 3.3 for the new stack, 3.5 for the old stack, 4.0 for the hot end of the dual stack, and 8.8 for the cold end of the dual stack.

2. Results for Gas Mixtures

For this analysis we have elected to present two sets of data, both of which are for the new stack. This is primarily due to the fact that the new stack is the only one for which we have any helium-argon data. Also, based on the stack analysis, the new stack is the best one available. For this analysis we will discuss the results for 2% pressure amplitude and both the short and long resonator. The long resonator consists of a one inch spacer that lengthens the resonator and thereby changes the position of the stack relative to the acoustic standing wave.

Figures V-4 and V-5 show the plots of T_c/T_h versus Q_{total} for the short and long resonators, respectively. It is clear from these curves that all of the data are linear, as expected. It is interesting to note that in Figure V-2 all of the curves for pure helium were essentially parallel, even though the data was for different stacks. Now, in Figures V-4 and V-5 we see that the curves are no longer parallel for the different gases, even though the data are all for the same stack. This is believed to be related to the fact that the heat pumping capacity is related to the PU product (pressure times volume velocity). For helium gas at constant pressure amplitude the PU product will vary in a consistent manner, with respect to temperature, regardless of stack design. For different

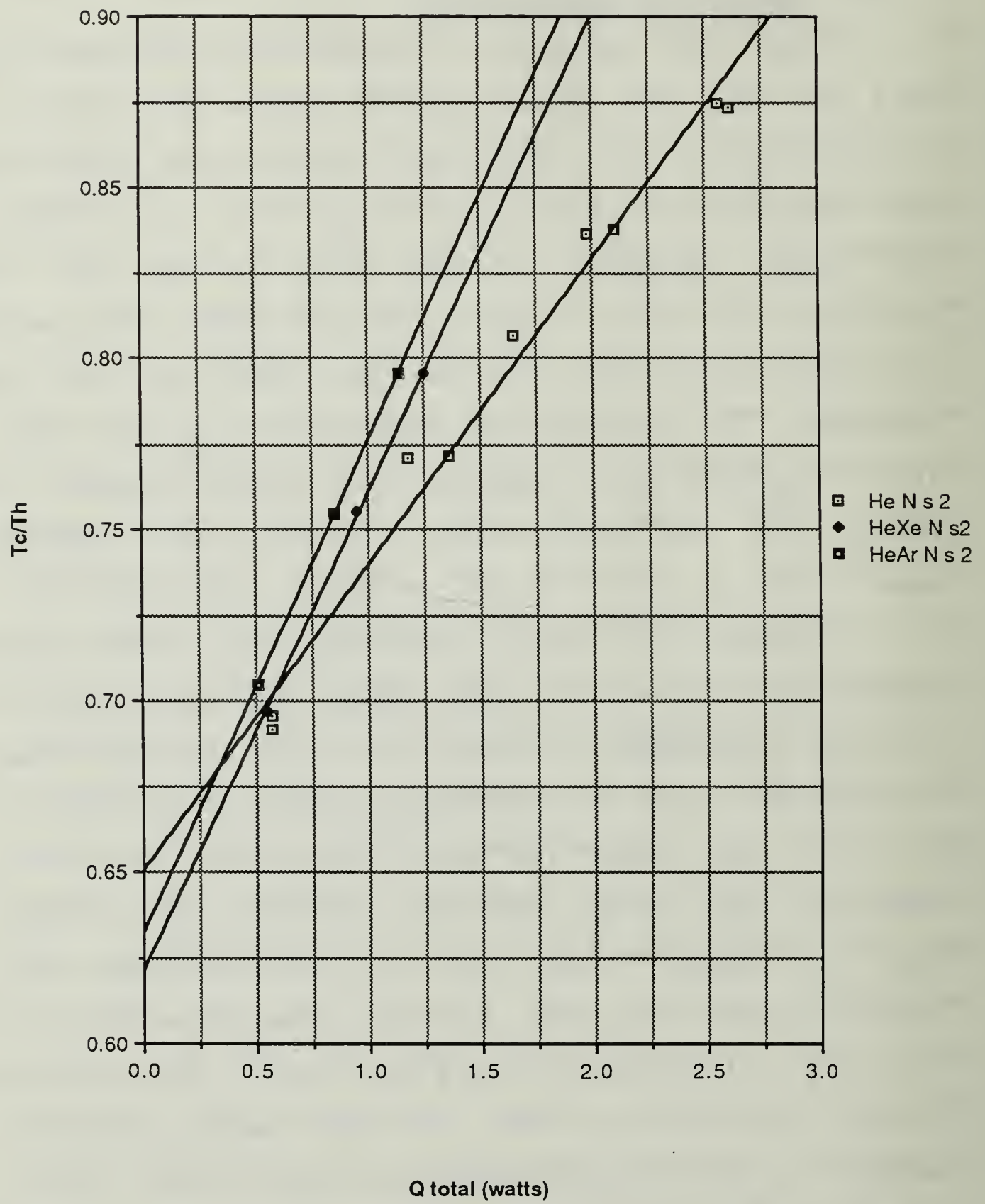


Figure V-4. Temperature Ratio vs. Q_{total} , New Stack, Short Resonator, All Gases

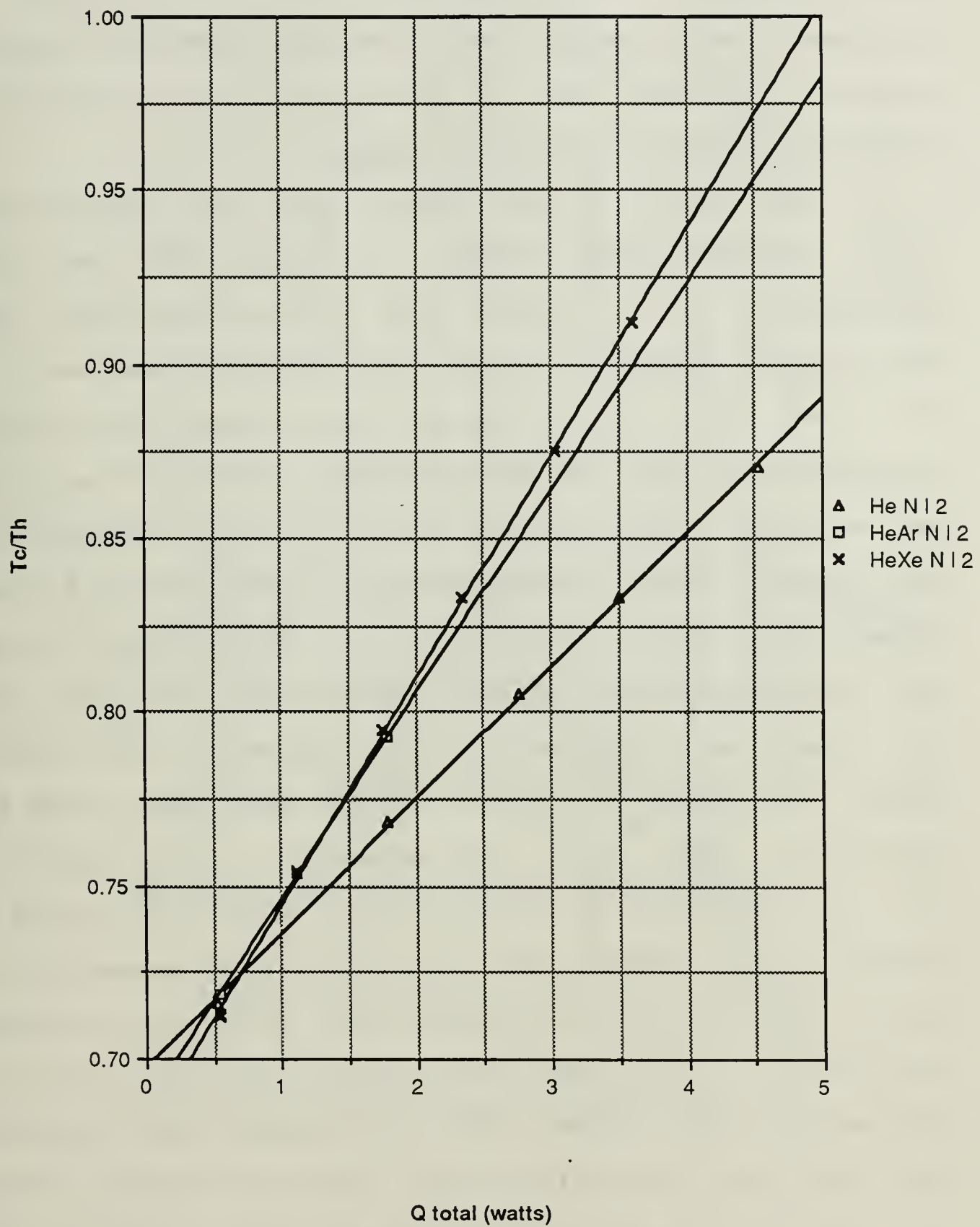


Figure V-5. Temperature Ratio vs. Q_{total} , New Stack, Long Resonator, All Gases

gases however, the velocities will vary because of different sound speeds, and therefore even at constant pressure amplitude the PU product will vary differently, producing curves with different slopes.

The plots of COPR versus Q_{total} for the short and long resonator are shown in Figures V-6 and V-7, respectively. It is clear from all of these curves that helium-argon produces a certain degree of improvement in COP, over pure helium, and that helium-xenon produces the highest COPR. For the short resonator curves of Figure V-6 we see that the peak COPR values are approximately 0.078 for helium, 0.102 for helium-argon, and 0.129 for helium-xenon. From these values we see that helium-argon gives a 31% increase over helium, while helium-xenon provides a 65% improvement over helium and a 27% improvement over helium-argon. It should be noted that the peak COPR values are shifted to lower heat load values for the gas mixtures. This is believed to be due to a reduction in this PU product that was discussed above. Similar calculations for other stacks and other pressure amplitudes show an average improvement in the peak COPR values of 61%, when comparing helium-xenon to helium. There is no other short resonator data available for helium-argon. The long resonator curves of Figure V-7 have been included primarily because they illustrate the peak COPR value that has been measured to date of 0.197 for helium-xenon. Although the helium-argon

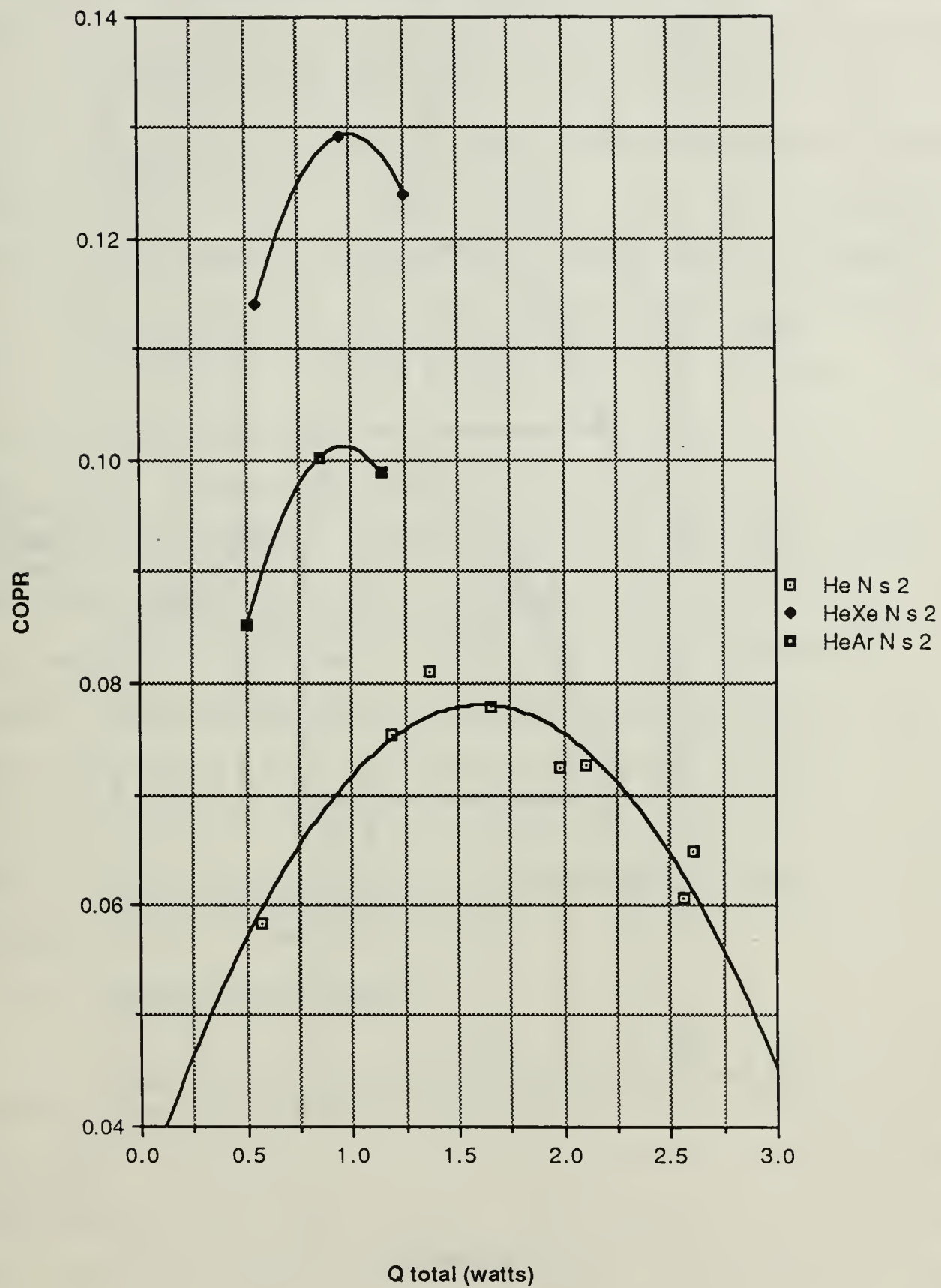


Figure V-6. COPR vs. Qtotal, New Stack, Short Resonator, All Gases

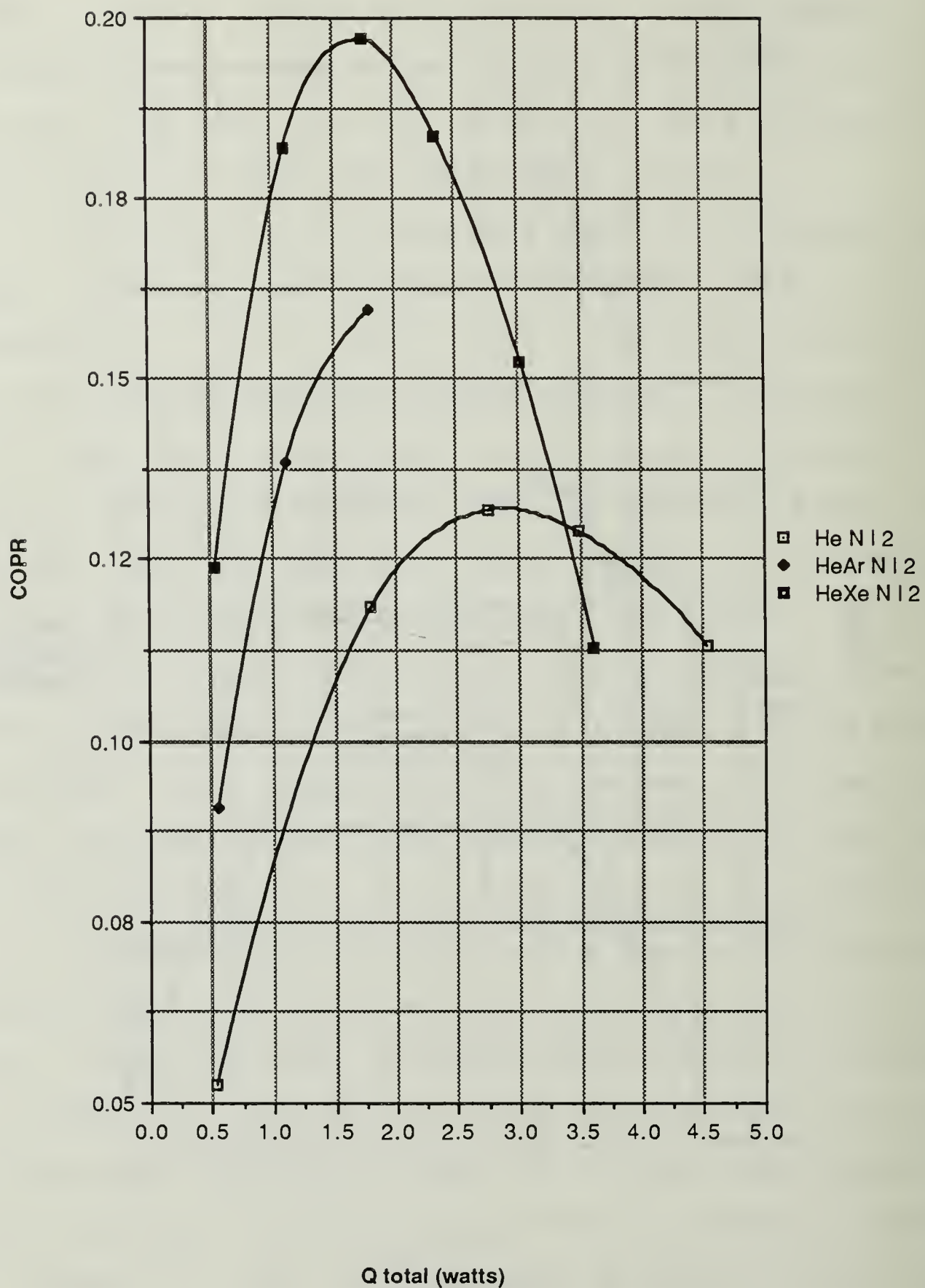


Figure V-7. COPR vs. Qtotal, New Stack, Long Resonator, All Gases

curve appears somewhat incomplete we feel safe in assuming, based on all of our other curves and data, that the curve is within a few percentage points of its peak value at the last plotted data point. We will therefore use that datum for our peak value. These curves show the same general trends as those of Figure V-6, however the magnitudes of the improvements are somewhat reduced. For peak values of 0.132 for helium, 0.1595 (from data of Appendix C) for helium-argon and 0.197 for helium-xenon, we see that helium-argon only produces a 21% improvement over helium and helium-xenon produces a 49% improvement over helium with a 24% improvement over helium-argon. It is believed that the improvement percentages with the long resonator are reduced because the long resonator itself produces about a 62% improvement over the short resonator, thereby placing the refrigerator closer to a maximum possible or limiting COPR value. Thus the absolute improvements we achieved have a smaller effect, percentage wise.

3. Overall Improvement

In this section we present the overall result of the thesis. That is, the overall improvement in the COP of the prototype refrigerator, taking into account both the stack modifications and the binary gas mixtures. To illustrate this case we have elected to compare the results with the old stack and pure helium at 2% pressure amplitude to those achieved with the new stack and helium-xenon at 2% pressure

amplitude. These sets of data were selected because the original refrigerator used only the old stack and pure helium, while our best results were achieved with the new stack and helium-xenon. We have not used the long resonator data, even though that gives our highest COPR, because we did not take any long resonator data with the old stack. However, for a number for the old stack, long resonator, pure helium setup we can use the 0.126 peak COPR given by Hofler(1986) in his doctoral dissertation. Comparing this to our best case peak COPR of 0.197 we get a 56% improvement.

For the comparison of our experimental data we will present the COPR versus Q_{total} plot only, since the T_c/T_h versus Q_{total} plots have already been discussed for this data. Figure V-8 shows our plot for overall improvement. With peak COPR values of 0.129 for the helium-xenon and 0.067 for the helium we see that the overall improvement in the refrigerator's coefficient of performance, due to our modifications, is 93%.

4. Other Effects of Interest

There are two other areas of interest that have been mentioned briefly during our discussions of results. These are the effects produced by changing resonator length and those produced by changing the pressure amplitude.

In Figure V-9 we present the data for all three gases in the new stack with both short and long resonators.

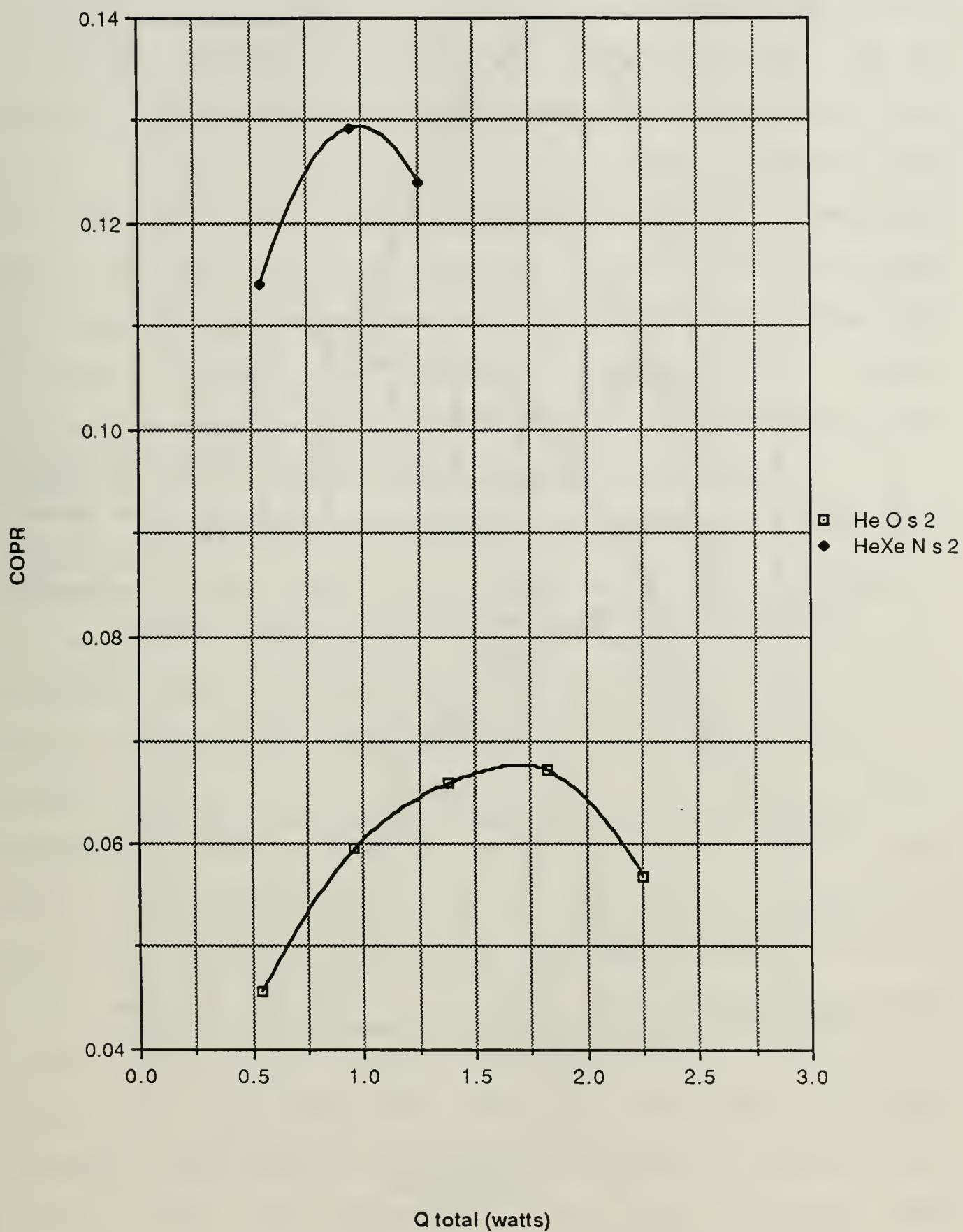


Figure V-8. COPR vs. Qtotal, Showing Overall Performance Improvement

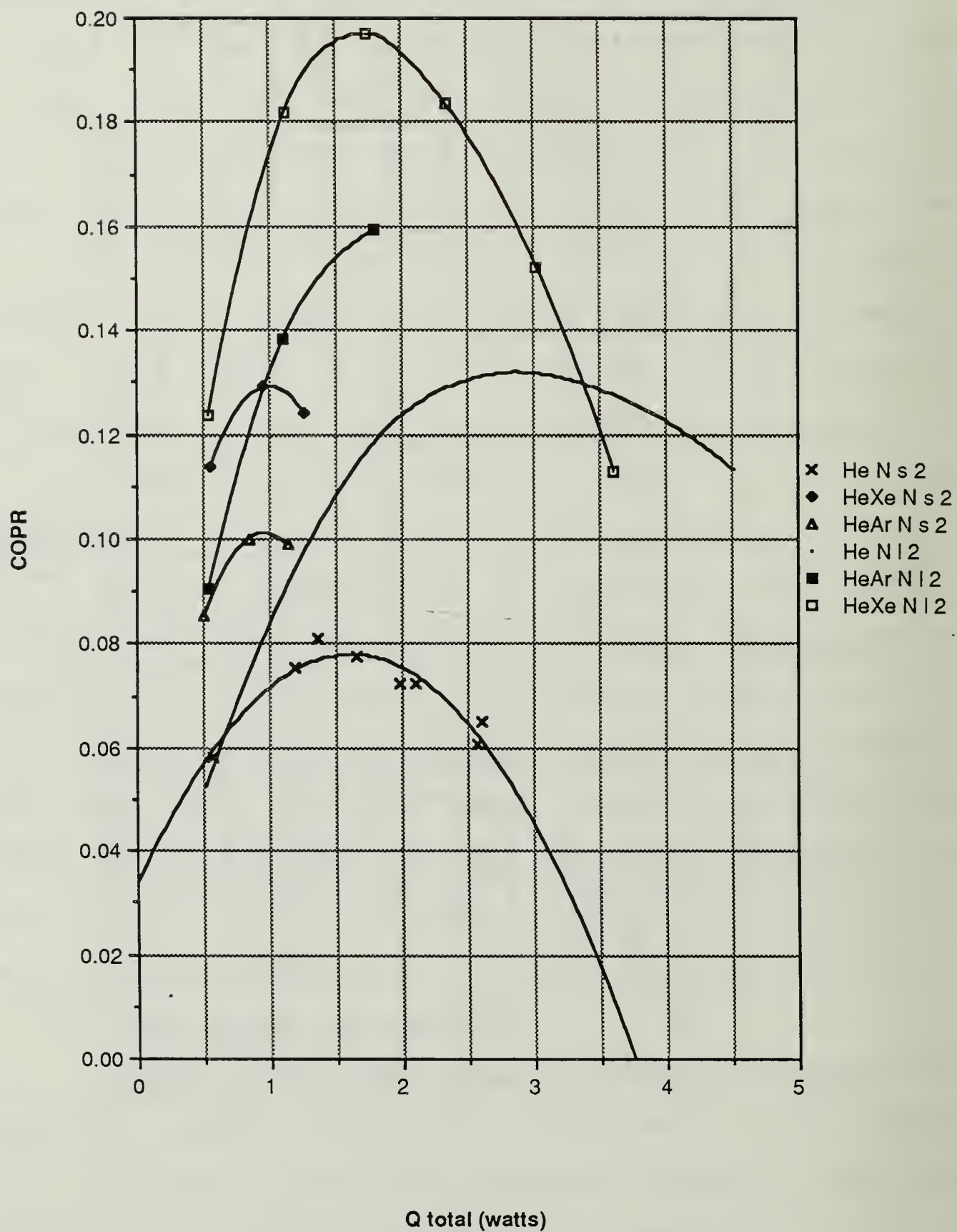


Figure V-9. COPR vs. Qtotal, Showing Resonator Effects

From this we can see that just the shift from short to long resonator produces increases in COPR as follows: 70% for helium, 59% for helium-argon and 52% for helium-xenon. This rather large increase in COP is due primarily to the shift in the position of the stack relative to the standing wave. With the long resonator installed, the hot end of the stack is moved closer to the velocity antinode and the heat transfer power is increased significantly, thereby producing the large increase in the COP and the observed shift of the COPR peak towards higher heat loads.

In Figures V-10 and V-11 we present a comparison between both gas types and pressure amplitudes. In Figure V-10 we have helium-xenon with the short resonator, both pressure amplitudes and all three stacks. In Figure V-11 we have all of the same curves for pure helium. In all of these curves it is obvious that at higher pressure amplitudes the peak COPR value has shifted toward higher heat loads. Based on this and the discussion of Figures V-4 and V-5 it is clearly shown that heat transfer power (or heat pumping capacity) increases with pressure amplitude (due to the PU product increasing). It is interesting to note that the peak COPR value is in fact lower, at higher pressure amplitudes, for all of the cases for which we have data, with the exception of the pure helium, short resonator, old stack case. In his doctoral dissertation, Hofler reported that the peak COPR value increased with

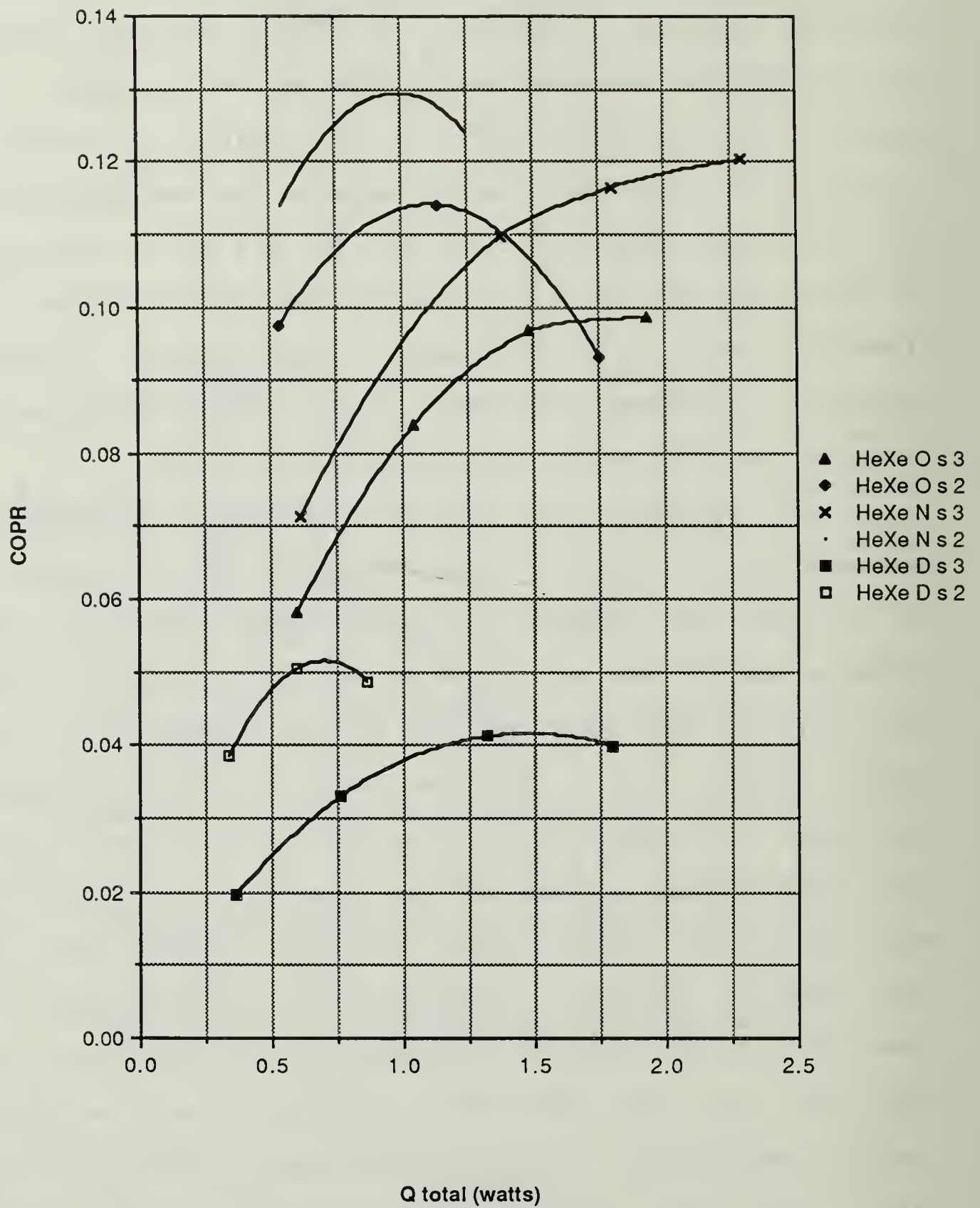


Figure V-10. COPR vs. Qtotal for HeXe, Short Resonator, All Stacks and Amplitudes

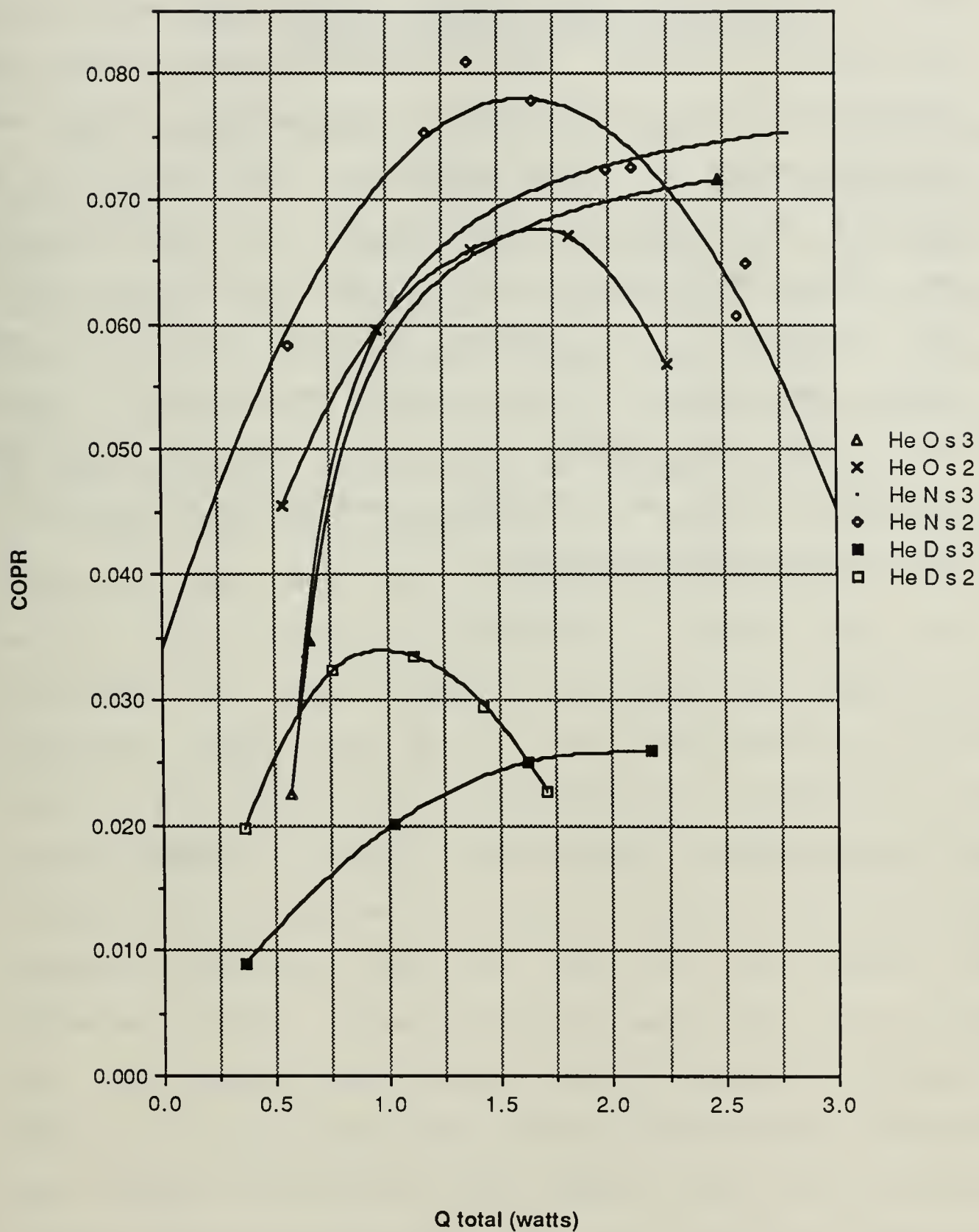


Figure V-11. COPR vs. Qtotal for He, Short Resonator, All Stacks and Amplitudes

pressure amplitude for all of his data. In fact our data with his stack and helium also follow this trend. Additionally, Hofler (1986) reported: "there is also some indication that the magnitude of these maxima approach some constant value at higher amplitudes." Our results for gas mixtures and other stack designs tend to contradict this, and lead toward a rather alarming conclusion that there is some relatively low pressure amplitude at which the COPR maxima peak and above which the COPR maxima drop off again. This seems to indicate that there may be some non-linearity, such as turbulence, that limits the best COP's to relatively low amplitudes.

VI. CONCLUSIONS AND RECOMMENDATIONS

The primary purpose of this thesis is to provide modifications for the Space Thermoacoustic Refrigerator (STAR) that will improve its thermodynamic efficiency, specifically its coefficient of performance (COP). Through the use of a helium-xenon binary gas mixture and a new stack design, with less string and reduced plate spacing, we have produced a 93% increase in the peak value of COP.

Along with this improvement we have raised several questions that are as yet unanswered. Based on our results with a long resonator, relative to those with a short resonator, it would appear that there is some optimum resonator length and design that must be found. Further testing with different resonator spacer thicknesses, must be performed to resolve this issue. The unexplained drop in peak COP relative to Carnot (COPR), with increasing pressure amplitude opens the door for more testing with different setups and many pressure amplitudes. It is clear that the binary gas mixture of helium-xenon is superior under all of the conditions that we have observed. However, the failure of the dual stack and the better than expected results with the new stack leave the final stack design as an open item. It is clear that another dual stack and a different version of the new stack should both be built,

with smaller plate spacings, to determine the optimum stack design. It is the answers to these question that will yield the design capable of producing the maximum thermodynamic efficiency for the Space Thermoacoustic Refrigerator (STAR).

Although this project deals specifically with the space application of our refrigerator, there is no reason that it should be limited to that application. Due to the lack of moving parts that are present in most other cooling engines (i.e. sliding seals) this unit should be extremely reliable. It also has reasonable efficiency relative to most commercial refrigeration devices. The fact that it does not use chloroflourocarbons is a great advantage, especially with the close scrutiny that this ozone destroying substance is currently receiving. Therefore, this type of refrigeration device could, and should be developed for commercial use and should be considered as a possible candidate for virtually any type of cooling need.

APPENDIX A. PRANDTL NUMBER PROGRAM

This appendix provides a program and documentation for the calculation of Prandtl numbers for binary gas mixtures. The program, written by the author, is designed to calculate Prandtl numbers for all concentrations of a binary mixture of Helium and one other gas. The program is written in Fortran for use on the Naval Postgraduate school mainframe computer, with a Watfor-77 compiler. Two output files are created when the program is run. The first, called "PRANTL OUTPUT A1", is a listing of Prandtl numbers versus helium fraction for further use in a plotting program, to create Prandtl number versus helium fraction curves for the gas mixture selected. The second, called "PRANTL RESULTS A1" is a tabular listing of Prandtl number, thermal conductivity (in cal/cm-sec-K), and dynamic viscosity (in gm/cm-sec) versus helium fraction for the selected gas mixture. The listings go from pure helium to zero percent helium in one percent intervals to provide easy access to any specific mixture. All of the theory and equations necessary to create the program, other than knowledge of a programming language, can be found in "MOLECULAR THEORY of GASES and LIQUIDS" by Hirschfelder, Curtiss, and Bird, John Wiley & Sons, Inc., New York, 1954. The primary source was chapter eight of the text, hereafter

referred to as Hirschfelder, although section and equation numbers will be specified where necessary for clarification.

As written, this program was designed for personal use, exclusively to derive the data necessary to create the previously mentioned curves of Prandtl number versus helium fraction. It has been modified to include the second tabular output for completeness and further use by others in this field. The program is currently written to require hard input and therefore requires editing of the main program for each change of gas type or temperature. In addition to satisfying the specified needs, this method was used due to there being thirteen input parameters that vary with gas type and temperature, five of which require table lookups in Hirschfelder. This program could be modified for incorporation into a larger program as a subroutine, provided the specific gas types and temperatures of interest are completely specified and all of the input parameters are looked up and incorporated into a data array for reading. This has not been done to date as the current useage did not require these features.

As previously stated the primary source for this program is chapter eight of Hirschfelder, which provides the equations necessary to calculate various transport coefficients, such as the coefficient of viscosity and the coefficient of thermal conductivity. The equations

presented in chapter eight rely heavily on the elementary theory of transport phenomena presented in section 1.2 of the text as well as the rigorous kinetic theory for monatomic gases presented in chapter seven. The intricate details of this theory will not be presented here, however a discussion of the methods used, including the main assumptions and restrictions, will be provided as well as a definition of each of the terms or symbols in the program.

The development of the kinetic theory for gases is based on knowledge of the distribution function that represents the number of molecules of a specific species, in a unit volume element about a point in space, with velocities in a unit range about a specified velocity, at a given instant in time. Since the usual definitions for transport coefficients only apply under conditions of equilibrium (or only slightly different from equilibrium) this restriction applies to the results. Under this limit the distribution function is nearly Maxwellian and is solvable by a perturbation method developed by Chapman and Enskog. The solutions are then used to obtain expressions for transport coefficients in terms of a set of integrals, $\Omega(l,s)$, which involve explicitly the dynamics of molecular encounters. The Chapman-Enskog theory relies on several assumptions and therefore has limited applicability. Each assumption will be briefly discussed and related to the specific situation of our experiment.

Only binary collisions are considered, which limits us to densities low enough that three body collisions are unimportant. The theory predicts that viscosity is independent of pressure at constant temperature. Experiments on Nitrogen have shown that only a 4% deviation in viscosity occurs as pressure is varied from 1 to 60 atmospheres. Our operating condition of 10 atmospheres is well within this and should therefore closely follow the theory in this respect.

The theory further limits itself to Classical Mechanics and thereby precludes low temperature situations where quantum effects become significant. These quantum effects are less than 1% for helium above 200 Kelvin (and even smaller for heavier isotopes). The coldest temperature we have achieved to date has been 193 Kelvin under a no load condition so our normal operations are all above 200 Kelvin and we are not concerned with quantum effects.

The Chapman-Enskog theory uses a series approximation, to the above mentioned distribution function, in solving the Boltzmann equation and then uses only the first approximation, which is only valid when the gradients of the physical quantities (i.e. density, velocity, temperature) are small. The changes of these properties over one mean free path must be small with respect to unity. Based on the mean free paths for gases at pressures above one atmosphere this condition is satisfied except

under conditions of extreme gradients such as those present in shock waves. Since we do not have any shock waves we are not restricted by this.

The theory further assumes that the dimensions of the containing vessel and any obstacles within it are large compared to the mean free path, which provides no limitations for our gases and our pressures. Although the Chapman-Enskog theory applies strictly to monatomic gases the results have been shown to be good, even for polyatomic gases, provided that the molecules are not too non-spherical. Finally, the development of the theory results in the set of integrals $\Omega(l,s)$, which are present in all of the equations for transport coefficients. These integrals, in turn are dependent upon the potential function that represents the molecular interactions. Throughout the derivation in Hirschfelder, and for all of the equations used here, the Lennard-Jones (6-12) potential is assumed.

Since some of the other terms and symbols depend upon the Ω terms in the program, we will start with a discussion of where the Ω terms come from. These $\Omega(l,s)$ terms represent a set of integrals, linear combinations of which are used to evaluate the more complex bracket integrals arrived at in solving for the expansion coefficients of the Sonine polynomials. The transport coefficients are expressed in terms of the Sonine

polynomial expansion coefficients and can then be expressed in terms of these $\Omega(l,s)$ integrals. In Hirschfelder there is also an $\Omega\text{-star}(l,s)$ symbol which represents the deviation of a particular molecular model (in our case the Lennard-Jones (6-12) potential) from the idealized rigid sphere model of molecular interactions. All of the Ω s in the program represent an $\Omega\text{-star}$ value. The Ω integrals are functions of the reduced temperature ($T^*=kT/\epsilon$) and are tabulated in table I-M of Hirschfelder.

Where more than one variable of a given type exists, such as σ_1 , σ_2 , and σ_{12} , the 1 and 2 represent the value of the quantity for pure gas 1 or pure gas 2 (which is always helium for our purposes), respectively. The 12 represents the value for gases 1 and 2 together. This is true for all cases except ϵ_{12} and λ_{12} . These two variables represent artificial quantities for a hypothetical pure substance with molecules of molecular weight $2(M_1)(M_2)/(M_1+M_2)$ that interact according to a potential curve specified by interaction parameters σ_{12} and ϵ_{12} . These parameters are defined in terms of the Lennard-Jones (6-12) potential in chapter one of Hirschfelder, where σ is the distance of closest approach (in angstroms) of two molecules which collide with zero initial relative kinetic energy and ϵ is the maximum energy of attraction of the two molecules. Table I-A of Hirschfelder provides values for σ and ϵ/k for various

substances, where k is the Boltzmann constant and ϵ/k has units of Kelvin. The parameters ϵ_{12} and σ_{12} are arrived at through empirical combining laws which relate force constants between unlike molecules to those between like molecules. These laws are $\sigma_{12} = (1/2)(\sigma_1 + \sigma_2)$ and $\epsilon_{12} = (\epsilon_1 \epsilon_2)^{1/2}$. The quantities A_{12} and B_{12} are merely frequently encountered ratios of different Ω 's that have been tabulated separately as functions of T^* in table I-N of Hirschfelder.

The remaining terms or symbols in the program are fairly straightforward, based on the above explanations and each type will now be defined:

PR=prandtl number

HE=helium fraction

LAM=thermal conductivity coefficient (in cal/cm-sec-K)

ETA=coefficient of dynamic viscosity (in gm/cm-sec)

M=molecular weight

CP=specific heat capacity at constant pressure
(in cal/gm-K)

T=absolute temperature (in Kelvin)

X1=fraction of non-helium gas

X2=helium fraction

I=counting variable for the Do loop

The output parameters are Prandtl number, helium fraction, thermal conductivity, and dynamic viscosity. They are represented by PR(I), HE(I), LAMIX(I), and ETAMIX(I)

respectively. The remaining parameters are all merely mathematically defined intermediate steps in the calculations of the output parameters and have no physical meaning. The terms used for viscosity are XETA, YETA, and ZETA, and the terms used for thermal conductivity are U1, U2, UY, UZ, XLAM, YLAM, and ZLAM.

This section will now provide the most recent version of the program. Since the explanation of the input is fairly lengthy it will be covered first, rather than disrupt the flow of the program. This will include a list of all required input parameters, their sources where appropriate, and a sample set of inputs that were used. There are thirteen input quantities, A12, B12, OMEG12, M1, M2, CP1, CP2, SIGMA1, SIGMA2, SIGM12, OMEGA1, OMEGA2, AND T. After selecting M1, M2, and T you have specified your gas combination and temperature of interest. Values for CP may be obtained from various sources, such as the CRC tables, thermodynamics textbooks, or standard tables of thermodynamic properties. The values for SIGMA as well as ϵ/k are obtained from table I-A of Hirschfelder. Using ϵ/k for each gas and $\epsilon_{12} = ((\epsilon_1 \epsilon_2)^{\frac{1}{2}})$ you calculate $T1^*$, $T2^*$, and $T12^*$ (where $T^* = kT/\epsilon$). Now using the appropriate T^* you go to table I-M of Hirschfelder for the OMEGA values and table I-N for A12 and B12. This provides a complete set of input quantities. The following table is a sample set of inputs for two gas combinations at two different temperatures:

<u>GAS COMBINATION AND TEMPERATURE</u>				
QUANTITY	He-Xe	He-Xe	He-Ar	He-Ar
<u>OF INTEREST</u>	200	300	200	300
M1	131.3	131.3	39.948	39.948
M2	4.0026	4.0026	4.0026	4.0026
SIGMA1	4.055	4.055	3.418	3.418
SIGMA2	2.556	2.556	2.556	2.556
(ϵ/K)1	229	229	124	124
(ϵ/K)2	10.22	10.22	10.22	10.22
OMEGA1	1.700	1.394	1.275	1.104
OMEGA2	0.7467	0.7485	0.7467	0.7485
CP1	0.0382	0.0382	0.12477	0.12477
CP2	1.2512	1.2512	1.2512	1.2512
(ϵ/K)12	48.38	48.38	35.60	35.60
T12*	4.134	6.201	5.618	8.427
A12	1.098	1.1034	1.102	1.108
B12	1.093	1.0904	1.091	1.0905
OMEG12	0.9632	0.8916	0.9080	0.8470

PROGRAM PRANTL

C

C

C First the array variables are dimensioned to allow

```

C   calculating and plotting the desired quantities. Then
C   the real quantities are defined since some begin with
C   letters that would make them integers by default.
C
C
      DIMENSION PR(150),HE(150),LAMIX(150),ETAMIX(150)
      REAL M1,M2,OMEGA1,OMEGA2,OMEG12,LAM1,LAM2,LAM12,PR,HE
      REAL LAMIX,ETAMIX
C
C
C   Now comes the input section where the counting variable
C   is initialized to zero and all required data is input.
C
C
      A12=1.1080
      B12=1.0905
      OMEG12=0.8470
      I=0
      M1=39.948
      M2=4.0026
      CP1=0.12477
      CP2=1.2512
      SIGMA1=3.418
      SIGMA2=2.556
      SIGM12=0.5*(SIGMA1+SIGMA2)
      OMEGA1=1.104

```


OMEGA2=0.7485

T=300

C

C

C Now the output files are created and opened and headings
C are placed where appropriate.

C

C

OPEN(67,FILE='PRANTL OUTPUT A1')

OPEN(68,FILE='PRANTL RESULTS A1')

WRITE(68,*)'THIS OUTPUT FILE IS FOR A MIXTURE OF
*GASES WITH'

WRITE(68,1)M1,M2

1 FORMAT('ATOMIC WEIGHTS OF ',F10.7,' AND',F10.7,' ,AND
* A ')

WRITE(68,2)T

2 FORMAT('TEMPERATURE OF ',F11.7,' DEGREES KELVIN.')

WRITE(68,*)

WRITE(68,*)' PRANTL HE THERMAL

* DYNAMIC'

WRITE(68,*)' NUMBER FRACTION CONDUCTIVITY

* VISCOSITY'

WRITE(68,*)

WRITE(68,*)' CAL/CM-SEC-K

* GM/CM-SEC'

WRITE(68,*)

C

C

C Now the Do loop is opened to perform the required

C calculations. The equations are from chapter eight of

C Hirschfelder and the equation numbers are as follows:

C ETA1 and ETA2 equation 8.2-18

C ETA12 equation 8.2-21

C LAM1 and LAM2 equation 8.2-31

C LAM12 equation 8.2-35

C U1,U2,UY,UZ,XLAM,YLAM, and ZLAM equation 8.2-36

C XETA,YETA, and ZETA EQUATION 8.2-22

C The equation for Prandtl number is $ETAMIX * CPMIX / LAMIX$.

C

C

```

DO 10 X1=0.0,1.005,0.01
  I=I+1

  ETA1=2.6693E-5*SQRT(M1*T)/(SIGMA1*SIGMA1*OMEGA1)
  ETA2=2.6693E-5*SQRT(M2*T)/(SIGMA2*SIGMA2*OMEGA2)
  ETA12=2.6693E-5*SQRT(2*M1*M2*T/(M1+M2))/(SIGM12*
*SIGM12*OMEG12)

  LAM1=1.9891E-4*SQRT(T/M1)/(SIGMA1*SIGMA1*OMEGA1)
  LAM2=1.9891E-4*SQRT(T/M2)/(SIGMA2*SIGMA2*OMEGA2)
  LAM12=1.9891E-4*SQRT(T*(M1+M2)/(2*M1*M2))/((SIGM12
***2)*OMEG12)

  U1=(4*A12/15)-(((B12/5)+(1/12))*(M1/M2))+(((M1-M2)
***2)/(2*M1*M2))

```

```

U2=(4*A12/15)-(((B12/5)+(1/12))*(M2/M1))+(((M2-M1)
***2)/(2*M1*M2))
UY=((4*A12/15)*(((M1+M2)**2)/(4*M1*M2))*(LAM12*LAM
*12/(LAM1*LAM2)))-((B12/5)+(1/12))-(((12*B12/32*A12
*)-(25/(32*A12)))*(((M1-M2)**2)/(M1*M2)))
UZ=((4*A12/15)*(((M1+M2)**@)/(4*M1*M2))*((LAM12/
*LAM1)+(LAM12/LAM2))-1))- (B12/5)-(1/12)
X2=1-X1
XETA=(X1*X1/ETA1)+(2*X1*X2/ETA12)+(X2*X2/ETA2)
YETA=(3*A12/5)*((X1*X1*M1/(M2*ETA1))+(X2*X2*M2/(M1*
*ETA2)))+(2*X1*X2*((M1+M2)**2)*(ETA12*ETA12)/(4*M1*M2*
*ETA1*ETA2*ETA12)))
ZETA=(3*A12/5)*((X1*X1*M1/M2)+(X2*X2*M2/M1))+((2*X1*
*X2)*(((M1+M2)**2)/(4*M1*M2))*((ETA12/ETA1)+(ETA12
*/ETA2)))-1)))
XLAM=(X1*X1/LAM1)+(2*X1*X2/LAM12)+(X2*X2/LAM2)
YLAM=(X1*X1*U1/LAM1)+(2*X1*X2*UY/LAM12)+(X2*X2*U2/
*LAM2)
ZLAM=(X1*X1*U1)+(2*X1*X2*UZ)+(X2*X2*U2)
PR(I)=((1+ZETA)*(XLAM+YLAM)*((X1*M1*CP1)+(X2*M2*CP2)
*))/((XETA+YETA)*(1+ZLAM)*((X1*M1)+(X2*M2)))
HE(I)=X2
LAMIX(I)=(1+ZLAM)/(XLAM+YLAM)
ETAMIX(I)=(1+ZETA)/(XETA+YETA)

```

C

C

C Now we will write to the output files the data that has
C been calculated.

C

C

WRITE(67,5)PR(I),HE(I)

WRITE(68,6)PR(I),HE(I),LAMIX(I),ETAMIX(I)

5 FORMAT(F10.7,F10.2)

6 FORMAT(F10.7,F12.2,E15.7,E15.7)

10 CONTINUE

STOP

END

APPENDIX B. PLOTTING PROGRAM

This appendix provides a program, written by the author, that will draw curves of Prandtl number versus helium fraction from the output file, "PRANTL OUTPUT A1", created by running the program "PRANDTL FORTRAN A1" that was presented in Appendix A. This program must be compiled in FORTVS and is specifically designed to use DISSPLA on the Naval Postgraduate School mainframe computer. Various DISSPLA subroutines are called by the program and each will be explained with comment statements. DISSPLA requires the data that is to be plotted to be in an array format. Each of the arrays used here are set to a maximum of 150 points. If modifications are made to "PRANDTL FORTRAN A1" such that more than 150 points are calculated the array sizes must be redefined. Two character strings are used in this program. They are NEW1\$ and NEW2\$, both of which are used to rename files. The first changes the input filename into the format required for DISSPLA and the second changes the file back to its original name for storage. The only parameters used are PR(I) and HE(I) which represent Prandtl number and helium fraction, respectively. Both of these quantities are real numbers and are defined as such in the program. This completes the introduction and explains the first three lines of the

program. The remainder of this appendix will be a listing of the program with explanatory comments. Latest update of program, March 1988.

```
Program GRFPRN

character*80 NEW1$,NEW2$

dimension PR(150),HE(150)

real PR,HE

c
c The next three lines rename the input file to the
c format necessary for DISSPLA and open it for use.
c
NEW1$='rename '///' PRANTL OUTPUT A1'///' file
*XYZ1 A1'

call excms(NEW1$)

open(67,file='XYZ1')

c
c In the next seven lines a Do loop is used to read
c all of the data from the input file into the
c specified arrays. Then the input file is closed and
c renamed it to its original name. The format line
c ensures the data is read from the file in the same
c format as it was written into the file.
c
1 format(f10.7,f10.2)

do 10 I=1,100
```

```

        read(67,1)PR(I),HE(I)

10      continue

20 close(67)

      New2$='rename '///' file XYZ1 A1'///' PRANTL

      *OUTPUT A1'

      call excms(NEW2$)

c
c The remainder of the program calls DISSPLA subroutines
c to create and plot the desired curves. Call tek618
c sets up the required machine for the plotting and
c links you to the plotter. You must be on a tek618
c terminal to use this program. Call blowup is used to
c magnify the plot to near full page size, for clarity.
c Call page sets up the page size, in inches. Call area2d
c sets up a two dimensional plot area of the specified
c size, in inches. Call xname and yname allow you to
c label the axes. Call headin allows naming the plot.
c Call graf sets up the physical origin and the maxima
c for the axes. The 'scale' portion of this call allows
c DISSPLA to select appropriate increments for the axes
c based on the minima and maxima specified. Call thkfrm
c and call frame place frames around the inner plot area
c and the entire plot, of a specified thickness. Call
c curve tells the plotter to plot the specified arrays of
c data points. The arrays must be called in the proper
c order (y-axis, x-axis) to get the correct curve. Call

```

c endpl ends the specific plot and sets up a new page for
c another plot. Call donepl tells the device you are done
c plotting.

c

```
    call tek618
    call blowup(1.5)
    call page(11,8.5)
    call area2d(8.,6.)
    call xname('helium fraction$',100)
    call yname('Prandtl number$',100)
    call headin('Prandtl number vs. helium fraction$',
*100,1.,1)
    call graf(0.0,'scale',1.0,0.4,'scale',0.7)
    call thkfrm(.02)
    call frame
    call curve(HE,PR,100,0)
    call endpl(0)
    call donepl
    stop
end
```


APPENDIX C. RAW DATA

This Appendix provides a listing of our spreadsheet, discussed in Chapter V, including all recorded data and calculated values that we have used. Many of the values are not related to our coefficient of performance evaluation, but were calculated for informational purposes.

The Appendix is broken down into three sets of three pages each, in order to fit the 24 column by 122 row spreadsheet within the desired margins. Each set of three pages covers the entire 24 columns for the specified data sets, with nine columns per page. We will discuss each of the columns, omitting the first which specifies the data set.

Columns 1,2,3,4,6,8,9,10 and 11 are all raw data and are self explanatory. Column 5 is the measured mean pressure of column 4, after conversion from milli-volts to psia (at 1.5 psia per mv). Column 7 converts the measured dynamic pressure signal of column 6 to percent pressure amplitude ($p_0/p_m = 1586 \times C6/C5$). Column 12 is an acceleration term that is calculated for use in the work equation as a correction for accelerometer non-linearities ($acc = 0.2848 \times C3 \times C8 / 170.5$). Column 13 is the absolute temperature ratio ($T_C/T_H = (C2 + 273.15) / (C1 + 273.15)$). Column 14 is the applied heater load in watts ($QHEAT = C9 \times C10 \times 0.001$ or $QHEAT = C10 \times C10 \times C11 / 10^6$, as appropriate). Column 15 is the

work in watts ($W=59810 \times (1-7.4 \times 10^{-5} \times C12) \times C6 \times 0.003 \times C8 / [1839.8 - 0.05(C3-550)]$), as discussed in Chapter V. Column 16 is the coefficient of performance, neglecting the heat leak from the cold end of the refrigerator ($COP=C14/C15$). Column 17 is the coefficient of performance relative to Carnot, neglecting the heat leak ($COPR=C16((1/C13)-1)$). Column 18 is the heat leak in watts, as discussed in Chapters IV and V ($HEATLK=0.0064(C1-C2)$). Column 19 is the coefficient of performance, taking into account the heat leak ($COP2=(C14+C18)/C15$). Column 20 is the coefficient of performance relative to Carnot, taking into account the heat leak ($COPR2=C19((1/C13)-1)$). Column 21 is the total heat load in watts ($Qtot=C14+C18$). Column 22 is the overall temperature difference ($\Delta T=C1-C2$). Column 23 is an approximate viscous penetration depth for the given temperature, pressure, frequency and gas type and an approximate value for dynamic viscosity ($VISC\ PEN=\sqrt{(C1+273.15)(0.005014692852)/(C3 \times C5)}$), where the coefficient takes into account all constants and the value used for dynamic viscosity). Column 24 is an approximate thermal penetration depth calculated from $\delta = \delta \sigma^{-1/2}$ ($THERM\ PEN=1.219820636 \times C23$). The equations for viscous and thermal penetration depths use a single value for δ and σ within each data set, respectively, instead of a value calculated for each data point. This is done for ease of calculation.

The resulting values are therefore not precise but merely reasonable approximations.

The spreadsheet of raw data and calculated values is provided on the next nine pages, and does not follow on this page for formatting reasons.

	TH	TC	FREQ	PMEAN	PMEAN	VPRESS	Po/Pm	VLOCKIN	VHEAT
	deg C	deg C	Hz	mVrms	psia	Vrms	%	mVrms	V
old stack pure He short resonator	25.1	-58.6	522.03	100.17	150.26	0.28391	2.997	367.3	0.000
	22.4	-57.2	523.20	99.98	149.97	0.18870	1.996	241.6	0.000
	22.6	-44.7	537.10	100.00	150.00	0.18890	1.997	262.1	6.870
	22.9	-34.0	548.70	99.97	149.96	0.18860	1.995	277.0	9.714
	23.2	-24.7	558.70	99.98	149.97	0.18940	2.003	289.1	11.897
	20.3	-13.5	570.40	101.06	151.59	0.18870	1.974	307.0	13.780
	23.1	-13.4	570.40	100.40	150.60	0.18900	1.990	309.0	13.780
	26.7	-43.0	539.60	99.93	149.90	0.28280	2.992	391.5	13.780
	22.8	-62.2	518.10	99.96	149.94	0.18960	2.006	228.2	0.000
	24.2	-71.3	508.40	100.05	150.08	0.28390	3.000	326.3	0.000
new stack pure He short resonator	22.6	-67.5	507.94	99.54	149.31	0.18902	2.008	233.1	
	25.9	-68.6	506.90	100.20	150.30	0.28332	2.990	349.8	
	23.2	-44.7	533.70	104.17	156.26	0.18873	1.916	256.1	
	23.5	-34.0	544.90	102.50	153.75	0.18903	1.950	280.2	
	23.6	-24.9	554.49	103.20	154.80	0.18947	1.941	293.1	
	24.1	-13.5	562.52	102.00	153.00	0.18939	1.963	319.8	
	26.9	-43.1	535.55	100.10	150.15	0.28340	2.993	416.8	
	25.3	-73.5	501.57	100.04	150.06	0.28367	2.998	337.2	
	22.6	-68.6	507.10	99.97	149.96	0.18900	1.999	230.1	
	20.7	-34.0	544.50	100.09	150.14	0.09465	1.000	147.7	
	23.7	-24.5	554.62	100.05	150.08	0.18886	1.996	309.0	
	23.7	-13.4	565.44	100.11	150.17	0.18922	1.998	331.7	
	23.0	-44.6	533.81	100.07	150.11	0.18899	1.997	272.5	
old stack He-Xe short resonator	23.7	-68.9	235.50	98.67	148.01	0.28390	3.042	169.3	0.000
	24.1	-60.5	239.86	98.13	147.20	0.28310	3.050	181.4	6.871
	24.2	-51.9	244.21	97.84	146.76	0.28310	3.059	194.1	9.706
	24.3	-42.7	248.82	97.54	146.31	0.28380	3.076	208.6	11.904
	22.4	-38.4	250.88	97.94	146.91	0.18870	2.037	142.2	8.416
	23.2	-70.1	234.76	98.84	148.26	0.28330	3.031	167.9	0.000
	21.0	-62.5	238.85	99.14	148.71	0.19000	2.026	118.6	0.000
	22.2	-17.5	260.29	98.60	147.90	0.18950	2.032	159.8	11.898
new stack He-Xe short resonator	22.9	-77.6	229.24	100.99	151.49	0.28380	2.971	160.3	
	24.1	-60.5	238.28	101.12	151.68	0.28340	2.963	181.7	
	23.9	-51.9	242.48	101.03	151.55	0.28291	2.961	193.5	
	24.5	-42.8	246.82	101.73	152.60	0.28291	2.940	202.8	
	22.1	-38.3	248.93	101.63	152.45	0.18910	1.967	141.5	
	22.3	-50.0	243.33	101.71	152.57	0.18870	1.962	130.0	
	21.9	-67.5	234.57	102.03	153.05	0.18910	1.960	113.2	
	23.5	-77.8	229.07	100.16	150.24	0.28340	2.992	161.6	
	23.3	-80.3	227.13	89.60	134.40	0.28421	3.354	183.8	

	IHEAT	RHEAT	ACC	TC/TH	QHEAT	WORK	COP	COPR	HEATLK
	mA	ohms	cgsE-3		watt	watt	Q=heater	c17/carn	watt
	0.00		320.28	0.7194	0.0000	9.9215	0.0000	0.0000	0.5692
	0.00		211.14	0.7307	0.0000	4.3736	0.0000	0.0000	0.5413
old	72.81		235.15	0.7725	0.5002	4.7429	0.1055	0.0311	0.4576
stack	102.82		253.88	0.8078	0.9988	4.9991	0.1998	0.0475	0.3869
pure He	125.82		269.80	0.8384	1.4969	5.2348	0.2860	0.0551	0.3257
short	145.60		292.51	0.8848	2.0064	5.5306	0.3628	0.0472	0.2298
resonator	145.60		294.41	0.8768	2.0064	5.5747	0.3599	0.0506	0.2482
	146.00		352.87	0.7676	2.0119	10.5129	0.1914	0.0580	0.4740
	0.00		197.49	0.7128	0.0000	4.1544	0.0000	0.0000	0.5780
	0.00		277.10	0.6788	0.0000	8.8393	0.0000	0.0000	0.6494
	0.00	94.00	197.77	0.6954	0.0000	4.2636	0.0000	0.0000	0.5676
	0.00	94.00	296.18	0.6840	0.0000	9.5190	0.0000	0.0000	0.5954
	89.50	94.40	228.31	0.7709	0.7562	4.6697	0.1619	0.0481	0.4278
	116.90	94.48	255.04	0.8062	1.2911	5.1085	0.2527	0.0608	0.3623
new	133.20	94.55	271.47	0.8366	1.6775	5.3509	0.3135	0.0612	0.3056
stack	158.30	94.64	300.49	0.8735	2.3716	5.8244	0.4072	0.0590	0.2369
pure He	158.00	94.40	372.86	0.7667	2.3566	11.2885	0.2088	0.0635	0.4410
short	0.00	94.00	282.51	0.6690	0.0000	9.1956	0.0000	0.0000	0.6224
resonator	0.00	94.00	194.91	0.6916	0.0000	4.2091	0.0000	0.0000	0.5746
	0.00	94.48	134.34	0.8139	0.0000	1.3606	0.0000	0.0000	0.3446
	138.00	94.55	286.27	0.8376	1.8006	5.6168	0.3206	0.0621	0.3037
	156.80	94.64	313.29	0.8750	2.3268	6.0303	0.3859	0.0551	0.2337
	99.50	94.40	242.98	0.7717	0.9346	4.9701	0.1880	0.0556	0.4259
	0.00		66.60	0.6881	0.0000	4.6249	0.0000	0.0000	0.5926
	72.97		72.68	0.7154	0.5014	4.9399	0.1015	0.0404	0.5414
old	102.94		79.18	0.7441	0.9992	5.2838	0.1891	0.0650	0.4870
stack	126.09		86.70	0.7748	1.5010	5.6900	0.2638	0.0767	0.4288
He-Xe	89.11		59.59	0.7943	0.7499	2.5844	0.2902	0.0752	0.3891
short	0.00		65.84	0.6852	0.0000	4.5772	0.0000	0.0000	0.5971
resonator	0.00		47.32	0.7161	0.0000	2.1716	0.0000	0.0000	0.5344
	125.77		69.48	0.8656	1.4964	2.9152	0.5133	0.0797	0.2541
	0.00	94.00	61.38	0.6605	0.0000	4.4137	0.0000	0.0000	0.6131
	95.70	94.16	72.32	0.7154	0.8624	4.9930	0.1727	0.0687	0.5161
new	119.30	94.29	78.37	0.7448	1.3420	5.3063	0.2529	0.0866	0.4624
stack	141.10	94.41	83.61	0.7739	1.8796	5.5598	0.3381	0.0988	0.4105
He-Xe	96.80	94.45	58.84	0.7954	0.8850	2.5979	0.3407	0.0876	0.3684
short	73.50	94.32	52.84	0.7553	0.5095	2.3824	0.2139	0.0693	0.4410
resonator	0.00	94.00	44.35	0.6970	0.0000	2.0797	0.0000	0.0000	0.5453
	0.00	94.00	61.83	0.6585	0.0000	4.4430	0.0000	0.0000	0.6179
	0.00	94.00	69.73	0.6505	0.0000	5.0646	0.0000	0.0000	0.6320

	COP2 w c19	COPR2 c20/carn	Qtot watt	DELTA T deg	VISC PEN cm	THERM PEN cm
	0.0574	0.0224	0.5692	83.70	0.008307	0.010133
	0.1238	0.0456	0.5413	79.60	0.008268	0.010086
old	0.2020	0.0595	0.9578	67.30	0.008162	0.009957
stack	0.2772	0.0659	1.3857	56.90	0.008081	0.009857
pure He	0.3482	0.0671	1.8226	47.90	0.008012	0.009773
short	0.4043	0.0526	2.2362	33.80	0.007848	0.009573
resonator	0.4044	0.0568	2.2546	36.50	0.007911	0.009651
	0.2365	0.0716	2.4858	69.70	0.008203	0.010006
	0.1391	0.0561	0.5780	85.00	0.008315	0.010143
	0.0735	0.0348	0.6494	95.50	0.008410	0.010259
	0.1331	0.0583	0.5676	90.10	0.008413	0.010262
	0.0625	0.0289	0.5954	94.50	0.008440	0.010296
	0.2535	0.0754	1.1839	67.90	0.008031	0.009796
	0.3237	0.0778	1.6534	57.50	0.008017	0.009779
new	0.3706	0.0724	1.9831	48.50	0.007921	0.009663
stack	0.4478	0.0649	2.6085	37.60	0.007917	0.009658
pure He	0.2478	0.0754	2.7976	70.00	0.008229	0.010038
short	0.0677	0.0335	0.6224	98.80	0.008483	0.010348
resonator	0.1365	0.0609	0.5746	91.20	0.008402	0.010249
	0.2533	0.0579	0.3446	54.70	0.008077	0.009853
	0.3746	0.0726	2.1043	48.20	0.008045	0.009814
	0.4246	0.0606	2.5606	37.10	0.007966	0.009717
	0.2737	0.0810	1.3605	67.60	0.008190	0.009991
	0.1281	0.0581	0.5926	92.60	0.006535	0.012596
	0.2111	0.0840	1.0428	84.60	0.006498	0.012524
old	0.2813	0.0967	1.4862	76.10	0.006450	0.012432
stack	0.3392	0.0986	1.9298	67.00	0.006401	0.012338
He-Xe	0.4407	0.1141	1.1391	60.80	0.006341	0.012223
short	0.1305	0.0599	0.5971	93.30	0.006534	0.012595
resonator	0.2461	0.0975	0.5344	83.50	0.006444	0.012421
	0.6005	0.0932	1.7505	39.70	0.006203	0.011955
	0.1389	0.0714	0.6131	100.50	0.006538	0.012603
	0.2761	0.1098	1.3784	84.60	0.006422	0.012378
new	0.3400	0.1165	1.8044	75.80	0.006367	0.012272
stack	0.4119	0.1203	2.2902	67.30	0.006295	0.012134
He-Xe	0.4825	0.1241	1.2535	60.40	0.006246	0.012040
short	0.3990	0.1293	0.9506	72.30	0.006317	0.012177
resonator	0.2622	0.1140	0.5453	89.40	0.006420	0.012374
	0.1391	0.0721	0.6179	101.30	0.006575	0.012672
	0.1248	0.0670	0.6320	103.60	0.006978	0.013451

	TH	TC	FREQ	PMEAN	PMEAN	VPRESS	Po/Pm	VLOCKIN	VHEAT
	deg C	deg C	Hz	mVrms	psia	Vrms	%	mVrms	V
	23.7	-72.5	291.33	100.84	151.26	0.28311	2.968	190.1	
new	24.4	-60.4	299.42	100.49	150.74	0.28301	2.978	208.1	
stack	24.2	-51.8	305.07	100.88	151.32	0.28321	2.968	220.3	
He-Ar	25.0	-42.9	310.85	101.84	152.76	0.28303	2.939	229.8	
(22%)	22.3	-38.2	313.60	100.82	151.23	0.18950	1.987	160.6	
short	22.5	-50.1	306.06	100.25	150.38	0.18878	1.991	149.8	
resonator	22.2	-65.0	296.28	100.25	150.38	0.18921	1.996	135.1	
	24.0	-72.2	291.54	100.25	150.38	0.28333	2.988	191.7	
	22.9	-60.3	470.43	100.40	150.60	0.18916	1.992	212.8	
	23.9	-44.8	485.56	99.98	149.97	0.18902	1.999	249.2	
new	23.9	-34.0	495.98	99.95	149.93	0.18920	2.001	276.7	
stack	24.6	-25.1	504.18	99.80	149.70	0.18902	2.003	298.7	
pure He	24.9	-13.7	514.63	100.38	150.57	0.18934	1.994	326.3	
long	22.9	-61.2	469.90	100.10	150.15	0.18932	2.000	212.2	
resonator	27.5	-43.1	488.19	99.92	149.88	0.28343	2.999	386.0	
	28.8	-32.3	498.54	100.00	150.00	0.28365	2.999	425.6	
	28.8	-32.3	498.52	99.93	149.90	0.28359	3.001	426.2	
	26.1	-62.0	468.88	99.98	149.97	0.28335	2.997	316.7	
	24.4	-64.0	284.28	99.94	149.91	0.28315	2.996	183.5	
new	24.7	-60.3	286.60	99.82	149.73	0.28300	2.998	191.7	
stack	25.2	-51.8	291.71	99.70	149.55	0.28310	3.002	208.1	
He-Ar	25.8	-43.0	296.91	99.64	149.46	0.28268	3.000	226.7	
(19%)	22.9	-38.4	299.55	100.09	150.14	0.18942	2.001	159.6	
long	22.9	-50.1	292.58	99.99	149.99	0.18923	2.001	142.0	
resonator	22.1	-60.9	286.15	100.02	150.03	0.18982	2.007	126.1	
	24.4	-64.9	283.80	99.98	149.97	0.28274	2.990	182.1	
	21.8	-63.1	207.92	99.78	149.67	0.18940	2.007	94.1	
new	22.6	-50.1	213.39	99.94	149.91	0.18902	2.000	108.7	
stack	22.4	-38.2	218.27	99.91	149.87	0.18948	2.005	124.2	
He-Xe	23.2	-26.2	222.90	99.83	149.75	0.18916	2.003	138.6	
long	23.0	-14.0	227.38	99.91	149.87	0.18957	2.006	154.2	
resonator	23.8	-2.3	231.63	100.01	150.02	0.18923	2.001	167.8	
	21.7	-63.0	207.98	99.85	149.78	0.18941	2.006	94.3	
	23.0	-41.0	490.81	100.01	150.02	0.18892	1.997	198.8	
	23.7	-34.1	497.57	99.84	149.76	0.18838	1.995	208.8	
dual	23.5	-24.9	506.39	99.83	149.75	0.18978	2.010	226.1	
stack	24.1	-13.1	517.38	100.56	150.84	0.18866	1.984	241.1	
pure He	24.2	-2.7	526.79	100.35	150.53	0.18900	1.991	260.2	
long	27.9	-13.3	517.66	100.27	150.41	0.28320	2.986	372.1	
resonator	27.2	-24.1	507.60	100.16	150.24	0.28346	2.992	345.3	
	27.1	-33.4	498.35	100.18	150.27	0.28369	2.994	322.8	
	26.0	-38.6	493.36	100.20	150.30	0.28325	2.989	309.7	
	24.8	-55.5	472.10	59.68	89.52	0.17804	3.154	353.6	

	IHEAT	RHEAT	ACC	TC/TH	QHEAT	WORK	COP	COPR	HEATLK
	mA	ohms	cgsE-3		watt	watt	Q=heater	c17/carn	watt
	0.00	94.00	92.51	0.6759	0.0000	5.2182	0.0000	0.0000	0.5580
new	80.10	94.16	104.08	0.7150	0.6041	5.7066	0.1059	0.0422	0.4918
stack	107.70	94.29	112.26	0.7444	1.0937	6.0427	0.1810	0.0621	0.4408
He-Ar	128.40	94.41	119.32	0.7723	1.5565	6.2969	0.2472	0.0729	0.3938
(22%)	91.20	94.45	84.13	0.7952	0.7856	2.9544	0.2659	0.0685	0.3509
short	67.10	94.32	76.58	0.7544	0.4247	2.7462	0.1546	0.0503	0.4211
resonator	0.00	94.00	66.86	0.7048	0.0000	2.4835	0.0000	0.0000	0.5058
	0.00	94.00	93.35	0.6763	0.0000	5.2659	0.0000	0.0000	0.5580
	0.00	94.16	167.22	0.7190	0.0000	3.9001	0.0000	0.0000	0.5242
	120.00	94.40	202.12	0.7687	1.3594	4.5538	0.2985	0.0898	0.4328
new	159.00	94.48	229.24	0.8051	2.3885	5.0523	0.4728	0.1145	0.3648
stack	183.50	94.55	251.56	0.8331	3.1837	5.4409	0.5851	0.1172	0.3131
pure He	212.60	94.64	280.50	0.8705	4.2776	5.9424	0.7198	0.1071	0.2432
long	0.00	94.14	166.56	0.7159	0.0000	3.8926	0.0000	0.0000	0.5298
resonator	190.50	94.40	314.77	0.7652	3.4258	10.4081	0.3266	0.1002	0.4448
	237.60	94.49	354.42	0.7977	5.3343	11.5415	0.4622	0.1172	0.3849
	238.10	94.49	354.90	0.7977	5.3568	11.5549	0.4636	0.1176	0.3849
	0.00	94.12	248.04	0.7056	0.0000	8.6416	0.0000	0.0000	0.5550
	0.00	94.08	87.14	0.7029	0.0000	5.0388	0.0000	0.0000	0.5746
new	70.80	94.16	91.77	0.7146	0.4720	5.2597	0.0897	0.0358	0.5525
stack	130.60	94.29	101.40	0.7419	1.6082	5.7084	0.2817	0.0980	0.5005
He-Ar	168.60	94.40	112.43	0.7699	2.6834	6.2051	0.4325	0.1293	0.4472
(19%)	121.50	94.44	79.86	0.7929	1.3941	2.9346	0.4751	0.1241	0.3985
long	81.70	94.32	69.40	0.7534	0.6296	2.6099	0.2412	0.0789	0.4745
resonator	0.00	94.15	60.27	0.7189	0.0000	2.3261	0.0000	0.0000	0.5395
	0.00	94.06	86.33	0.6999	0.0000	4.9933	0.0000	0.0000	0.5805
	0.00	94.15	32.68	0.7122	0.0000	1.7318	0.0000	0.0000	0.5349
new	83.40	94.29	38.75	0.7542	0.6558	1.9959	0.3286	0.1071	0.4580
stack	120.20	94.42	45.28	0.7950	1.3642	2.2852	0.5970	0.1540	0.3818
He-Xe	146.40	94.54	51.60	0.8333	2.0263	2.5450	0.7962	0.1593	0.3112
long	171.70	94.67	58.57	0.8751	2.7910	2.8365	0.9840	0.1405	0.2331
resonator	190.60	94.80	64.92	0.9121	3.4439	3.0800	1.1182	0.1077	0.1644
	0.00	94.15	32.76	0.7127	0.0000	1.7356	0.0000	0.0000	0.5336
	0.00	94.39	162.98	0.7839	0.0000	3.6356	0.0000	0.0000	0.3776
	72.70	94.46	173.54	0.8053	0.4992	3.8053	0.1312	0.0317	0.3410
dual	114.50	94.56	191.25	0.8369	1.2397	4.1467	0.2990	0.0583	0.2856
stack	148.30	94.67	208.36	0.8749	2.0821	4.3914	0.4741	0.0678	0.2195
pure He	175.70	94.80	228.96	0.9095	2.9265	4.7417	0.6172	0.0614	0.1587
long	207.00	94.67	321.75	0.8632	4.0565	10.0871	0.4021	0.0638	0.2431
resonator	154.80	94.57	292.77	0.8292	2.2662	9.3872	0.2414	0.0497	0.3027
	85.70	94.46	268.71	0.7985	0.6938	8.7963	0.0789	0.0199	0.3570
	0.00	94.41	255.22	0.7841	0.0000	8.4337	0.0000	0.0000	0.3811
	0.00	94.23	278.84	0.7305	0.0000	6.0381	0.0000	0.0000	0.4738

	COP2 w c19	COPR2 c20/carn	Qtot watt	DELTA T deg	VISC PEN cm	THERM PEN cm
	0.1069	0.0513	0.5580	96.20	0.007043	0.010759
new	0.1921	0.0765	1.0960	84.80	0.006967	0.010644
stack	0.2539	0.0872	1.5345	76.00	0.006887	0.010521
He-Ar	0.3097	0.0913	1.9503	67.90	0.006799	0.010387
(22%)	0.3847	0.0990	1.1365	60.50	0.006773	0.010347
short	0.3080	0.1002	0.8457	72.60	0.006877	0.010507
resonator	0.2036	0.0853	0.5058	87.20	0.006986	0.010673
	0.1060	0.0507	0.5580	96.20	0.007064	0.010792
	0.1344	0.0525	0.5242	83.20	0.008709	0.010623
	0.3936	0.1184	1.7922	68.70	0.008604	0.010496
new	0.5450	0.1319	2.7533	57.90	0.008515	0.010387
stack	0.6427	0.1288	3.4968	49.70	0.008462	0.010322
pure He	0.7608	0.1132	4.5208	38.60	0.008355	0.010192
long	0.1361	0.0540	0.5298	84.10	0.008727	0.010645
resonator	0.3690	0.1133	3.8706	70.60	0.008636	0.010534
	0.4955	0.1257	5.7192	61.10	0.008561	0.010442
	0.4969	0.1261	5.7417	61.10	0.008564	0.010446
	0.0642	0.0268	0.5550	88.10	0.008789	0.010720
	0.1140	0.0482	0.5746	88.40	0.007475	0.011314
new	0.1948	0.0778	1.0245	85.00	0.007453	0.011281
stack	0.3694	0.1285	2.1087	77.00	0.007398	0.011198
He-Ar	0.5045	0.1508	3.1306	68.80	0.007343	0.011114
(19%)	0.6109	0.1595	1.7926	61.30	0.007258	0.010986
long	0.4230	0.1384	1.1041	73.00	0.007348	0.011122
resonator	0.2319	0.0907	0.5395	83.00	0.007419	0.011229
	0.1162	0.0498	0.5805	89.30	0.007480	0.011322
	0.3089	0.1248	0.5349	84.90	0.006894	0.013288
new	0.5581	0.1819	1.1138	72.70	0.006809	0.013124
stack	0.7640	0.1971	1.7460	60.60	0.006731	0.012974
He-Xe	0.9185	0.1837	2.3375	49.40	0.006673	0.012861
long	1.0661	0.1522	3.0241	37.00	0.006602	0.012724
resonator	1.1715	0.1129	3.6084	26.10	0.006546	0.012618
	0.3075	0.1239	0.5336	84.70	0.006890	0.013279
	0.1039	0.0286	0.3776	64.00	0.008544	0.010422
	0.3208	0.0504	0.8403	57.80	0.008503	0.010372
dual	0.3678	0.0717	1.5253	48.40	0.008426	0.010279
stack	0.5241	0.0750	2.3015	37.20	0.008314	0.010142
pure He	0.6507	0.0647	3.0852	26.90	0.008250	0.010063
long	0.4262	0.0676	4.2996	41.20	0.008377	0.010219
resonator	0.2737	0.0564	2.5689	51.30	0.008455	0.010313
	0.1194	0.0301	1.0507	60.50	0.008530	0.010406
	0.0452	0.0124	0.3811	64.60	0.008557	0.010438
	0.0785	0.0289	0.4738	80.30	0.011312	0.013798

	TH	TC	FREQ	PMEAN	PMEAN	VPRESS	Po/Pm	VLOCKIN	VHEAT
	deg C	deg C	Hz	mVrms	psia	Vrms	%	mVrms	V
	23.7	-41.0	217.92	100.12	150.18	0.28365	2.996	144.7	
dual	24.6	-31.2	222.07	100.73	151.10	0.28308	2.971	154.9	
stack	24.8	-21.1	226.16	100.63	150.95	0.28335	2.977	168.1	
He-Xe	25.6	-11.4	230.13	101.49	152.24	0.28289	2.947	177.9	
long	22.2	-40.6	217.91	97.26	145.89	0.18935	2.058	99.0	
resonator	23.0	-28.0	223.30	100.87	151.31	0.18890	1.980	104.0	
	22.5	-14.0	228.81	99.64	149.46	0.18928	2.009	118.6	
	24.4	-41.0	217.90	99.70	149.55	0.28332	3.005	144.7	
	23.8	-36.6	238.56	99.70	149.55	0.28328	3.004	170.3	
dual	24.0	-27.9	242.61	100.30	150.45	0.28351	2.989	177.1	
stack	24.2	-16.9	247.39	100.56	150.84	0.28333	2.979	186.6	
He-Xe	24.4	-7.0	251.73	101.53	152.30	0.28349	2.952	193.8	
short	22.0	-34.6	239.37	99.43	149.15	0.18893	2.009	113.6	
resonator	22.3	-23.8	244.41	100.44	150.66	0.18864	1.986	118.5	
	22.1	-11.9	249.70	101.03	151.55	0.18907	1.979	125.9	
	24.1	-36.3	238.77	99.40	149.10	0.28244	3.004	170.6	
	25.9	-31.0	545.83	100.49	150.74	0.28347	2.983	350.1	
	26.6	-22.9	554.24	98.71	148.07	0.28264	3.028	374.1	
dual	26.6	-15.0	562.40	99.23	148.85	0.28305	3.016	386.1	
stack	27.2	-7.1	570.22	99.49	149.24	0.28270	3.004	400.1	
pure He	23.1	-34.6	541.73	100.09	150.14	0.18935	2.000	224.7	
short	23.4	-22.9	554.27	101.09	151.64	0.18919	1.979	235.3	
resonator	23.4	-12.9	564.27	99.59	149.39	0.18939	2.011	254.4	
	23.9	-3.0	574.07	100.11	150.17	0.18897	1.996	264.1	
	23.6	5.0	581.68	99.83	149.75	0.18951	2.007	276.7	
	23.4	-32.2	543.70	99.83	149.75	0.18909	2.003	227.8	

	IHEAT	RHEAT	ACC	TC/TH	QHEAT	WORK	COP	COPR	HEATLK
	mA	ohms	cgsE-3		watt	watt	Q=heater	c17/carn	watt
	0.00	94.38	52.67	0.7821	0.0000	3.9758	0.0000	0.0000	0.3921
dual	100.00	94.48	57.46	0.8126	0.9448	4.2465	0.2225	0.0513	0.3381
stack	147.60	94.60	63.50	0.8460	2.0609	4.6112	0.4469	0.0814	0.2782
He-Xe	179.50	94.70	68.39	0.8762	3.0513	4.8708	0.6264	0.0885	0.2242
long	0.00	94.39	36.04	0.7874	0.0000	1.8181	0.0000	0.0000	0.3806
resonator	77.10	94.52	38.79	0.8278	0.5619	1.9052	0.2949	0.0613	0.3091
	121.10	94.66	45.33	0.8765	1.3882	2.1763	0.6379	0.0898	0.2212
	0.00	94.38	52.67	0.7802	0.0000	3.9711	0.0000	0.0000	0.3963
	0.00	94.43	67.36	0.7966	0.0000	4.6704	0.0000	0.0000	0.3600
dual	69.00	94.52	71.77	0.8253	0.4500	4.8600	0.0926	0.0196	0.3093
stack	106.40	94.64	77.11	0.8618	1.0714	5.1161	0.2094	0.0336	0.2450
He-Xe	130.30	94.75	81.49	0.8945	1.6087	5.3154	0.3026	0.0357	0.1871
short	0.00	94.46	45.42	0.8082	0.0000	2.0813	0.0000	0.0000	0.3373
resonator	57.90	94.57	48.38	0.8440	0.3170	2.1676	0.1463	0.0270	0.2748
	83.70	94.70	52.51	0.8848	0.6634	2.3078	0.2875	0.0374	0.2026
	0.00	94.43	68.04	0.7968	0.0000	4.6648	0.0000	0.0000	0.3600
	0.00	94.49	319.20	0.8097	0.0000	9.5091	0.0000	0.0000	0.3653
	86.50	94.57	346.34	0.8349	0.7076	10.1127	0.0700	0.0138	0.3178
dual	119.70	94.66	362.71	0.8612	1.3563	10.4416	0.1299	0.0209	0.2671
stack	143.60	94.74	381.09	0.8858	1.9536	10.7941	0.1810	0.0233	0.2202
pure He	0.00	94.45	203.33	0.8052	0.0000	4.1120	0.0000	0.0000	0.3704
short	69.40	94.57	217.85	0.8439	0.4555	4.2992	0.1059	0.0196	0.2972
resonator	96.60	94.67	239.78	0.8776	0.8834	4.6467	0.1901	0.0265	0.2330
	115.00	94.83	253.25	0.9094	1.2541	4.8096	0.2608	0.0260	0.1727
	129.40	94.90	268.85	0.9373	1.5890	5.0486	0.3147	0.0210	0.1194
	0.00	94.47	206.88	0.8125	0.0000	4.1621	0.0000	0.0000	0.3570

	COP2 w c19	COPR2 c20/carn	Qtot watt	DELTA T deg	VISC PEN cm	THERM PEN cm
	0.0986	0.0275	0.3921	64.70	0.006744	0.012999
dual	0.3021	0.0697	1.2829	55.80	0.006671	0.012858
stack	0.5073	0.0924	2.3391	45.90	0.006616	0.012752
He-Xe	0.6725	0.0951	3.2755	37.00	0.006539	0.012604
long	0.2093	0.0565	0.3806	62.80	0.006826	0.013156
resonator	0.4571	0.0951	0.8709	51.00	0.006630	0.012779
	0.7395	0.1042	1.6094	36.50	0.006584	0.012691
	0.0998	0.0281	0.3963	65.40	0.006767	0.013043
	0.0771	0.0197	0.3600	60.40	0.006461	0.012453
dual	0.1562	0.0331	0.7593	51.90	0.006389	0.012315
stack	0.2573	0.0413	1.3164	41.10	0.006321	0.012184
He-Xe	0.3379	0.0399	1.7958	31.40	0.006239	0.012025
short	0.1621	0.0385	0.3373	56.60	0.006439	0.012411
resonator	0.2730	0.0505	0.5918	46.10	0.006343	0.012226
	0.3753	0.0488	0.8661	34.00	0.006255	0.012057
	0.0772	0.0197	0.3600	60.40	0.006471	0.012472
	0.0384	0.0090	0.3653	56.90	0.008122	0.009907
	0.1014	0.0201	1.0254	49.50	0.008142	0.009932
dual	0.1555	0.0251	1.6234	41.60	0.008062	0.009834
stack	0.2014	0.0260	2.1738	34.30	0.008004	0.009763
pure He	0.0901	0.0218	0.3704	57.70	0.008131	0.009918
short	0.1751	0.0324	0.7527	46.30	0.008002	0.009761
resonator	0.2403	0.0335	1.1165	36.30	0.007991	0.009747
	0.2967	0.0295	1.4268	26.90	0.007908	0.009647
	0.3384	0.0226	1.7085	18.60	0.007863	0.009592
	0.0858	0.0198	0.3570	55.60	0.008131	0.009918

REFERENCES

- Boyd, A. W., Kosinski, B. P., and Weston, R. L., "Autonomous Measurement of Space Shuttle Payload Bay Acoustics During Launch," Naval Research Reviews, vol. 39 (1), p. 9, 1987.
- Ceperley, P. H., "A Pistonless Stirling Engine - The Traveling Wave Heat Engine," Journal of the Acoustical Society of America, vol. 66, p. 1508, 1979.
- Chapman, S. and Cowling, T. G., The Mathematical Theory of Non-Uniform Gases, Cambridge University Press, 1939.
- Faraday, M., Quarterly Journal of Science, vol. 5, p. 274, 1818.
- Fitzpatrick, M., Electrodynamic Driver for the Space Thermoacoustic Refrigerator (STAR), Masters Thesis, Naval Postgraduate School, Monterey, CA, March 1988.
- Garrett, S. L., Swift G. W., and Packard, R. E., "Helium Gas Purity Monitor for Recovery Systems," Physica, vol. 107B, p. 601, 1981.
- Get Away Special Team, Get Away Special (GAS) Small Self-contained Payloads--Experimenter Book, National Aeronautics and Space Administration, Goddard Space Flight Center, Special Payloads Division, Greenbelt, MD, July 1984.
- Gifford, W. E. and Longworth, R. C., "Surface Heat Pumping," International Advances in Cryogenic Engineering, vol. 11, p. 171, Plenum, NY, 1966.
- Hirschfelder, J. O., Curtiss, C. F., and Bird, R. B., Molecular Theory of Gases and Liquids, John Wiley & Sons, Inc., NY, 1954.
- Hofler, T. J., Thermoacoustic Refrigeration Design and Performance, Ph.D. Dissertation, University of California, San Diego, CA, 1986.
- Hofler, T. J., "Accurate Acoustic Power Measurements with a High-intensity Driver," Journal of the Acoustical Society of America, vol. 83 (2), p. 777, 1988.
- Huang, F. F., Engineering Thermodynamics, Fundamentals and Applications, Macmillan Publishing Co., Inc., NY, 1976.

Kempton, A. J., "Heat Diffusion as a Source of Aerodynamic Sound," Journal of Fluid Mechanics, vol. 78, p. 1, 1976.

Merkli, P. and Thomann, H., "Thermoacoustic Effects in a Resonant Tube," Journal of Fluid Mechanics, vol. 70, p. 161, 1975.

Polturak, E., Garrett, S. L., and Lipson, S. G., "Precision Acoustic Gas Analyzer for Binary Mixtures," Rev. Sci. Inst., vol. 57 (11), p. 2837, 1986.

Rayleigh, Lord, Proceedings of the Royal Society, vol. VIII, p. 536; Nature, vol. XVIII, p. 319, 1878.

Rayleigh, Lord, Theory of sound, Second Edition, Volume II, Section 332i, Dover, NY, 1945.

Reif, F., Fundamentals of Statistical and Thermal Physics, McGraw-Hill Inc., 1965.

Rijke, P. L., Annals of Physics (Leipzig), vol. 107, p. 339, 1859.

Rott, N., "Damped and Thermally Driven Acoustic Oscillations in Wide and Narrow Tubes," Journal of Applied Mathematics and Physics (ZAMP), vol. 20, 1969.

Rott, N., "The Heating Effect Connected with Non-linear Oscillations in a Resonant Tube," Journal of Applied Mathematics and Physics (ZAMP), vol. 25, 1974.

Rott, N., "Thermally Driven Acoustic Oscillations, Part III: Second Order Heat Flux," Journal of Applied Mathematics and Physics (ZAMP), vol. 26, 1975.

Rott, N., "Thermoacoustics," Advances in Applied Mechanics, vol. 20, 1980.

Sears, F. W. and Salinger, G. L., Thermodynamics, Kinetic Theory, and Statistical Thermodynamics, Third Edition, pp. 113-115, Addison-Wesley, 1975.

Smith, J. L. Jr., Robinson, G. Y. Jr., and Isawa, Y., Survey of the State-of-the-Art of Miniature Cryocoolers for Superconductive Devices, Naval Research Laboratory, Washington, D. C., 1984.

Sondhauss, C., Annals of Physics and Chemistry, Volume 79, (1), 1850.

Swift, G. W., "Thermoacoustic Engines", to be published in the Journal of the Acoustical Society of America, circa 1989.

Swift, G. W., Migliori, A., Garrett, S. L., and Wheatley, J. C., "Two Methods for Absolute Calibration of Dynamic Pressure Transducers," Review of Scientific Instruments, vol. 53 (1), p. 1906, 1982.

Taconis, K. W., Beenakker, J. J. M., Nier, A. O. C., and Aldrich, L. T., "Measurements Concerning the Vapour-liquid Equilibrium of Solutions of He^3 in He^4 Below 2.19°K," Physica, vol. 15, p. 733, 1949.

Walker, G., "Cryocoolers, Parts 1 and 2," International Cryogenics Monograph Series, Plenum Press, NY, 1983.

Wheatley, J. C. and Cox, A., "Natural Engines," Physics Today, August, 1985.

Wheatley, J. C., Hofler, T. J., Swift, G. W., and Migliori, A., "Experiments with an Intrinsically Irreversible Acoustic Heat Engine," Physical Review Letters, vol. 50 (7), p. 499, February, 1983a.

Wheatley, J. C., Hofler, T. J., Swift, G. W., and Migliori, A., "An Intrinsically irreversible Thermoacoustic Heat Engine," Journal of the Acoustical Society of America, vol. 74 (1), p. 153, July, 1983b.

Wheatley, J. C., Hofler, T. J., Swift, G. W., and Migliori, A., "Understanding Some Simple Phenomena in Thermoacoustics with Applications to Acoustical Heat Engines," American Journal of Physics, vol. 53 (2), p. 147, February, 1985.

Wheatley, J. C., Swift, G. W., and Migliori, A., "The Natural Heat Engine," Los Alamos Science, Number 14, Fall 1986.

Yazaki, T., Tominaga, A., and Narahara, Y., Journal of Low Temperature Physics, vol. 41, p. 45, 1980.

INITIAL DISTRIBUTION LIST

	No. Copies
1. Defense Technical Information Center Cameron Station Alexandria, VA 22304-6145	2
2. Library, Code 0142 Naval Postgraduate School Monterey, CA 93943-5002	2
3. Professor S. L. Garrett, Code 61Gx Naval Postgraduate School Monterey, CA 93943-5000	8
4. Dr. T. Hofler, Code 61Hf Naval Postgraduate School Monterey, CA 93943-5000	3
5. Professor A. Atchley, Code 61Ay Naval Postgraduate School Monterey, CA 93943-5000	1
6. Dr. L. E. Hargrove Office of Naval Research Physics Division - Code 1112 800 N. Quincy Street Arlington, VA 22217	1
7. Professor I. Rudnick UCLA--Physics Dept. 405 Hilgard Ave. Los Angeles, CA 90024	1
8. Commanding Officer Office of Naval Technology ATTN: Dr. Philip Selwyn (Code 20) CAPT R. S. Fitch (Code 23D) 800 N. Quincy Street Arlington, VA 22217	1 1
9. Dr. M. Melich, 9637 North 24th Street Arlington, VA 22207	2
10. Commanding Officer Naval Air Development Center ATTN: Dr. T. Gabrielson Warminster, PA 18974	1

11. Commanding Officer
Naval Research Laboratory
ATTN: T. G. Giallorenzi 1
F. Hellrich 1
4555 Overlook Avenue
Washington, D. C. 20375-5000
12. Professor A. H. Fuhs, Code 67Fu 1
Naval Postgraduate School
Monterey, CA 93943-5000
13. Professor R. Panholzer, Code 62Pz 2
Naval Postgraduate School
Monterey, CA 93943-5000
14. D. Rigmaiden, Code 72 1
Naval Postgraduate School
Monterey, CA 93943-5000
15. LT Scott Palmer 1
Space and Naval Warfare Systems Command
PDW 106/72A
Washington, D. C. 20360-5100
16. Ms. Carol Tanner 1
Mail Station N4/910
Aerospace Corporation
P. O. Box 92957
Los Angeles, CA 90009
17. Rear Admiral Truly 1
Commander Naval Space Command
Dahlgren, VA 22448-5170
18. Mr. Frank Deithrick 1
Space and Naval Warfare Systems Command
Washington, D. C. 20363-5100
19. The University of Texas at Austin
ATTN: Prof. I. Busch-Vishniac (Mech. Eng.) 1
Prof. W. D. McCormick (Physics) 1
Austin, TX 78713-8029
20. Los Alamos National Laboratories
Condensed Matter and Thermal Physics (Group P-10)
ATTN: Dr. G. W. Swift 1
Dr. A. Migliori 1
P. O. Box 1663/MS 764
Los Alamos, NM 87545

21. Commanding Officer
Naval Weapons Center
Office of Counsel - Code 006
ATTN: Steven Church 1
China Lake, CA 93555
22. LCDR Allen Hansen 1
Navy Space System Activity
P. O. Box 92960 WWP
Los Angeles, CA 90009
23. LT Mary Cox 1
Dept. of the Air Force
Space Test Program Office (SD/CLTPC)
HQ Space Division
P. O. Box 92960
Los Angeles, CA 90009-2960
24. Dr. S. F. Watanabe 1
Director, Technology Assessment
McDonnell Douglas Corporation
1550 Wilson Blvd., Suite 550
Arlington, VA 22209
25. The Aerospace Corporation
ATTN: Dr. Bruce C. Edgar (M1/120) 1
Julie D. White (M1/122) 1
P. O. Box 92957
Los Angeles, CA 90009-2957
26. LT Michele Fitzpatrick 1
1634 W. Norwegian St.
Pottsville, PA 17901
27. LT Michael P. Susalla 6
4148 Mustang Street
San Diego, CA 92111
28. LT R. Volkhert 1
Code 33, UX
Naval Postgraduate School
Monterey, CA 93943
29. CPT D. Harris 1
Code 33, UX
Naval Postgraduate School
Monterey, CA 93943

30. National Center for Physical Acoustics
ATTN: Librarian
P. O. Box 847
Fraternity Row
University, MS 38677 1
31. Dr. Robert Fisher
Lockheed Corporation
3170 Porter Drive
Sunnyvale, CA 95070 1
32. LCDR Austin Bond
NMPC Sea Duty Component
P. O. Box 16134
Arlington, VA 22215-1134 1
33. Professor K. E. Woehler, Code 61Wh
Physics Department Chairman
Naval Postgraduate School
Monterey, CA 93943-5000 1

JAN 2 1996
FEB 12 1996

Thesis

S8642 Susalla

c.1 Thermodynamic improve-
ments for the space
thermoacoustic refrigera-
tor (STAR).

thesS8642

Thermodynamic improvements for the space



3 2768 000 78947 3

DUDLEY KNOX LIBRARY